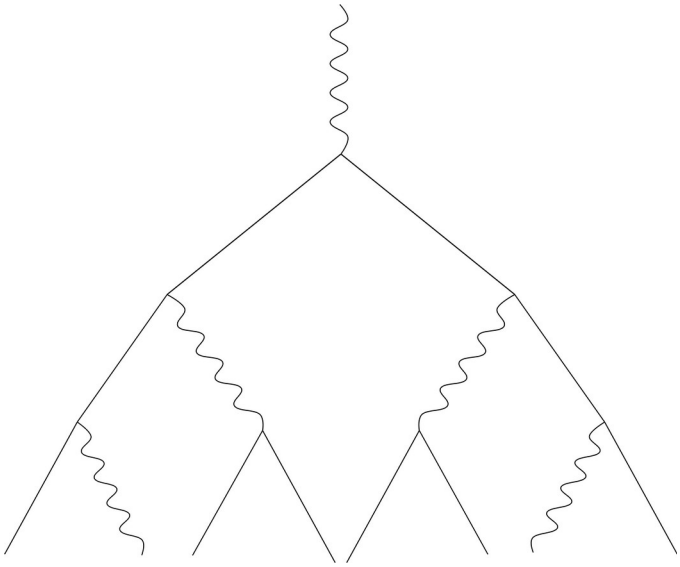


Fast Radio Bursts and Multimessenger Astrophysics with the Pierre Auger Observatory

Maria Alexandra Lima Fernandes
Mestrado em Astronomia e Astrofísica
Departamento de Física e Astronomia
2021

Orientador
Raul Sarmento, Investigador, LIP

Coorientador
Orfeu Bertolami Neto, Professor Catedrático, FCUP



Todas as correções determinadas pelo júri, e só essas, foram efetuadas.

O Presidente do Júri,

Porto, / /

Universidade do Porto

Faculdade de Ciências

Mestrado em Astronomia e Astrofísica

Fast Radio Bursts and Multimessenger Astrophysics with the Pierre Auger Observatory

Maria Alexandra Lima Fernandes

Supervisor
Dr. Raul Sarmento

Co-supervisor
Prof. Dr. Orfeu Bertolami Neto

A thesis submitted in fulfilment of the requirements for the degree of Master of Science

at

Departamento de Física e Astronomia

Porto, September of 2021

[This page was intentionally left blank]

Acknowledgements

I want to thank everyone for their direct or indirect help with this thesis, as it was essential to overcome all the obstacles along the way.

First, I want to thank my supervisor Dr. Raul Sarmento for the many helpful online discussions, suggestions of literature and countless emails as they were fundamental for the success of this thesis. I also want to thank my co-supervisor Prof. Dr. Orfeu Bertolami Neto for the insightful discussions and suggestions, as well as the constant availability.

Thirdly, I want to mention my friends and colleagues, Gonçalo Roboredo, Inês Carvalho, Maura Barros, Laure Trichet and Patricia Orobiyi, for the constant support and help during this challenging period.

Lastly, I thank my family, for the immense support along the years as it was vital in my growth and love for Physics. To my mom and my sisters, Raquel, Susana and Mariana, a special thank you for putting up with my constant blabbering about physics.

[This page was intentionally left blank]

Abstract

Fast Radio Bursts (FRBs) are millisecond radio bursts from extragalactic sources that occur at a rate of thousands per day, over the entire sky, with radiation energy densities at the source about ten billion times larger than those from Galactic pulsars. There are still a lot of unknowns surrounding FRBs, namely whether there are different internal populations, repeaters and non repeaters and the mechanisms of their emission and sources, since to justify their energetics, there has to be an exotic, extremely powerful event. Source models such as, the "Baryon Loaded Shock Scenario", predict the emission of both FRBs and high energy photons and neutrinos by a magnetar. In order to bridge the gap between theory and experiment, a sensitivity study was conducted for the Pierre Auger Observatory as well as for other extensive atmospheric shower detectors with wide field-of-view, to estimate upper limits to the spectral photon fluence at 90% confidence level (CL). A first estimation was made considering a perfect trigger efficiency, which was then afterwards compared to the same estimate using a realistic one. Then, an analysis to evaluate the effect of the time interval and of the zenith angle in the upper limit was conducted. A second analysis was performed using other observatories, namely HAWC, LHAASO and SWGO. A combined sensitivity was also estimated using catalogued FRB events and the corresponding exposure of each observatory, HAWC and LHAASO, at the time of detection. It was concluded that constraining the theoretical models would only be possible after the detection of either a single very bright ($\varepsilon_{radio} > 10^{40}$ erg) and with a nearby ($d \sim 0.1$ kpc) source FRB or sufficient less energetic galactic events, for which a stack analysis could be performed, improving sufficiently the sensitivity of detection.

[This page was intentionally left blank]

Resumo

"Fast Radio Bursts" (FRBs) são pulsos de rádio, com duração de milisegundos, originários de fontes extragaláticas e que ocorrem a taxas de milhares por dia, cobrindo todo o céu. São emitidos com densidades de energia aproximadamente mil milhões de vezes superiores às de um pulso de rádio vindo de uma pulsar. Os FRBs estão ainda envoltos por um manto de incerteza, nomeadamente no que toca à existência de diferentes populações internas, se se repetem ou não e sobre as suas fontes e mecanismos de emissão, uma vez que para justificar as energias envolvidas é necessário considerar eventos astrofísicos exóticos e extremamente energéticos. Modelos teóricos como o "Baryon Loaded Shock Scenario" prevêm tanto a emissão de FRBs, como a emissão de neutrinos e fotões de alta energia por parte de um "magnetar". Este modelo serviu como guia para o trabalho apresentado nesta tese, em que realizámos um estudo de sensibilidade tanto para o Observatório Pierre Auger como para outros detetores de chuveiros atmosféricos extensivos, através da estimativa do limite superior da fluência espectral para um nível de confiança de 90%. Assim, é inicialmente feita uma comparação entre duas estimativas para a sensibilidade - uma considerando uma eficiência de "trigger" ideal e outra uma eficiência de "trigger" realista. Analisámos, em seguida, o efeito do intervalo de tempo e do ângulo zenital no limite superior da fluência. Uma segunda análise foi efetuada usando outros observatórios - HAWC, LHAASO e SWGO. Um estudo de sensibilidade combinada foi também realizado utilizando eventos de FRBs catalogados para o observatório HAWC e LHAASO, no momento de deteção. Conclui-se que o constrangimento do modelo teórico só seria possível depois da deteção ou de um único FRB muito energético ($\varepsilon_{\rm radio} > 10^{40}$ erg), com uma fonte próxima ($d \sim 0.1$ kpc), ou de suficientes eventos galáticos menos energéticos, para os quais uma análise de "stack" poderia ser realizada, melhorando a sensibilidade da deteção.

[This page was intentionally left blank]

Contents

Acknowledgements vii

Abstract ix

Resumo xi

List of Tables xv

List of Figures xxi

1 Introduction 1

2 Fast Radio Bursts (FRBs) 3

2.1 Overview . . . 3

2.2 Main properties . . . 4

2.2.1 Detection and localization . . . 4

2.2.2 Distance estimation . . . 6

2.2.3 Rate of occurrence . . . 9

2.2.3.1 Repeating FRBs . . . 11

2.2.4 Energetics . . . 12

2.3 Source models for FRBs . . . 12

2.4 Emission models based on magnetars . . . 14

2.4.1 Magnetar properties . . . 15

2.4.2 Magnetars as a source of FRBs . . . 17

2.4.3 Galactic FRB - FRB 200428 . . . 17

2.4.4 High energy particles as counterparts of FRBs . . . 19

2.4.4.1 Baryon loaded shock scenario . . . 21

2.5 High-energy multimessenger studies with FRBs . . . 23

3 High energy astroparticles and their detection 26

3.1 High energy astroparticle detectors . . . 26

3.2 Extensive atmospheric showers . . . 29
3.2.1 The Heitler model for electromagnetic showers . . . 29
3.3 The Pierre Auger Observatory . . . 31
3.3.1 General description of the observatory . . . 32
3.3.2 Surface detector . . . 34
3.3.3 Fluorescence detector . . . 35
3.3.4 Upgrades . . . 35
3.3.4.1 SD-433 . . . 36
3.3.5 Event reconstruction . . . 37
3.3.6 Photon detection . . . 38
3.3.7 Neutrino detection . . . 38

4 Multimessenger Study for FRBs **40**
4.1 High-energy photons as FRB counterparts . . . 40
4.1.1 Sensitivity studies with the Pierre Auger Observatory . . . 42
4.1.1.1 Spectral photon fluence . . . 43
4.1.1.2 Assumptions and considerations in the analysis . . . 45
4.1.1.2.1 Perfect trigger and reconstruction efficiency . . . 46
4.1.1.2.2 Perfect discriminant power . . . 47
4.1.1.3 Exposure . . . 48
4.1.1.4 Upper limit to the flux normalization factor at 90% CL . . . 48
4.1.1.5 Upper limit to the spectral photon fluence at 90% CL . . . 49
4.1.1.6 Introducing a realistic trigger efficiency . . . 50
4.1.1.6.1 Effect of the zenith angle . . . 51
4.1.1.6.2 Effect of the time interval . . . 54
4.1.2 FRB localization and Auger's field of view . . . 58
4.1.3 Sensitivity studies considering other observatories . . . 59
4.1.4 Sensitivity to stack analysis using catalogued FRB events . . . 63
4.2 High-energy neutrinos as FRB counterparts . . . 66

5 Conclusions and Outlook **68**

Appendices **70**

Bibliography **71**

List of Tables

2.1 List of galactic magnetars, where sources in bold have had giant flares, sources in italics are candidates only and sources in parentheses are normally rotation-powered pulsars. For each magnetar the table gives (from left to right), the period (P), the spin-inferred magnetic field strength (B), the characteristic age, the spin-down luminosity ($\dot{E}$), the distance (D), the quiescent luminosity in the 2–10-keV band for the distance provided (L_X), and the frequency band of the found counterpart, OIR=Optical/Infrared counterpart, R=Radio counterpart. H=Hard X-rays detected [70]. 18

3.1 Multimessenger detectors, separated between the four principle signals for multimessenger detection: electromagnetic radiation (EM); high energy neutrinos (HEN); ultrahigh energy cosmic rays (UHECR); gravitational waves (GW). They are further separated into current, in construction and proposed detectors, which may not be completely up to date (reference from 2019)[93]. 27

4.1 Values of the parameters a and b of Eq. 4.22 fitted to simulated events generated with energies between $10^{16} - 10^{17}$ eV. 46

4.2 Properties of high energy photon detectors, namely, the area, energy range, localization and maximum/minimum declination of the field of view of the detector for $\theta < 45°$ for the SD-433 of the Pierre Auger observatory [109], HAWC [101], SWGO [103], and LHAASO [102]. 60

4.3 Estimated exposure found for HAWC, LHAASO and SWGO for a 1 second analysis with initial zenith angle $\theta \sim 15°$. 61

[This page was intentionally left blank]

List of Figures

2.1 Localization of 774 fast radio bursts plotted using equatorial coordinates, 191 of which are repeaters of ∼20 different sources. Catalog of FRBs after CHIME's FRB project detections were added to the TNS [43] accessed in June 2021. . . . 5

2.2 Localization of 290 fast radio bursts plotted using equatorial coordinates, 170 of which are FRB repeaters. Catalog of FRBs before CHIME's FRB project detections were added to the TNS [43] accessed in May 2021. 7

2.3 Fast radio burst dynamic spectra. The top panels show the total pulse intensity. The lower panels show the sweep of the burst across the time-frequency plane [8]. The time structure of the frequency allows for the estimation of the dispersion measure of a FRB. Left: FRB 010724, the first-reported FRB [11]. Right: FRB 110220, detected at Parkes [42]. 8

2.4 Dispersion measures plotted as a function of galactic latitude b for pulsars and FRBs. Dark blue: Galactic Pulsars (2422), light blue: Galactic pulsars associated with supernova remnants (27), light green: pulsars in the Large Magellanic Cloud (21), dark green: pulsars in the Small Magellanic Cloud (5) and red: FRBs (55) [8]. 8

2.5 Observed sky distribution of both apparent non-repeater and the first detected repeater events of FRBs from the first CHIME/FRB Fast Radio Burst Catalog [44]. Left: right ascension; right: declination. 10

2.6 Observed DM distribution of both apparent non-repeater and the first detected repeater events of FRBs from the first CHIME/FRB Fast Radio Burst Catalog [44]. Left: DM distribution; right: Extragalactic DM distribution. 10

2.7 Several estimates for the FRB rate above 5 Jy ms [44]. 11

2.8 Localization of 191 fast radio bursts, repeaters of ∼20 different sources, plotted using equatorial coordinates. Catalog of FRBs repeaters after CHIME's FRB project detections were added to the TNS [43] accessed in June 2021. 13

2.9 Localization of 31 magnetars plotted using equatorial coordinates. Source: Transient Name Server (TNS) [43] accessed in June 2021. In red, the localization of SGR 1935+2154, the magnetar directly associated with the galactic FRB, FRB200428. 16

2.10 Localization of FRB200428, and the galactic magnetar SGR 1935+2154. From the center outwards, the ellipses represent the 68.4%-, 90%- and 95%-confidence STARE2 localization regions of FRB 200428, the CHIME localization region corresponds approximately to the maroon circle and the known position of SGR 1935+2154 is shown as a black dot [40]. 19
2.11 Scheme for multimessenger emission in the baryon-loaded shock scenario, that predicts the emission of both FRBs and high energy neutrinos and photons, from a giant flare in a magnetar. 20
2.12 Baryon loaded shock scenario. At earlier times ($t \sim t_{\rm FRB}$) most of the pion-production will be by the thermal protons interacting with the synchrotron photons. At later times, $t \gg t_{\rm FRB}$, the particles interacting with the synchrotron photons will be the non-thermal protons. 23
2.13 Left: Observed neutrino spectra expected using the baryon load shock model for a fiducial burst of 1ms duration, $\nu = 1$ GHz and $\varepsilon_{\rm radio} = 10^{40}$ erg and distance of 0.1 kpc. Shown for comparison are also approximate IceCube sensitivity curves for observation windows of 30 ms and 17 s [59]. Right: Total γ-ray fluence due to neutral pion decay from the same fiducial burst now for a source at a distance of 0.1, 1, 10 and 100 kpc, compared to the sensitivities of the HAWC Observatory at 0° zenith angle [59]. 24
2.14 Baryon loaded shock scenario. Predicted neutrino properties for a sample of FRBs with measured properties as a function of the total flare energy (bottom axis) or approximate radio isotropic energy (top axis). The neutrino properties shown are $t_{\rm max}$, the duration of neutrino emission, $\varepsilon_{\rm max}\,[t_{\rm max}]$, peak neutrino energy, ε_ν, total neutrino energy radiated and F_ν, observed neutrino fluence. The FRBs shown include the sample of localized FRBs with known distances including two repeaters (different colors) and non-localized CHIME FRBs (gray points) [59]. 25

3.1 The three types of high energy photon detectors - Satellites, Cherenkov telescopes and EAS arrays [97]. 28
3.2 Representative image of an extensive air shower (EAS) producing signal in the surface array of the Pierre Auger Observatory. Credit: LIP 29
3.3 Schematic view of an electromagnetic cascade. Adapted from [106] and [107]. . 31
3.4 Map of the Pierre Auger Observatory. The red region represents the surface array (SD), with each dot corresponding to one of the 1660 surface detector stations. The four fluorescence detector enclosures are shown, each with the 30° field of view of its six telescopes. Also indicated are the two laser facilities, CLF and XLF, near the center of the observatory [109]. 33

3.5 Surface detector station or Cherenkov water tank. Left: Photograph of one of the stations. Right: Description of the main components of the tank [109]. . . . 33
3.6 Left: The Los Leones fluorescence detector enclosure. Right: Schematic view of a fluorescence telescope and description of its main components [109]. 34
3.7 Schematic map of the SD-433 array. The color represents to which matrix the water Cherenkov detector belongs. The red tanks are part of the SD-433 unitary cell, black belong to the SD-750 array and blue to the SD-433 upgrade [110]. . 36
3.8 Event reconstruction with the surface array. Scheme representation of the evolution of the shower front [109]. 37
3.9 Types of neutrinos in Auger. Credit: Roger Clay, University of Adelaide. . . . 38

4.1 Estimated number of 10^{16} eV photons predicted by the baryon loaded shock scenario as a function of the area of detection. In blue, for a source at d=10 kpc and in yellow, for a source at d=0.1 kpc. The red line marks the effective area of the SD-433. 41
4.2 Sketch of the hexagon composed by an internal tank surrounded by 6 neighbors of SD stations separated by 433 m and the corresponding effective area, which is the shaded hexagon around the central station, for a triangular grid. 44
4.3 Trigger efficiency curves of SD-433 in terms of the primary energy for simulated proton events of the Pierre Auger Observatory for different intervals of θ obtained from [117]. 45
4.4 Time evolution of the zenith angle, initially set as $\sim 15°$. The time evolution of the zenith angle depends on the declination of the source, which for this case is $\delta \sim -50.7°$. 49
4.5 Estimated upper limit to the flux normalization factor, k_γ^{UL}, arriving to the SD-433 in the Pierre Auger Observatory for 1 second considering perfect trigger efficiency for five bands within the energy interval $[10^{16}, 10^{17}]$ eV. 50
4.6 Estimated upper limit to the spectral photon fluence at 90% CL, $\mathcal{F}_\gamma^{UL}$, arriving to the Pierre Auger Observatory for 1 second considering perfect trigger efficiency for five bands within the energy interval $[10^{16}, 10^{17}]$ eV. In yellow is the reference value for the magnitude of the photon fluence predicted by the baryon loaded shock scenario for a source at d= 0.1 kpc, see Fig. 2.13. 51
4.7 Estimated upper limit to the spectral photon fluence, $\mathcal{F}_\gamma^{UL}$, at 90% CL for photon events arriving to the Pierre Auger Observatory with zenith angle $\theta \sim 15°$ for 1 second considering perfect trigger efficiency (in blue) and the trigger efficiency curves from [117] (in orange). 52
4.8 Exposure for photon events arriving to the Pierre Auger Observatory with zenith angle (θ) approximately 15°, 20°, 30°, 35° and 40° for 1 second. 53

4.9 Upper limit to the flux normalization factor, k_γ^{UL}, at 90% CL for photon events arriving to the Pierre Auger Observatory with zenith angle (θ) approximately 15°, 20°, 30°, 35° and 40° for 1 second. 53
4.10 Upper limit to the spectral photon fluence, $\mathcal{F}_\gamma^{UL}$, at 90% CL for photon events arriving to the Pierre Auger Observatory with zenith angle (θ) approximately 15°, 20°, 30°, 35° and 40° for 1 second. 54
4.11 Time evolution of the zenith angle (θ) for the transit of a source, for which the FoV initially comes closer until it reaches its minimum and then moves away. . 55
4.12 Exposure for photon events arriving to the Pierre Auger Observatory with zenith angle $\theta \sim 15°$ for 1, 100, 1000 and 10 000 seconds. 56
4.13 Estimated upper limit to the flux normalization factor, k_γ^{UL}, at 90% CL for photon events arriving to the Pierre Auger Observatory with zenith angle $\theta \sim$ 15° for 1, 100, 1000 and 10 000 seconds. 57
4.14 Estimated upper limit to the spectral fluence, $\mathcal{F}_\gamma^{UL}$, at 90% CL for photon events arriving to the Pierre Auger Observatory with zenith angle $\theta \sim 15°$ for 1, 100, 1000 and 10 000 seconds. In purple is the reference value for the magnitude of the photon fluence predicted by the baryon loaded shock scenario for a source at d= 0.1 kpc, see Fig. 2.13. 58
4.15 Localization of 774 fast radio bursts plotted using equatorial coordinates (source: Transient Name Server (TNS)). The shaded regions are the total region in the sky observed by the Pierre Auger Observatory (blue) and by LHAASO (pink) for $0° < \theta < 45°$ plotted using equatorial coordinates. 59
4.16 Fraction of a sidereal day for which the instantaneous field of view for zenith angles $\theta < 45°$ of the Pierre Auger Observatory covers a point in the sky as a function of its declination. 60
4.17 Estimated upper limit to the spectral fluence, $\mathcal{F}_\gamma^{UL}$, at 90% CL for photon events arriving to HAWC, LHAASO and SWGO with zenith angle $\theta \sim 15°$ for 1 second. In purple is the reference value for the magnitude of the photon fluence predicted by the baryon loaded shock scenario for a source at d= 0.1 kpc, see Fig. 2.13. 62
4.18 Localization of FRB 20181030E and the FoV of the Pierre Auger Observatory for the zenith angle (θ) interval of 0° to 45°, for the moment of detection. . . . 63
4.19 Stack analysis of the upper limit to the spectral fluence, $\mathcal{F}_\gamma^{UL}$, for photon events arriving to HAWC and LHAASO using catalogued FRB events for a 1 second analysis. Also represented is an estimate to the order of magnitude for the photon fluence for an extragalactic FRB with $\varepsilon_{radio} \sim 10^{40}$ erg and at typical distances of ~ 0.1 Gpc predicted by the baryon loaded shock scenario. 65

4.20 Localization of the galactic FRB 200428 (black) and the FoV of the Pierre Auger Observatory for different intervals of zenith angle (θ) at the moment of detection of the FRB. 67

[This page was intentionally left blank]

1 Introduction

Astroparticle physics is a relatively recent field of study that relies on the detection of not only photons but also of a variety of different particles from astrophysical sources. After photons, which have been studied for centuries, the first of these different particles to be detected were cosmic rays. They were discovered when, in 1912, Victor Hess took electrometers in a ballon to high altitudes, up to 5 km, and showed that in addition to the expected terrestrial component of ionizing radiation, there was a source of ionizing radiation which increased in intensity with altitude. Two years later, the development of a cloud chamber, by Kohlhörster, confirmed the existence of the extraterrestrial component. Today, we know that cosmic rays are charged particles - high energy atomic nuclei - that move through space at nearly the speed of light and may reach ultra-high energies, above the scale of EeV [1].

In 1967, solar neutrinos were detected in the Homestake Mine experiment [2]. The detection of neutrinos revolutionized how one sees astronomical objects, since they provided a whole new way to study them. The Kamioka Nucleon Decay Experiment (Kamiokande), in 1987, became the first experiment detecting neutrinos and their arrival direction, meaning that it was now possible to "see" the Sun through its neutrino emission. The Kamiokande experiment also documented the explosion of a supernova in the Large Magellanic Cloud, in the same year, by detecting its neutrino burst.

Another breakthrough came with the first observation of a gravitational wave on 14 September 2015 by the LIGO and Virgo collaborations [3]. This was also the first observation of a binary black hole merger, demonstrating both the existence of binary stellar-mass black hole systems and the fact that such mergers could occur within the current age of the universe. At this point, there are several studies trying to associate neutrinos to gravitational waves [4, 5, 6].

Electromagnetic signals, from the entire electromagnetic spectrum, are also essential in multimessenger astrophysics with a lot of studies being complemented by the information they provide. An electromagnetic burst, which has awaken a lot of interest in recent years, are gamma ray bursts (GRBs). These GRBs are cosmological signals originating from the most luminous explosions in the universe, with typical isotropic luminosities of $\sim 10^{51} - 10^{53}$ erg s^{-1}. They are believed to be also sources of non-electromagnetic radiation, namely of high energy neutrinos, cosmic rays and gravitational waves [7].

The discovery and detection of all these signals led to the birth of a new field of astrophysics

called **multimessenger astrophysics**, where one tries to understand astrophysical objects and their emissions through the detection and association between different types of signals being emitted/accelerated by a single source/system. This new way to study such complex and mysterious objects allowed for a much more complete manner to observe the sky, as was the case of the multimessenger observation of a neutron star merger which was a joint effort between multiple collaborations [4].

A very important discovery in the field of Astronomy and Astrophysics came with the detection of a radio signal from a pulsar by Jocelyn Bell in 1967. First dismissed as radio interference, these periodic signals later came to be associated with a fast rotating neutron star called pulsar. A more recent discovery surrounding radio transients - the detection of a fast radio burst (FRB), an extragalactic radio signal - was followed by a wave of fascination with the millisecond signals. These bursts, although in a lot of ways similar to pulsar pulses, have an estimated energy at the source which is at least 9 orders of magnitude larger.

This work intends to study the possible experimental association between the recently discovered FRBs and other astrophysical messengers, such as high energy photons and neutrinos. For this effect, we first take a look at FRBs, their properties and the possibility of the emission of high energy counterparts. Then, we review the mechanisms of detection of the high energy counterparts, such as photon and neutrinos, using the Pierre Auger Observatory as the case of study to conduct this analysis. Lastly, we conduct a follow-up analysis to estimate the sensitivity of the detector to high energy photons emitted with FRBs, in order to constrain a particular theoretical emission model for FRB counterparts. We begin by studying the detection of high energy photons, estimating the upper limit to the spectral photon fluence at 90% confidence level for the Pierre Auger Observatory. Then, we perform the same estimate for other detectors, namely HAWC, LHAASO and SWGO, and compare the results. After, we do a stack analysis using catalogued FRB events for HAWC and LHAASO using the corresponding exposure of each observatory at the time of detection. We end with a brief discussion on the analysis for high energy neutrino counterparts to be followed either through the Pierre Auger Observatory or using other neutrino detectors.

2 Fast Radio Bursts (FRBs)

2.1 Overview

As already mentioned, FRBs are millisecond radio bursts typically from an extragalactic population of sources. After assuming an isotropic distribution of the sources emitting these signals, the estimated rate of fast radio bursts over the entire sky is of thousands per day [8].

These radio transients have been detected at frequencies ranging between 300 MHz - 8GHz by ground-based radio telescopes. Their radio-frequency (ν) dependent arrival times are consistent with a radio wave going through a cold plasma [9, 10].

The first extragalactic fast radio burst to be identified, FRB010724, was detected on the 24th of July 2001 [11]. It consisted of a 30 Jy [1] dispersed radio burst of duration < 5 ms. Its dispersion measure (DM) (see eq. 2.1) DM$= 375$ cm^{-3}pc, was consistent with the burst having an extragalactic origin [11].

There are several different aspects regarding fast radio bursts that lead us to believe that there are different internal classes, each created by a different source, with possibly different mechanisms of emission. One is the fact that FRBs have been measured to have both circular [12, 13, 14] and/or linear [15, 16, 17] polarizations, and some appear unpolarized, which may be due to extremely high Faraday rotation [17]. Another clue is the variability of pulse profiles of fast radio bursts - a few have double or triple peaks [18], whereas most detected FRBS have one single peak. Many FRBs also possess complex microstructures in their profiles [19]. There are some that are known to repeat, like FRB 121102 [20] or FRB 180814.J0422+73 [21]. Additionally, there is a lot of variability in regards to the periodicity of the repeating FRBs. This important facet will be explored in the subsection 2.2.3.1.

Fast radio bursts are powerful tracers of the circumsource environments, of the properties of the intergalactic medium (IGM) [22, 23, 24] and of dark matter distribution [25, 26, 27]. In fact, they are used in a vast variety of studies, such as to probe magnetized plasma, which gives an unique opportunity for remote sensing of the extreme environments around burst sources, their host galaxies and the IGM [28]. This probing can result in, for example, the constraint of the local DM and new models for cosmological magnetic fields using large FRB samples [28].

Fast radio burst detections are also useful for imposing constraints on microlensing [29, 30],

[1] Jansky (Jy) - unit of spectral flux density which in SI is measured in W m^{-2} Hz^{-1},1 Jy=10^{-26}Wm^{-2}s^{-1}Hz^{-1}.

placing limits on photon mass [31, 32], studying fundamental cosmological parameters [33, 34], testing Einstein's Equivalence Principle [35, 36] and for studying the cosmic web [37], cosmic microwave background (CMB) optical length [38] and superconducting cosmic strings [39].

Additionally, since these signals travel such large distances, the observed fluence, compared to a pulse from a galactic pulsar, for example, implies that the radiation energy densities at the source are about ten billion times larger than the latter. This fact alone led to great mystery and scientific interest in fast radio bursts and their possible sources.

To explain such high energy densities at the source, various new or known exotic objects in extreme circumstances where proposed as responsible for the emission. In fact, the wide range of models covered almost everything, from alien spacecrafts to cosmic strings [8]. However, those concerning compact objects are the ones that gained most attention. From these models, a recurring object is a particular type of neutron star called a magnetar. This particular star, as a source of FRBs, will be discussed in more detail ahead.

A very important development in fast radio burst research came with the discovery of a FRB associated with a galactic magnetar [40]. This particular discovery was a critical point in the study of these transients as it, for the first time, directly associated a FRB with its source. It also meant the discovery of a galactic radio burst and the smaller distances traveled can mean considerable differences in the studies we are able to perform and the experimental results we expect, as we will see later on. Thus, a rapidly rotating magnetar is a promising explanation as the source of FRBs. Nonetheless, alternative source models are not ruled out since, as was already mentioned, there are likely different classes of FRBs with different objects or systems as sources. This idea has been recently reinforced by the localization of the repeating FRB 180916.J0158+65 and its association to a star-forming region in a nearby (redshift 0.0337 ± 0.0002) massive spiral galaxy [41]. The lack of both a persistent radio counterpart and a high Faraday rotation measure distinguishes this burst from the only previous repeating FRB localized in association with an object, FRB 121102.

2.2 Main properties

2.2.1 Detection and localization

FRBs are, in many aspects, very similar to pulses from Galactic radio pulsars and the surveys responsible for their detection are also identical, both done using ground-based radio telescopes. The detection is made through high time resolution spectra ($\sim 100\ \mu$s) with ~ 1000 frequency channels across a total bandwidth of hundreds of MHz [8].

The first fast radio bursts detected presented relatively simple temporal structures, typically being Gaussian-like pulses modified, in some cases, by scatter broadening [11, 42]. However, these first surveys were limited in their conclusions by the time resolution of post-detection dedispersion. More recent work showed that FRBs can present quite complex t-ν structures

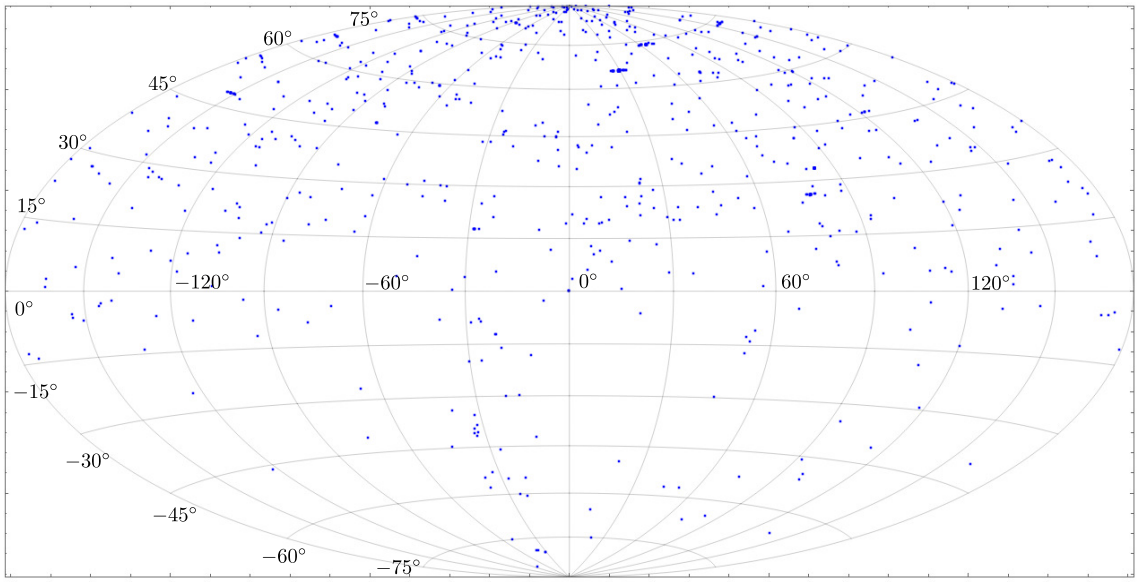


Figure 2.1: Localization of 774 fast radio bursts plotted using equatorial coordinates, 191 of which are repeaters of ∼20 different sources. Catalog of FRBs after CHIME's FRB project detections were added to the TNS [43] accessed in June 2021.

that are distinguishable from single pulses from pulsars [18, 19].

To this day, almost 800 fast radio bursts have been detected, according to the online FRB catalogue: Transient Name Server (TNS) [43]. In Fig. 2.1, we can see a sky map with the localization of 774 FRBs, plotted in equatorial coordinates. We clearly see that there are more fast radio bursts detected in the northern hemisphere, and this is because approximately 500 burst detections were added to the FRB catalog coming from the Canadian Hydrogen Intensity Mapping Experiment Fast Radio Burst (CHIME/FRB) Project [44]. CHIME is a transit telescope operating between 400–800 MHz that is responsible for discovering a considerable part of both repeating and non-repeating FRBs.

Most of the FRB events found in the southern hemisphere have been detected by the Parkes and ASKAP surveys carried out from Australia. There also have been FRB surveys conducted by LOFAR/ARTEMIS, GBT/GBNCC and UTMOST. For more information on FRB surveys check Ref. [8].

Before this huge release of FRB events by CHIME, the FRB catalog counted with $\sim$ 300 fast radio burst events. The fast developments in regards to FRB detection are, indeed, quite clear. Not so long ago, in 2019, the reference number for FRB detections was only 54 [45]. This rapid evolution can prove to be revolutionary in the study of fast radio bursts as the lack of statistic was one of the biggest obstacles in understanding these mysterious signals, specially when we consider the diversity of properties associated with them. One way in which this effort by CHIME already payed off concerns the detection of the galactic FRB200428 and the

direct association with its source, a magnetar [40]. This experiment, with the largest number of FRBs detected using a single telescope and detection pipeline, is an unique opportunity to study FRB property distributions, since past experiments have been hampered by using FRBs from multiple surveys with very different operational parameters. Some of the important analyses coming from this catalog will be discussed below.

There is already a study on the morphology of the bursts coming from the CHIME collaboration, where the bursts were separated into four categories: "simple broadband", "simple narrowband", "temporally complex" and "downward drifting". Additionally, they were able to detect a morphological difference, on average, between the repeating and non-repeating bursts, which could be attributed to propagation effects or intrinsic to the population [46]. There is also a study searching for statistical cross-correlations of the results of the first CHIME/FRB Catalog with large-scale structure [47]. In this study, it was found that there is a significant angular cross-correlation between CHIME/FRB sources and galaxies in the redshift range $0.3 \lesssim z \lesssim 0.5$. Therefore, we expect the use of high duty cycle, wide-field arrays to mark a new phase in our understanding of fast radio bursts and their emitters.

When we look at only the first 300 events, plotted in a sky map in equatorial coordinates, we can see that the events do not appear to be uniformly distributed, Fig. 2.2. There are a few points in the sky where there are several FRB detections with similar declinations but slightly different right ascensions. Also, there is an accumulation of detections at right ascension $\sim 45°$ - both are due to experimental bias [8]. The distribution of the population of detected FRBs will be addressed later.

Of the detected events, only a few have secure localizations, and some of these are thanks to cross detections between different detectors and to counterparts found. Namely, FRB 121102, that was the first FRB known to repeat and was monitored by the Very Large Array in a fast-dump recording mode [48]. This effort resulted in the discovery of a persistent radio and optical counterpart and the localization of the event on a sub-arcsecond scale [49]. The source of this FRB was identified as a low-metallicity star-forming dwarf galaxy at redshift 0.19273(8), with the persistent radio counterpart offset from the center of the galaxy [50]. Other FRBs, like the previously mentioned FRB 180916.J0158+65, have been localized by radio interferometers and associated to host galaxies with known distances. Their luminosity distances range between 149 Mpc and 4 Gpc [51, 52].

One notable case of a precise localization of a fast radio burst was already mentioned and came with the detection by CHIME of FRB 200428 and the direct association with its source, a galactic magnetar, SGR 1935+2154 [53].

2.2.2 Distance estimation

A very important characteristic of this class of radio transients is that the arrival time of the frequency (ν) components is dispersed following the so-called DMν^{-2} scaling law expected

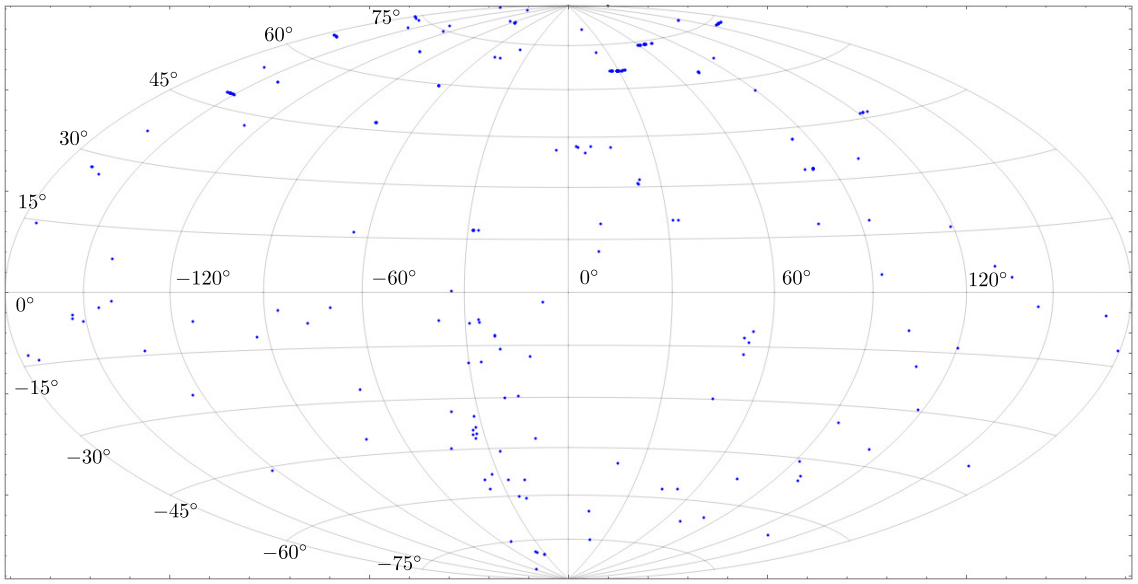


Figure 2.2: Localization of 290 fast radio bursts plotted using equatorial coordinates, 170 of which are FRB repeaters. Catalog of FRBs before CHIME's FRB project detections were added to the TNS [43] accessed in May 2021.

for a cold plasma, where

$$\mathrm{DM} = \int_0^d n_e \mathrm{ds} \tag{2.1}$$

is the dispersion measure, which measures the total electron column density, n_e, along the line of sight to the source at a distance d. This relation was already applied to pulses coming from pulsars and is used for estimating the distances traveled by these pulses after emission. The same reasoning was administered to fast radio bursts. In Fig. 2.3, we can see the dynamic spectra for two different FRB detections, both the total pulse intensity and the sweep of the burst across the time-frequency plane for the first ever detected FRB 010724 and the repeating FRB 110220.

Figure 2.4 shows dispersion measurements for galactic pulsars, pulsars in the Magellanic Clouds and FRBs as a function of the galactic latitude b. The dispersion measurements of all fast radio bursts with $|b| > 10°$ are much larger than any Galactic pulsar for the same latitude. So, an extragalactic population of FRBs could present this behavior if the total DM includes a large extragalactic contribution. Therefore, these detections are too large to be galactic DMs which led to the conclusion that these signals are, in fact, extragalactic [42].

The FRB dispersion measures vary between ~ 100 and 2600 pc cm^{-3} that is comparable to the range for pulsars, ~ 3 and 1700 pc cm^{-3}, which means that, in the latter case, most of these contributions are due to the ISM of the Milky Way and of the Magellanic clouds. The smallest DMs from FRBs are in agreement with an extragalactic component like what we would expect for a dwarf galaxy. This conclusion is straightforward from Fig. 2.4 at the DMs corresponding

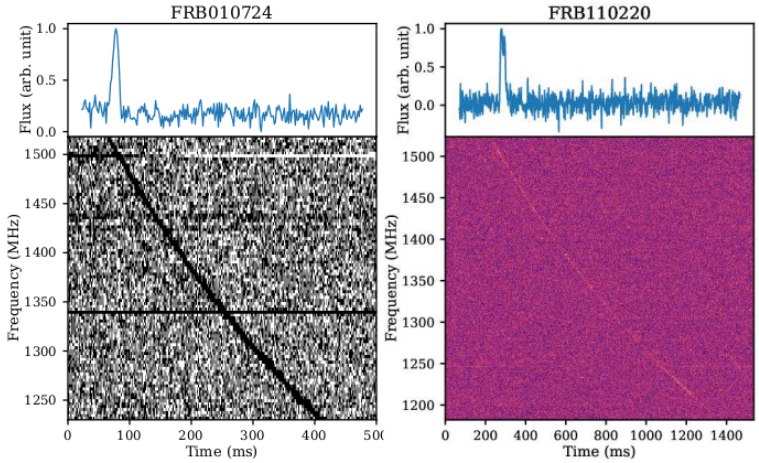


Figure 2.3: Fast radio burst dynamic spectra. The top panels show the total pulse intensity. The lower panels show the sweep of the burst across the time-frequency plane [8]. The time structure of the frequency allows for the estimation of the dispersion measure of a FRB. Left: FRB 010724, the first-reported FRB [11]. Right: FRB 110220, detected at Parkes [42].

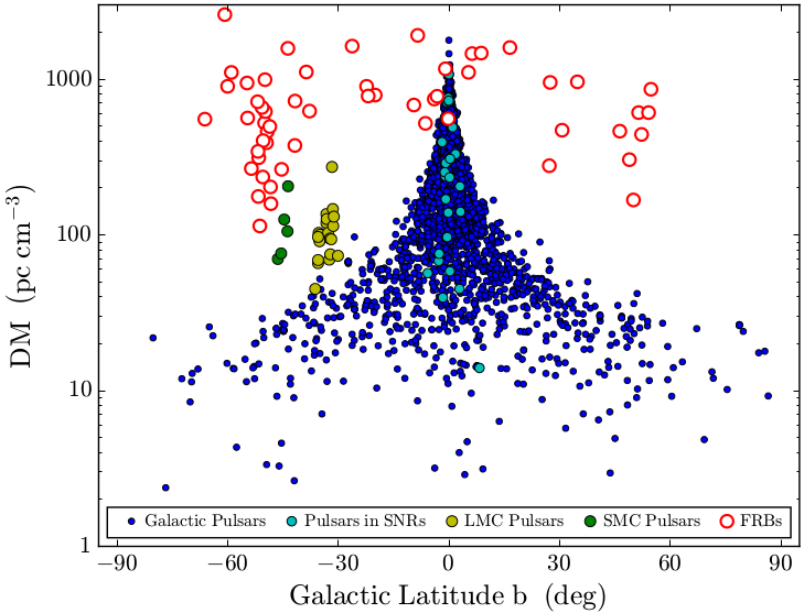


Figure 2.4: Dispersion measures plotted as a function of galactic latitude b for pulsars and FRBs. Dark blue: Galactic Pulsars (2422), light blue: Galactic pulsars associated with supernova remnants (27), light green: pulsars in the Large Magellanic Cloud (21), dark green: pulsars in the Small Magellanic Cloud (5) and red: FRBs (55) [8].

to pulsars in the Magellanic clouds. The largest DMs are similar to those expected from either a long path through the IGM or a galaxy disk, or a young supernova remnant [8]. Hence, ionized gas is a probable source for the extragalactic component of the dispersion measure for FRBs. When looking at Fig. 2.4, it appears that there is an acumulation of FRB events at $|b| \sim 50°$, which happens because the survey that detected 20 of the represented events, ASKAP, had a very narrow range of galactic latitudes, $|b| = 50° \pm 5°$ [8].

FRBs are estimated to originate at characteristic distances of hundred megaparsecs to tens gigaparsecs. An exception is the galactic FRB, with its source at an estimated distance of only ~ 10 kpc.

2.2.3 Rate of occurrence

As already mentioned, to date, there have been almost 800 fast radio burst detections, of which 191 are repeaters of ∼20 different sources. In order to estimate the rate of FRBs in the sky one has to assume a given sky distribution.

The sky distribution of FRBs has been typically assumed to be uniform. Notwithstanding, there have been analyses that seem to assume a latitude dependence and others that argue against it. Since the studies supporting these conclusions are based on low statistics (20 objects), this dependence was, until recently, still unclear.

More recently, June 2021, the analysis coming from the first CHIME/FRB Fast Radio Burst Catalog, with large statistics, separates the sky distribution for FRB - non-repeaters and FRB - repeaters, specifically in their right ascension and declination distributions. It was concluded that both classes of FRBs have sky distributions consistent with uniform distributions. Therefore, they are statistically consistent with having come from the same underlying sky distribution, see Fig. 2.5. Nevertheless, we have to point out that the conclusions on the first repeaters are still based on low statistics.

From Fig. 2.5 we can also see that the CHIME/FRB detector views the entire sky north of declination $-11°$ every day [44].

Another relevant analysis performed by CHIME using the new FRB catalog is to understand if the distribution of the DMs for the non-repeaters is the same as for the repeaters. It was concluded that both classes are statistically consistent with having come from the same underlying distribution, see Fig. 2.6. This study is particularly interesting because it investigates the hypothesis of repeaters and non-repeaters being separate classes of FRBs, i.e., originated from different objects or systems. So, if the extragalactic DMs are dominated by plasma in the intergalactic medium, then this result suggests no disparity between the distribution or host type of repeaters and non-repeaters. Furthermore, if the extragalactic DMs are dominated by the host's ISM, or its local environment, then the repeaters and non-repeaters must share similar host properties.

Even with the sudden increase of FRB detections in the last few years, the total number

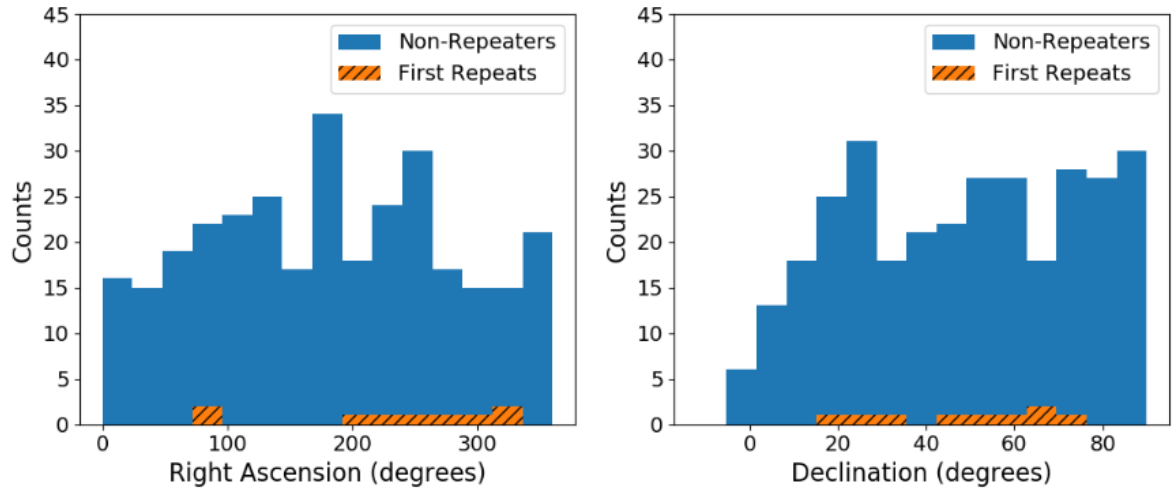


Figure 2.5: Observed sky distribution of both apparent non-repeater and the first detected repeater events of FRBs from the first CHIME/FRB Fast Radio Burst Catalog [44]. Left: right ascension; right: declination.

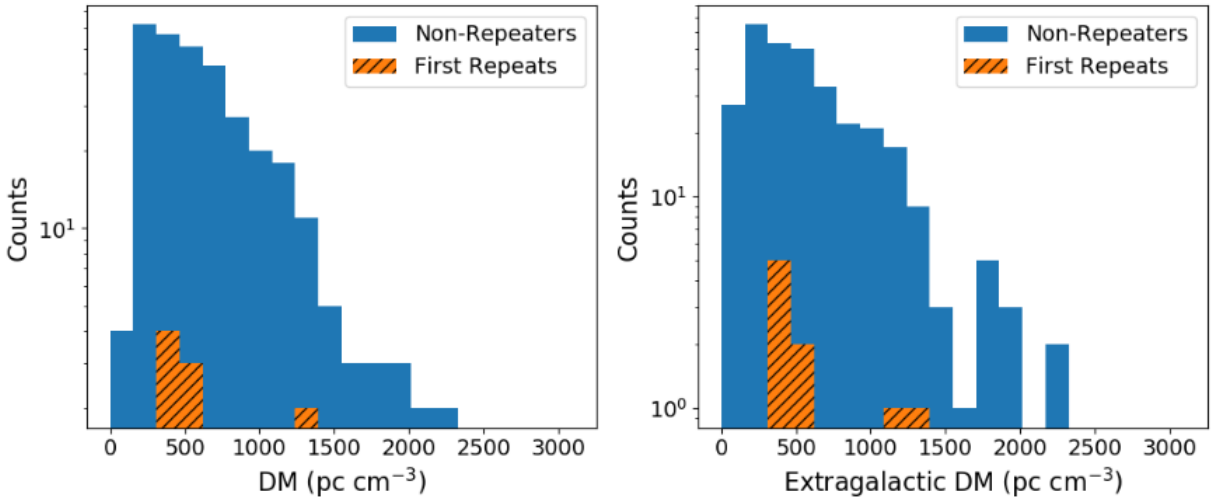


Figure 2.6: Observed DM distribution of both apparent non-repeater and the first detected repeater events of FRBs from the first CHIME/FRB Fast Radio Burst Catalog [44]. Left: DM distribution; right: Extragalactic DM distribution.

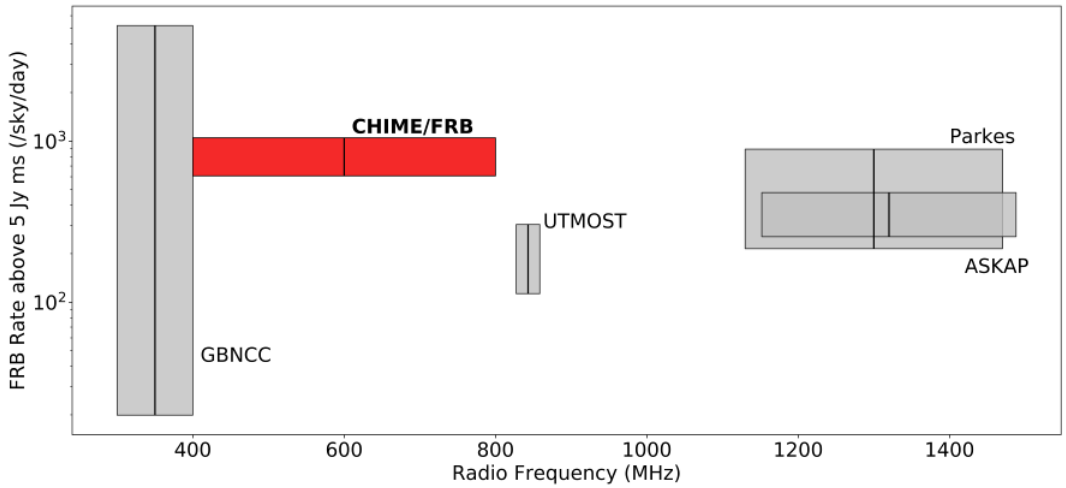


Figure 2.7: Several estimates for the FRB rate above 5 Jy ms [44].

of FRB detections does not yet compare with the statistics of pulses coming from pulsars, for example. However, when we consider an uniform distribution, and integrate the number of FRBs over the entire sky, the rate of FRBs is of the order of 1000 per day, which is a considerable number. The last result obtained from the first CHIME FRB catalog to be here discussed is exactly the updated sky rate for fast radio bursts. This measurement is actually different from the previous ones, as it corresponds to a lower frequency band of 400-800 MHz, whereas older surveys, generally using the Parkes and ASKAP telescope samples, had been in the 1.4 GHz band.

The estimated sky rate in the 300–400 MHz range from GBNCC surveys is $3.4^{+15.4}_{-3.3} \times 10^3\,\mathrm{day}^{-1}$ above a flux of 0.42 Jy, for a 5 ms pulse [54]. For the 400-800 MHz band the estimated rate using the CHIME/FRB Catalog 1 is $818 \pm 64^{+220}_{-200}\,\mathrm{day}^{-1}$ for a fluence limit of 5 Jy ms [44]. At 843 MHz and using six FRB events detected with Molonglo/UTMOST we have a reported rate of $98^{+59}_{-39}\,\mathrm{day}^{-1}$, for a fluence above 8 Jy ms [55]. For a frequency of 1.4 GHz, we present two different rate estimates: for a fluence limit of 2 Jy ms and based on Parkes 1.4-GHz FRB surveys the reported rate is $1.7^{+1.5}_{-0.9} \times 10^3\,\mathrm{day}^{-1}$; with the ASKAP FRB surveying, the reported rate is $37 \pm 8\mathrm{day}^{-1}$, above 26 Jy ms.

The CHIME collaboration organized these 5 reported rates by scaling them to a fluence limit of 5 Jy ms, the result can be found in Fig. 2.7. There, we see the different sky rates plotted for their respective frequency bands. We can see that the rate appears to decrease with both the frequency and the spectral flux.

2.2.3.1 Repeating FRBs

Some FRBs have been known to repeat and the first detected repeating FRB was FRB 121102 [56]. To this day there are 191 repeating fast radio bursts emitted from ∼20 different

sources, see Fig. 2.8, where only one of them is found in the southern hemisphere. However, the behavior of repeaters continues to be quite unpredictable. Most FRBs do not seem to ever repeat as some FRB lines of sight have been re-observed for more than 1000 h without any re-detections, which further supports the idea that repeaters and non-repeaters may differ in physical nature. Nonetheless, even within the FRBs that do repeat there is great diversity in behavior. There are FRB sources with only two detections and others with more than 10, most with no apparent periodicity. Yet, recently, the repeating FRB 180916 was shown to exhibit a 16 day period [57].

Until recently, it was difficult to classify and understand patterns in FRB properties because of the lack of statistics, specially when repeating sources where concerned. The large CHIME/FRB catalog allowed a much more complete analysis of the nature of repeaters versus non-repeaters, as it measured burst properties in a systematic, uniform way. The comparison between the sky and DM distributions showed that repeaters and non-repeaters appear to belong to the same underlying distribution. Additionally, if we look at signal strength or scattering properties of repeaters and apparent non-repeaters, we find no strong evidence for differences. However, when one compares the burst time widths and frequency bandwidths, it happens that the distributions for each FRB class possess strong differences. On average, repeaters have significantly broader widths and narrower bandwidths in the CHIME band. The CHIME collaboration suggests that these differences are strongly suggestive of differing emission mechanisms. The idea is that this could either be due to repeaters and apparent non-repeaters being from different source populations, or to a single population in which pulse morphology strongly correlates with the repetition rate [58].

2.2.4 Energetics

One peculiar facet regarding FRBs is the energy density associated with the burst, which is ten billion times larger than the typical energy density for a pulse from a Galactic radio pulsar, which means that finding a system that accounts for such energetics will be difficult. More likely than not, such energetic emission will not be emitted alone and the total energy associated with the emissions can be far greater than the FRB alone. The estimated radio energy emitted at the source for the population of FRBs typically ranges from $E_{\text{radio}} \sim 10^{37} - 10^{41}$ erg [59], whereas for the galactic FRB, the approximated energy is $\sim 10^{35}$ erg.

2.3 Source models for FRBs

There are many models proposed to explain such mysterious phenomenon as FRB emission. To justify the extreme fluence of FRBs upon emission, an equally exotic object/system must be considered. Even though there is great variability in the properties of the proposed models, there are a few key FRB characteristics that must be explained, or at least be possible, within

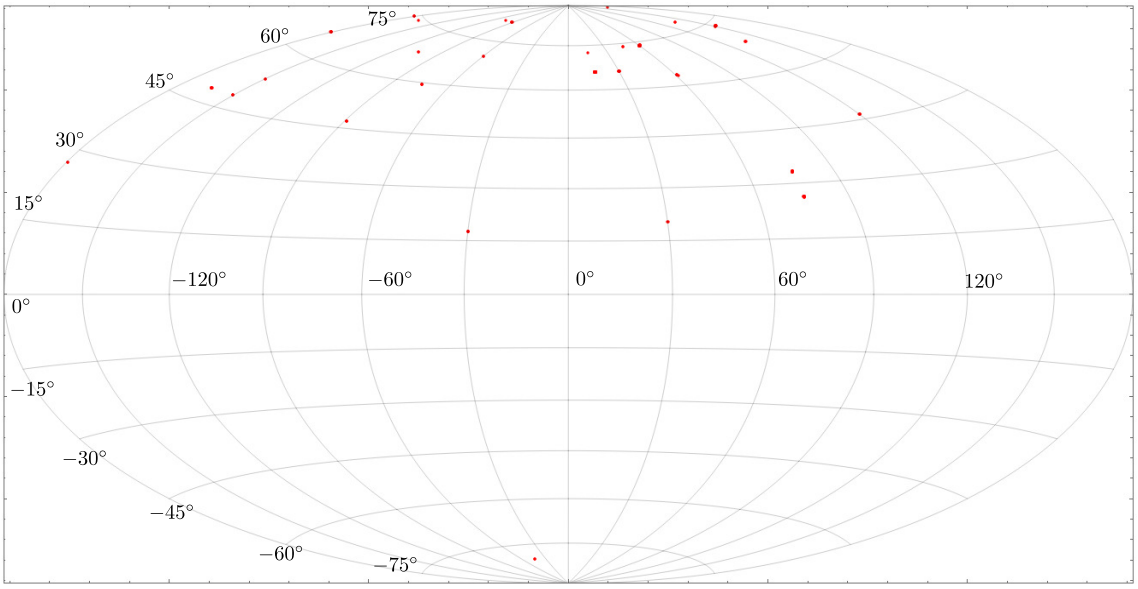


Figure 2.8: Localization of 191 fast radio bursts, repeaters of ∼20 different sources, plotted using equatorial coordinates. Catalog of FRBs repeaters after CHIME's FRB project detections were added to the TNS [43] accessed in June 2021.

the model. The most obvious is the amount of energy that must be associated with the emission. The brightness of the signal indicates that some beamed, coherent emission process is required and the brevity suggests the source is extremely compact [42].

The burst characteristics also need to be understood themselves, like duration of the signal, time-frequency structure, polarization and for the repeating FRBs, their low duty cycle, existence/absence of periodicity and rate variability. For all the FRB properties that seem to be heterogeneous, like polarization, for example, the emission model either explains the diversity upon emission, or attributes it to propagation effects or only attempts to describe the emission of a subset of FRBs.

We start by enumerating the main emission mechanisms employed to describe the creation of FRBs, as described in [45]. The main mechanisms are:

- Bremsstrahlung radiation, that occurs when an electron encounters a free ion and has its path bent, decelerates and consequently emits radiation;
- Atomic electron transition, where an electron bound to an atom emits electromagnetic radiation after dropping to a lower energy state;
- Synchrotron radiation, in which a charged particle moving in a magnetic field with some component of velocity perpendicular to the field will be forced to be on a helical trajectory and emit radiation. A charged particle moving along the bended magnetic field lines of a curved magnetic field will be accelerated transversely and will emit both

synchrotron radiation and another component called curvature radiation;

- Inverse Compton scattering, which happens when photons are scattered by ultra-relativistic electrons, creating photons with significantly higher energies.

The very short timescales of FRBs, of milliseconds, and the high energy associated, result in most of the proposed models assuming coherent radiation as result of the emission. Coherent radiation is either emitted by bunched particles accelerating along electromagnetic field lines, by masers, which arise from amplification of simultaneous electron phase transitions or by Dicke's superradiance, in which particles collectively undergo an atomic transition.

In [45], we find a very extensive theory catalog for FRB production. There, progenitor theories are organized into six different categories:

- compact object mergers/interactions;
- collapse of compact objects;
- supernova remnants;
- active galactic nuclei;
- collisions and close encounters;
- other models.

Therefore, most of fast radio burst models focus on either isolated or binary compact objects - white dwarfs (WD), neutron stars (NS) and black holes (BH) - or active galactic nuclei (AGN), perhaps interacting with a NS. Nonetheless, as already mentioned, the catalog of theories is extremely broad including models like technomarkers from extragalactic civilizations [60], superconducting cosmic strings [39], exploding black holes [61], reconnection in magnetars triggered by axion quark nuggets [62], WD-NS binaries [63], NS-NS mergers [64], WD-BH mergers that create reconnecting magnetic blobs [65], collapse of a supramassive NS [66], accretion or interaction of asteroids with compact objects [67], births of neutron stars or black holes, AGN-NS interactions and activity, like flares and starquakes from magnetars.

Magnetars are a class of massive neutron stars that, since the first FRB detections, have been pointed as a likely candidate for fast radio burst emission and the explanation will be discussed in section 2.4.

2.4 Emission models based on magnetars

Young, rapidly rotating neutron stars have, since the discovery of the first FRBs, been a particular focus of source models, considering that they are able to fill quite well the main

requirements associated to the FRB production. Neutron stars exist in sufficient number in the Universe to explain the estimated FRB rate and possess sources of free energy, rotational and magnetic, that can account for the burst energetics. They are compact sources which can account for the coherent emission. Moreover, magnetars are extremely dynamic stars, losing energy very rapidly in the beginning of their lives, and are known for periods of magnetospheric activity, i.e, giant flares and outbursts.

Thus, this class of young neutron stars exhibits dramatic variability across the electromagnetic spectrum – particularly at X-ray and soft γ-ray energies – ranging from few millisecond bursts to major month-long outbursts. Additionally, there is still a lot of unknowns with respect to the extent of magnetar emissions, which in turn makes it quite difficult to identify a magnetar.

Typically, magnetars are identified from two different classes of neutron stars: soft γ-ray repeaters (SGRs) and anomalous X-ray pulsars. The majority of known magnetars were discovered via their short X-ray bursts. Therefore, there is a strong bias in the known magnetar population toward sources most likely to burst. They are also spinning down, with spin-down rates that imply spin-down time scales $\left(\sim\frac{P}{\dot{P}}\right)$, where P is the period of the star, of a few thousand years, suggesting great youth. So, similarly to pulsars, magnetars spin faster in the beginning of their life due to rapid magnetic braking. Yet, at the same time, the younger they are, the faster they slow down, meaning that young magnetars will be highly dynamic.

2.4.1 Magnetar properties

Right now there are only about 30 confirmed magnetars, all of them confined to the galactic plane, see Fig. 2.9.

To be able to reach hydrostatic equilibrium against its own gravitational pull, a white dwarf relies on the pressure of electron degeneracy [68]. For more massive stars the electron degeneracy is not enough to counterbalance the gravitational force and the star continues collapsing until it is the pressure of neutron degeneracy ensuring hydrostatic equilibrium. Neutron stars have as their most important characteristics their rotation, age, size and intensity of the magnetic field. We may understand the order of magnitude of some of these quantities for a typical NS through a few simple considerations.

Like white dwarfs, neutron stars obey the following mass-volume relation,

$$\mathrm{MV} = \text{constant}. \tag{2.2}$$

Thus, with increasing mass, neutron stars become smaller and denser. Neutron stars are extremely compact objects, much more than the already exceptionally dense white dwarfs. To give an idea, white dwarfs have a radius of $\sim 10^6$ m, whereas for neutron stars, the radius is expected to vary between approximately 10 and 15 km.

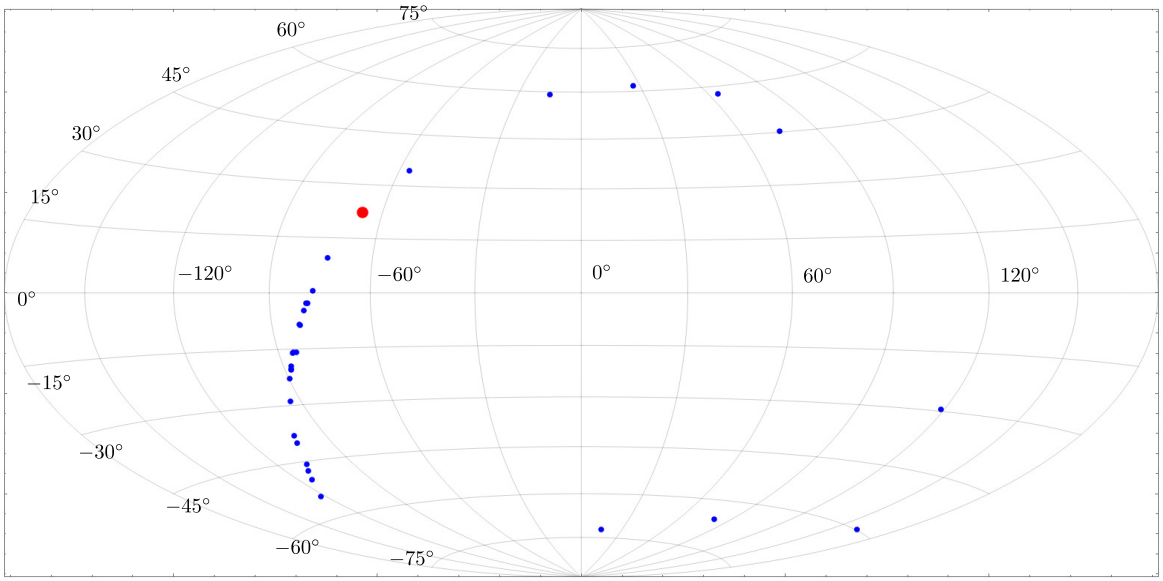


Figure 2.9: Localization of 31 magnetars plotted using equatorial coordinates. Source: Transient Name Server (TNS) [43] accessed in June 2021. In red, the localization of SGR 1935+2154, the magnetar directly associated with the galactic FRB, FRB200428.

One of the most identifiable characteristics of a neutron star is that it rotates rapidly. Even if the iron core of a pre-supernova star was rotating slowly, the decrease in radius is so big that the conservation of angular momentum ensures the formation of a rapidly rotating neutron star. If we consider the specific case of an iron core collapsing to form a neutron star, we have,

$$\mathrm{P_{NS}} \approx 3.8 \times 10^{-6} \mathrm{P_{core}}, \tag{2.3}$$

where $\mathrm{P_{core}}$ is the period of rotation of the core and $\mathrm{P_{NS}}$is the period of rotation of the neutron star [69]. For example, we can take the rotation period as the one observed for the white dwarf 40 Eridani B, $\mathrm{P_{core}} = 1350$ s, which results in a rotation period for the neutron star of 5 ms. Therefore, NS are rapidly rotating with rotation periods of the order of a few milliseconds.

Another very important characteristic of neutron stars is their very strong magnetic field. Alfvén's theorem, or the "freezing in" of magnetic field lines in a conducting fluid or gas implies that the magnetic flux through the surface of a white dwarf will be conserved as it collapses to form a neutron star. The flux of a magnetic field through a surface S is defined as the surface integral

$$\Phi \equiv \int_S \mathbf{B} \cdot \mathrm{d}\mathbf{A}, \tag{2.4}$$

where $\mathbf{B}$ is the magnetic field vector. If we ignore the geometry of the field, we get

$$B_i 4\pi R_i^2 = B_f 4\pi R_f^2. \tag{2.5}$$

For the initial strength of the magnetic field (B_i), in this estimation we will use the largest observed magnetic field for a white dwarf, $B_{WD} \approx 5 \times 10^4$ T. Then using the previous equation,

$$B_{NS} \approx B_{WD} \left(\frac{R_{WD}}{R_{NS}} \right)^2 \approx 10^{10} \text{T}.$$

Magnetars, being a class of more massive neutron stars, have an extremely high magnetic field ($> 10^{13}$ G), rapid rotation (spin period P $\sim$ ms), and typically are young ($\sim$ 100 - 1000 yr). In table 2.1, we can see a list of galactic magnetars and their main properties.

The spin-down rate and the current period of the magnetar are used to infer some of these properties, like the characteristic age, τ_c, the magnetic field strength, B, the moment of inertia, I, and the spin-down energy, $\dot{E}$, through the following expressions [71],

$$\tau_c(\text{seconds}) = \frac{P}{2\dot{P}}, \tag{2.6}$$

$$B(\text{gauss}) = 3.2 \times 10^{19} \sqrt{P\dot{P}}, \tag{2.7}$$

$$\dot{E}(\text{erg/s}) = 4\pi^2 I \dot{P} P^3. \tag{2.8}$$

2.4.2 Magnetars as a source of FRBs

Some magnetar emission models seem to be particularly good in explaining specific bursts like the repeating FRB 121102, see [72]. In this event, the bursts were also associated with a persistent source originating from the same structure and models involving a giant flare can account for many features of the bursts and also the associated persistent radio source (PRS). In the magnetar paradigm a great deal of diversity of FRB sources is expected from a range of ages, environments, and initial conditions of the sources.

Given the extreme properties of a magnetar, namely the intensity of their magnetic field, the periods of intense magnetospheric activity, like giant flares and outbursts, and the ensuing emissions and mechanisms of emission are still not well understood, they are strong candidates for FRB emission. So, it is not surprising that there are works dedicated to explaining how FRBs can be created by flaring magnetars [73, 74, 72, 75].

2.4.3 Galactic FRB - FRB 200428

FRB 200428 was detected on 28 April 2020 in the 1281–1468 MHz band. The millisecond-duration radio burst associated with the Galactic magnetar SGR 1935+2154 was observed with a fluence of $1.5 \pm 0.3 \times 10^6$ Jy ms [53]. This event is 30 times less energetic than the

Name[b]	P (s)	B[c] (10^{14} G)	Age[d] (kyr)	$\dot{E}$[e] 10^{33} erg s^{-1}	D[f] (kpc)	L_X[g] 10^{33} erg s^{-1}	Band[h]
CXOU J010043.1-721134	8.02	3.9	6.8	1.4	62.4	65	...
4U 0142+61	8.69	1.3	68	0.12	3.6	105	OIR/H
SGR 0418+5729	9.08	0.06	36000	0.00021	∼2	0.00096	...
SGR 0501+4516	5.76	1.9	15	1.2	∼2	0.81	OIR/H
SGR 0526−66	8.05	5.6	3.4	2.9	53.6	189	...
1E 1048.1-5937	6.46	3.9	4.5	3.3	9.0	49	OIR
(PSR J1119−6127)	0.41	4.1	1.6	2300	8.4	0.2	R/H
1E 1547.0-5408	2.07	3.2	0.69	210	4.5	1.3	O?/R/H
PSR J1622–4950	4.33	2.7	4.0	8.3	∼9	0.4	R
SGR 1627−41	2.59	2.2	2.2	43	11	3.6	...
CXOU J164710.2–455216	10.6	<0.66	>420	<0.013	3.9	0.45	...
1RXS J170849.0–400910	11.01	4.7	9.0	0.58	3.8	42	O?/H
CXOU J171405.7–381031	3.82	5.0	0.95	45	∼13	56	...
SGR J1745–2900	3.76	2.3	4.3	10	8.3	<0.11	R/H
SGR 1806−20	7.55	20	0.24	45	8.7	163	OIR/H
XTE J1810–197	5.54	2.1	11	1.8	3.5	0.043	OIR/R
Swift J1822.3–1606	8.44	0.14	6300	0.0014	1.6	>0.0004	...
SGR 1833–0832	7.56	1.6	34	0.32	...	...	...
Swift J1834.9–0846	2.48	1.4	4.9	21	4.2	<0.0084	...
1E 1841–045	11.79	7.0	4.6	0.99	8.5	184	...
(PSR J1846−0258)	0.327	0.49	0.73	8100	6.0	19	...
3XMM J185246.6+003317	11.56	< 0.41	> 1300	< 0.0036	∼7	< 0.006	...
SGR 1900+14	5.20	7.0	0.9	26	12.5	90	H
SGR 1935+2154	3.24	2.2	3.6	17	...	...	...
1E 2259+586	6.98	0.59	230	0.056	3.2	17	OIR/H
SGR 0755−2933	...	...	...	...	...	...	...
SGR 1801−23	...	...	...	...	...	...	...
SGR 1808−20	...	...	...	...	...	...	...
AX J1818.8−1559	...	...	...	...	...	...	...
AX J1845.0−0258	6.97	...	...	...	...	2.9	...
SGR 2013+34	...	...	...	...	...	...	...

Table 2.1: List of galactic magnetars, where sources in bold have had giant flares, sources in italics are candidates only and sources in parentheses are normally rotation-powered pulsars. For each magnetar the table gives (from left to right), the period (P), the spin-inferred magnetic field strength (B), the characteristic age, the spin-down luminosity ($\dot{E}$), the distance (D), the quiescent luminosity in the 2–10-keV band for the distance provided (L_X), and the frequency band of the found counterpart, OIR=Optical/Infrared counterpart, R=Radio counterpart. H=Hard X-rays detected [70].

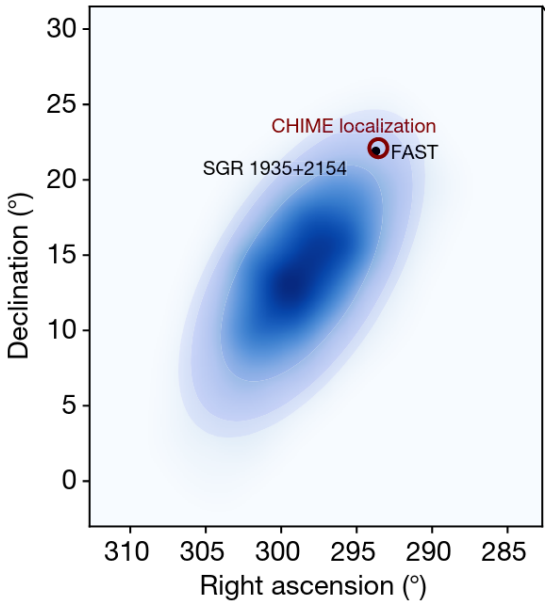


Figure 2.10: Localization of FRB200428, and the galactic magnetar SGR 1935+2154. From the center outwards, the ellipses represent the 68.4%-, 90%- and 95%-confidence STARE2 localization regions of FRB 200428, the CHIME localization region corresponds approximately to the maroon circle and the known position of SGR 1935+2154 is shown as a black dot [40].

weakest extragalactic FRB observed so far. However, because of the closeness of the source, the fluence is remarkably high. The estimated energy radiated by the burst in the $\sim$ GHz radio band is $\varepsilon_{\text{radio}} \sim 10^{34} - 10^{35}$ erg and it exceeds by several orders of magnitude that of any radio burst detected prior from a Galactic neutron star. In Fig. 2.10 we can see details of the detection, specifically the FRB's localization.

The discovery of FRB 200428 implies that active magnetars such as SGR 1935+2154 can produce FRBs at extragalactic distances. Additionally, the association of SGR 1935+2154 to FRB 200428 through the detection of a X-ray burst coming from the magnetar reinforces the idea that FRBs are originated from synchrotron masers or electromagnetic pulses powered by magnetar bursts and giant flares [40]. It is only expectable that a lot of future work in FRB modeling will be motivated by this important discovery. There are already a few examples of this, the FRB emission model we will be using as guide for the present analysis is one of them.

2.4.4 High energy particles as counterparts of FRBs

There have been multiple attempts to detect electromagnetic counterparts of FRBs. In the case of FRB 150418 and FRB 131104, counterparts were claimed but further analysis confirmed that neither emission was an FRB counterpart [76, 77]. For FRB 150418, a $\sim$ 6 day radio transient following the burst with emission consistent with a short gamma ray burst (sGRB)

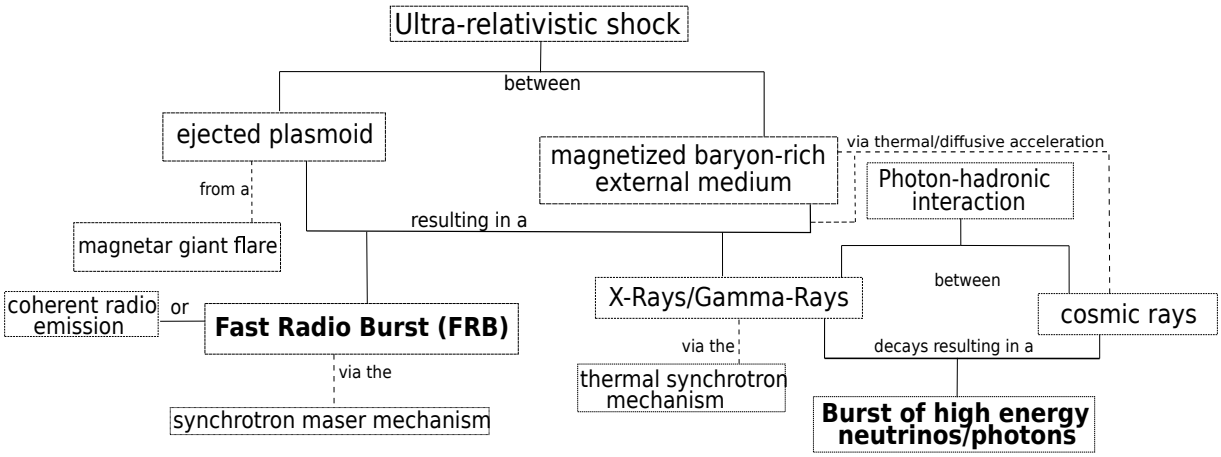


Figure 2.11: Scheme for multimessenger emission in the baryon-loaded shock scenario, that predicts the emission of both FRBs and high energy neutrinos and photons, from a giant flare in a magnetar.

afterglow was detected. Currently, the general consensus is that the two events are unrelated. For FRB 131104, a relatively long duration ($\sim$ 100 s) γ-ray transient, Swift J0644.5–5111, was observed shortly after the FRB. However, the lack of other counterparts suggests that this FRB is not associated with the GRB-like emission [45].

There are at least three cases where counterparts where confirmed:

- the repeating FRB 121102, with the PRS and optical counterpart which identified the galaxy of the source;
- the galactic FRB with the X-ray coming from SGR 1935+2154 [40, 53];
- FRB 180916.J0158+65 with simultaneous radio and X-ray observations [78].

It is to be expected that in the next few years the number of FRBs with known counterparts increases considerably, as the number of FRB detections and follow-up searches also increases. Actually, the field of FRB detection is advancing so rapidly that is possible that other counterpart detections already exist.

Such energetic signals motivate multimessenger studies, first because the objects responsible for FRB emission are very exotic and still surrounded by a blanket of mystery in what regards to mechanisms of emission. Furthermore, most of the models predicting the emission of fast radio bursts also predict the emission of other signals, not only the typical electromagnetic radiation but also gravitational waves (GWs), gamma-ray bursts (GRBs) and other high energy particles like cosmic rays (CRs) and neutrinos.

2.4.4.1 Baryon loaded shock scenario

The baryon loaded shock scenario is a theoretical model that explains the emission of both FRBs and high energy neutrinos and photons, from a flaring magnetar [74, 59]. The idea behind this model is that an ultra-relativistic shock powered by an ejected magnetically-dominated plasmoid, propagating into a magnetized baryon rich external medium, will simultaneously generate X-ray/gamma-rays via thermal synchrotron emission from electrons heated behind the shock, and coherent radio emission via the synchrotron maser mechanism (the fast radio burst emission). The neutrino/photon burst emission occurs from the photo-hadronic interaction between the previously generated X-ray/gamma-rays and relativistic ions, heated or accelerated at the shock. In Fig. 2.11 we show a scheme for this multimessenger emission model.

The baryon-loaded shock scenario explains the qualitative properties of FRB 200428 well, if one interprets the X-ray emission from the magnetar as incoherent synchrotron radiation from hot thermal electrons heated by the same shock that created the FRB.

In the context of this model, the ultra-relativistic blast by flare ejecta is coming from the magnetar with energy $\varepsilon_{\rm flare}$, and propagating into an external medium composed of electrons and ions, with a radial density profile, $n_{\rm ext}$, of the form

$$n_{\rm ext} \propto r^{-k}. \tag{2.9}$$

The inferred power-law indices of the external medium spans a wide-range $k \approx [-2, 2]$ for a set of detected FRBs of cosmological sources with known distances [74]. Therefore, for simplicity and as a generalization, a constant density medium (k = 0) is assumed. The qualitative results of this model are not, however, affected by this consideration. The radiative efficiency of the FRB emission is defined as

$$\eta \equiv \frac{\varepsilon_{\rm radio}}{\varepsilon_{\rm flare}}. \tag{2.10}$$

As already mentioned, the mechanism for emission of the coherent radio emission is the synchrotron maser mechanism, where bunches of electrons will simultaneously jump to the ground state, emitting photons of the same wavelength and start a chain of stimulated emission, amplifying the radiation and, therefore, creating a maser.

The ultra-relativistic shock heats the plasma to ultra-relativistic temperatures and the post-shock energy is shared roughly equally between the ions and electrons present in the plasma, heating each to a Maxwellian distribution of energies. Due to the strong magnetic fields associated with the process, the electrons radiate incoherent synchrotron emission in the hard X-ray/$\gamma-$ray range. Considering that the radiated photon energy is equal to that given to the

electrons, it follows that

$$E_{\mathrm{X}/\gamma} \approx \frac{\varepsilon_{\mathrm{flare}}}{2}. \tag{2.11}$$

Applying this model to FRB200428 gives an approximate radiative efficiency of $\eta \sim 10^{-4} - 10^{-5}$, which is in agreement to the measured ratio of the radio and X-ray fluence, $\varepsilon_{\mathrm{radio}} \sim 10^{34} - 10^{35}$ erg [53] and $E_{\mathrm{X}/\gamma} \sim 10^{39} - 10^{40}$ erg [79].

The other half of the shock energy thermally heats the ions present in the external medium surrounding the magnetar. In the co-moving frame of the shock gas, the ions will possess a relativistic Maxwellian energy distribution with an average particle energy of

$$\bar{E} \approx \frac{\Gamma m_p c^2}{2} \tag{2.12}$$

where Γ is the Lorentz factor of the forward shock.

A small fraction of the ions is accelerated to higher energies via diffusive acceleration [80], into a power-law non-thermal spectrum. This process will have associated a maximum cut-off energy estimated through the proton acceleration time to various loss time scales. The most constraining is not the proton synchrotron cooling, which happens over longer timescales, but equating the acceleration time to the dynamical time over which adiabatic losses occur, i.e., interactions between the ions and the photons of the medium.

Due to their large mass, the ions will hold on to their energy for long enough time to interact with the thermal synchrotron photons via the photo-meson process

$$p + \gamma \rightarrow p + \pi^{\pm,0}.$$

The rate of the hadro-nuclear interactions is low in comparison because of the high photon-to-baryon ratio behind the shock.

The high-energy neutrinos and γ-rays will be produced after the decay of $\pi^{\pm}$ and π^0, respectively. At earlier times ($t \sim t_{\mathrm{FRB}}$), most of the pion-production will be by the thermal protons interacting with the synchrotron photons. At times $t \gg t_{\mathrm{FRB}}$, only the non-thermal protons will have enough energy to produce pions, see Fig. 2.12.

For the earlier emission, it is estimated that $\sim 1 - 10$ TeV neutrinos are generated by the interaction of the thermal protons with synchrotron photons and for the latter emission, it is estimated the production of neutrinos with peak energy of $\sim 1 - 10$ PeV . On the left side of Fig. 2.13 we show an example calculation of the observed neutrino spectrum for a fiducial model with $t_{\mathrm{FRB}} = 1$ ms, $\nu = 1$ GHz, $\varepsilon_{\mathrm{radio}} = 10^{40}$ erg [59].

Figure 2.14 presents some key properties regarding this predicted neutrino emission such as the duration, spectral peak, total radiated energy, and fluence for a sample of FRBs with measured properties and known distances. Considering the FRB200428 from the galactic magnetar SGR 1935+2154, with $\varepsilon_{\mathrm{flare}} \sim E_{\mathrm{X}/\gamma} \sim 10^{40}$erg, the model predicts a neutrino burst

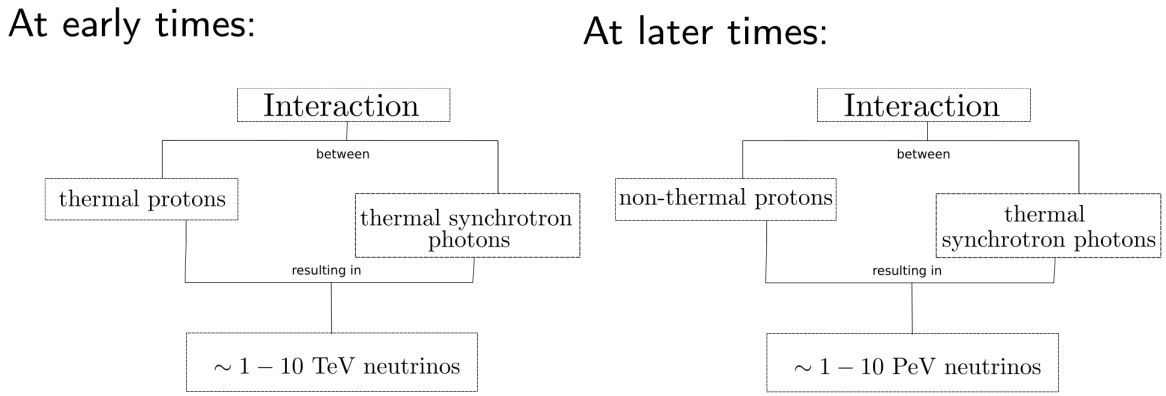


Figure 2.12: Baryon loaded shock scenario. At earlier times ($t \sim t_{\rm FRB}$) most of the pion-production will be by the thermal protons interacting with the synchrotron photons. At later times, $t \gg t_{\rm FRB}$, the particles interacting with the synchrotron photons will be the non-thermal protons.

of energy $\varepsilon_\nu \lesssim 10^{32}$ erg, corresponding to a fluence of $F_\nu \sim 10^{-12}$GeV cm^{-2}, which is ∼11 orders of magnitude smaller than the IceCube upper limit of 5×10^{-2}GeV cm^{-2} [59]. Hence, the non-detection of a neutrino associated with FRB 200428 is not constraining on the baryon loaded shock model.

In Fig. 2.13, however, we can see that it is the possible to have an observed neutrino fluence within the Icecube sensitivity. So, for what conditions does this happen? First, the distance of the source has to be quite small, definitely a galactic FRB. In the case of Fig. 2.13 (left) the source distance is 0.1 kpc. Second, if the galactic magnetar flare is more energetic, at the energy scale of the gamma-ray emission from giant flares, $\varepsilon_{\rm flare} \sim 10^{46}$erg and if we consider it is coming from the closest detected magnetar, 1E 1048.1-5937 at ≈ 2.7 kpc, then the predicted fluence could reach $\sim 10^{-2}$ GeV cm^{-2}. Detecting neutrinos associated with individual extragalactic FRBs discovered to date is unlikely due to their much greater distances, see the last panel of Fig. 2.14.

This model also predicts a burst of ∼TeV-PeV gamma-rays from the neutral pion decay, as shown in the graph on the right of Fig. 2.13. In this case, the thermal photons fall in the sensitivity range of the ground-based HAWC observatory [81]. Nonetheless, this is only possible for nearby sources $\lesssim 0.1$ kpc.

2.5 High-energy multimessenger studies with FRBs

Regarding GRBs, there have been several attempts at connecting them with FRBs. Either through a targeted/blind search for repeating fast radio bursts associated with gamma-ray bursts [82, 83, 84] or through a targeted/blind search for gamma-ray counterparts of fast radio bursts [85, 86]. Recently, the detection of a GRB, at GeV energies, from a magnetar giant

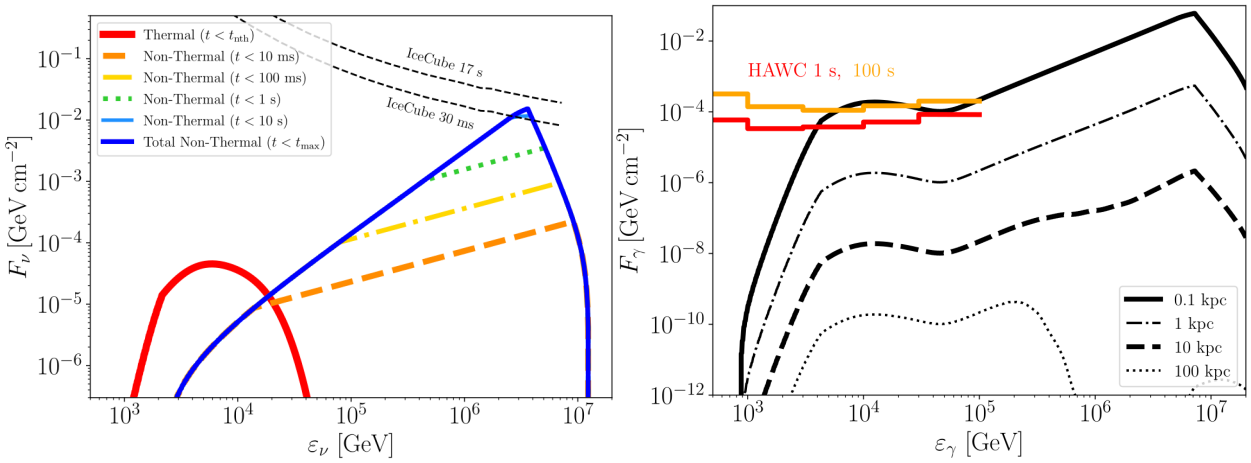


Figure 2.13: Left: Observed neutrino spectra expected using the baryon load shock model for a fiducial burst of 1ms duration, $\nu = 1$ GHz and $\varepsilon_{\rm radio} = 10^{40}$ erg and distance of 0.1 kpc. Shown for comparison are also approximate IceCube sensitivity curves for observation windows of 30 ms and 17 s [59]. Right: Total γ-ray fluence due to neutral pion decay from the same fiducial burst now for a source at a distance of 0.1, 1, 10 and 100 kpc, compared to the sensitivities of the HAWC Observatory at 0° zenith angle [59].

flare in the Sculptor galaxy (z=0.0337) has motivated the search for gamma-ray counterparts of FRBs, as an FRB has been already associated with a galactic magnetar. Studies have also been conducted to associate X-ray emission to FRBs, resulting in upper limits on the hard X-ray flux [87]. Multi-wavelength observations have been conducted for different FRBs. As already discussed, however, it only resulted in confirmed counterparts in a few cases.

Some theoretical models predicted that a small fraction of FRBs may be associated with gravitational waves. There arenot yet multimessenger studies of FRBs and gravitational waves. However, such association can be very valuable, as gravitational-wave measurements can be used to severely constrain the validity of FRB binary of neutron stars and/or black holes coalescence models [88]. Additionally, GW/FRB association systems could be used as complementary cosmic probes [89].

Neutrino associations have been explored by both Antares and IceCube. Antares' search found no coincident neutrino candidate and, consequently, constraints on the neutrino fluence and on the energy released were imposed [90]. IceCube's search for coincidence between neutrinos and fast radio bursts did not result in any candidate as well and upper limits on neutrino fluence were set [91, 92]. One important thing to note is that all of these three searches were performed when the number of detected FRBs were of only a dozens events. Thus, there will probably be more searches in the near future. Another aspect to note is that there is not yet a published high energy gamma-ray multimessenger search for FRBs, either using HAWC or LHAASO.

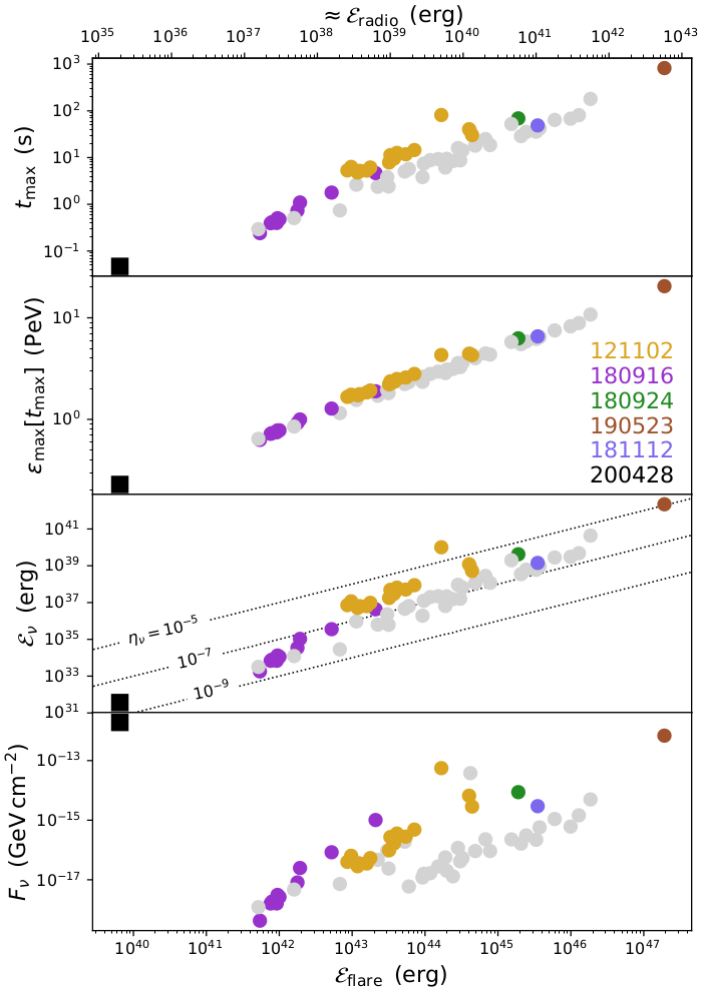


Figure 2.14: Baryon loaded shock scenario. Predicted neutrino properties for a sample of FRBs with measured properties as a function of the total flare energy (bottom axis) or approximate radio isotropic energy (top axis). The neutrino properties shown are $t_{\rm max}$, the duration of neutrino emission, $\varepsilon_{\rm max}\,[t_{\rm max}]$, peak neutrino energy, ε_ν, total neutrino energy radiated and F_ν, observed neutrino fluence. The FRBs shown include the sample of localized FRBs with known distances including two repeaters (different colors) and non-localized CHIME FRBs (gray points) [59].

3 High energy astroparticles and their detection

Even without theoretical models predicting high energy counterpart emissions it makes sense to perform general studies searching for counterparts whenever we have emissions involving high energy densities at the source as they make the typical multimessenger study case. In this work, we explore the possibility of detecting FRB counterparts and which detectors may be more appropriate to do so. We begin by delving into the typical high energy multimessenger signals and their detection.

3.1 High energy astroparticle detectors

The type of detector used to observe high energy particles depends on the particle in question and its energy [94]. There are four main types of high energy multimessenger signals: electromagnetic radiation (EM); high energy neutrinos (HEN); ultrahigh energy cosmic rays (UHECR); gravitational waves (GW). In table 3.1, we can see an overview on the main detectors, current, in construction and proposed.

Regarding photons, for x-rays and lower energy gamma-rays, the detection can be made by satellite, where the primary is directly detected. The satellite detectors have a small effective area, of the order of 1 m^2, a large duty cycle and a low rate of background events considering that they can be coupled to anti-coincidence systems that reject cosmic rays [94]. Examples of currently employed satellites include AGILE [95] and the largest gamma-ray space-based detector, the Fermi observatory [96].

If, however, the energy of the particle is high enough, some of the resulting secondary particles of the extensive air shower array (EAS) - created by the interaction of the particle at the top of the atmosphere - can reach ground-based detectors. Additionally, satellites are limited in the their surface and calorimeter capacity and as so, for higher energies, it is more convenient to study the effects of the interaction of the high energy photon with the atmosphere. There are two main types of ground-based detectors of very high energy (VHE) gamma rays - the Cherenkov telescopes and the EAS arrays, see Fig. 3.1. Cherenkov telescopes like H.E.S.S. [98], MAGIC [99] and VERITAS [100], detect the Cherenkov photons produced in the atmosphere by charged particles in the showers. These detectors are characterized by a low duty-cycle since, due to the faintness of the signal, data can typically only be taken on

	EM	HEN	UHECR	GW
Current	Swift satellite: BAT 15-150keV; XRT 0.2-10keV; UVOT 170-560nm Fermi satellite: LAT 20 MeV-300 GeV; GBM,10keV-25MeV HAWC (North -ground air shower array): 0.3 -100 TeV MAGIC, HESS, VERITAS ground IACTs: 150 GeV- 30 TeV ZTF, ASAS-SN ground surveys, optical, near-IR LOFAR : ground array transient survey, radio	ICECUBE ice Cherenkov array: Gton array TeV-100 PeV, Deep Core 10- 300 GeV ANTARES water Cherenkov array: 50 Mton, TeV-10 PeV, Super-K water Cherenkov array: 50 kton, 4.5MeV- 1 TeV ANITA balloon radio array: 10^{17} - 10^{20} eV	AUGER extensive air shower array: 3,000 km^2 ,1600 tanks, 27 air fluor. tel., 10^{17}-10^{21}eV TA extensive air shower array: 760 km^2 surface tanks + air fluor. tel., 10^{17}-10^{21}eV	LIGO, 2x4 km GW ground interferometer: ~10-10^3 Hz. (~1-100 M_{sun} equal mass binaries) VIRGO 2x3 km GW ground interferometer: ~10-10^3 Hz. (~1-100 M_{sun} equal mass binaries) Pulsar Timing Array radio interferometer, NANOGrav: (10^5-10^7 M_{sun} equal mass binaries)
In construction	SVOM satellite (~2021): GRM 30keV-5MeV,ECLAIRS 4-250keV, VT 400-950nm GLOWBUG, space-ISS (~2023): Scintillator array, 30keV-5MeV. Einstein Probe satellite (late 2022) Large FoV, 0.5-5 keV Time-Domain Explorer GECAM satellite (mid-2020s) All-sky, 6 keV-5 MeV, GW counterpart eROSITA, satellite (~2020): All-sky transient survey, 0.3-10 keV . LHAASO ground air shower array (~2022) 100GeV– 1 PeV LSST ground survey (~2022) optical, near-IR SKA ground array survey (~2022) Radio interferometer CTA ground IACT arrays, (~2025?): 4 LST 20-150GeV, 40 MST 0.15-5TeV, 70 SST 5-300TeV	ICECUBE upgrade (~2021): PINGU 7 new strings, 5-20 GeV KM3NeT water Cherenkov array (~2024?) 4-5 Gton TeV-10 PeV, ORCA 1-20GeV, ARCA 0.1TeV-100PeV Baikal GVD water Cherenkov array (~>2024?) 2 Gton , 5 TeV-10 PeV, Hyper-K water Cherenkov array (~>2026) 1 Mton, 1 MeV- 1 TeV	AUGER, Prime: Add 1600 surface scintillators, 10^{17}-10^{21} eV LHAASO ground air shower array (~>2023?) 100GeV– 1 PeV TAx4 (4 times previous area, ~>2023?): ~3,000 km^2 , 10^{17}-10^{21} eV	LIGO, A+ upgrade (2023): (increase previous detection distance by x2) KAGRA 2x3 km GW underground interf. (~2022): ~10-10^3 Hz. (~1-100 M_{sun} equal mass binaries) LIGO-India 2x4 km GW ground interf.(~2024): ~10-10^3 Hz. (~1-100 M_{sun} equal mass binaries) Pulsar Timing Array radio interf. (>2020), PPTA, EPTA: (10^5-10^7 M_{sun} equal mass binaries) eLISA, 3x2.5x10^6 km (~>2030s) GW space interferometer: ~10^{-4}–10^{-1} Hz. (~10^5-10^7 M_{sun} equal mass binaries)
Proposed	ISS-TAO, space-SS (~2023?): GTM 10keV-1 MeV, ULTRASAT satellite (~2023?): 50cm UV telescope, 250-280nm AMEGO satellite (~>2030s?): 300 keV-10 GeV HAWC-Southern hemisphere (~>2030s?): 4xNorth size, higher altitude, 0.1-100 TeV TMT, ELT, GMT (~>2025-30) 30 m class O/IR ground-based telescopes	ICECUBE Gen-2 (~>2030s?): PINGU 1-20 GeV, High Energy extension <100 PeV ARIANNA ice radio array (~>2025-30s?): 10^{17} - 10^{20} eV ARA/RNO ice radio array (~>2025-30s?): 10^{17} - 10^{20} eV GRAND ground det. array (~>2030s?): 10^{17} - 10^{21} eV	K-EUSO, space-ISS (~>2023-25?): UV tel. det. of exensive air showers 10^{17} - 10^{21} eV POEMMA satellite array (~>2030s?): UV telescope det., 10^{17} - 10^{20} eV GRAND ground det. array (~>2030s?): 10^{17} - 10^{21} eV TRINITY ground radio array (~>2030s?): UV telescope det., $10^{16.5}$ - 10^{18} eV	LIGO Voyager upgrade (~>mid-2020s) (BNS range up to 700-1,000 Mpc) Cosmic Explorer, 2x40 km (~>2030s) GW ground interferometer: ~10-10^3 Hz. (~1-100 M_{sun} equal mass binaries) Einstein Telescope, 3x10 km (~>2030s) GW underground interferometer: ~10-10^3 Hz. (~1-100 M_{sun} equal mass binaries)

Table 3.1: Multimessenger detectors, separated between the four principle signals for multimessenger detection: electromagnetic radiation (EM); high energy neutrinos (HEN); ultrahigh energy cosmic rays (UHECR); gravitational waves (GW). They are further separated into current, in construction and proposed detectors, which may not be completely up to date (reference from 2019)[93].

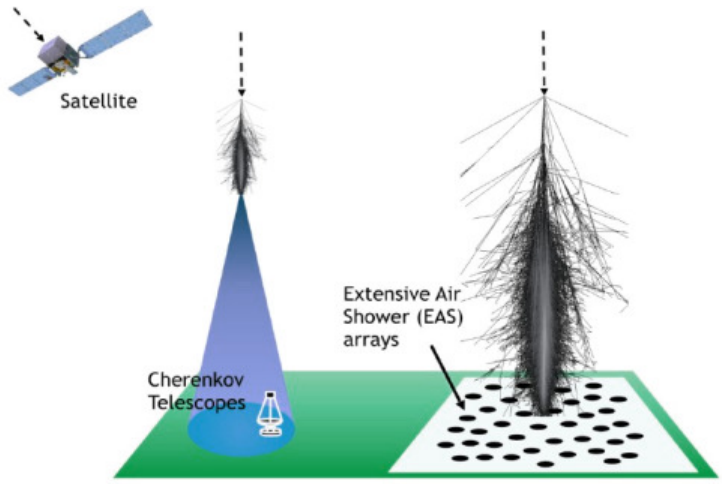


Figure 3.1: The three types of high energy photon detectors - Satellites, Cherenkov telescopes and EAS arrays [97].

moonless cloudless nights. These telescopes, operating for photons starting at ∼GeV energies, study showers where the energy of the primary is not enough for the secondary particles to be detected at ground level, but big enough for the Cherenkov light produced to be detected by ground-based telescopes. Thus, in order to improve the strength of the signal detected, Cherenkov telescopes are placed at mountain-top altitudes.

The EAS array detectors, like HAWC [101] or LHAASO [102], are large arrays of detectors sensitive to secondary particles generated in the extensive atmospheric showers. These arrays have a large duty-cycle and large field of view. The idea is to detect the secondary particles arriving at the array of ground-based detectors. The Large High Altitude Air Shower Observatory (LHAASO) is a gamma-ray and cosmic-ray observatory in Daocheng, China [102]. It consists of a hybrid extensive air shower array with an area of about $1\,\mathrm{km}^2$ at an altitude of 4,410 m a.s.l.. The Southern Wide-Field Gamma-Ray Observatory (SWGO) is a proposed ground array detector for very high energy gamma-ray astronomy to be constructed in the Southern Hemisphere [103].

Through the strength of the signal and its time of arrival to each detector, the properties of the shower and therefore of the primary are estimated, similarly to the Pierre Auger observatory surface array described in section 3.3. Such high energy photons are expected to be quite rare, it is only possible to detect them with very large surface arrays because they interact with the atmosphere creating the extensive air showers and consequently secondary particles.

Very high energy neutrinos are interesting particles as they can travel long distances without being absorbed, contrarily to photons, and without being disturbed by the magnetic deflection as experienced by charged particles. For these reasons, very high energy neutrinos also require very particular detectors or conditions of detection. Two current VHE neutrino detectors are

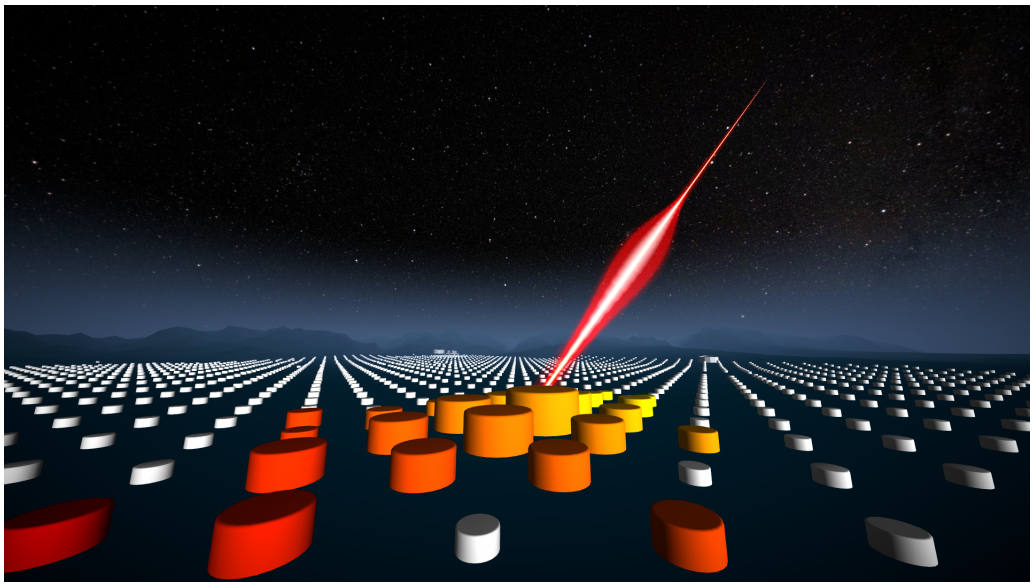


Figure 3.2: Representative image of an extensive air shower (EAS) producing signal in the surface array of the Pierre Auger Observatory. Credit: LIP

Antares [104] and IceCube[105]. IceCube is a 1 km^3 experiment found in Antartica that has been in operation since 2010. The detector is made up of 80 sparse and 6 dense vertical strings, each holding 60 optical modules at a depth of 1450-2450 m under ice. A single module contains several photomultiplier tubes. Additionally, IceCube counts with an air-shower array, similar to the previously mentioned EAS arrays. Antares is a quite similar detector to Icecube, with 12 vertical strings, making it a total of 1000 optical modules. Though, instead of being under ice it is found underwater, in the Mediterranean sea.

3.2 Extensive atmospheric showers

To test the baryon loaded shock model and therefore try to find out if FRBs can be associated with high energy photons and neutrinos, we need to first understand how these particles interact and how they are detected. Such high energy particles will interact in the atmosphere creating a chain of interactions that result in the production of an extensive air shower (EAS) of particles, see Fig. 3.2. We will describe the phenomena of extensive atmospheric showers through a simple model, Heitler's model [106].

3.2.1 The Heitler model for electromagnetic showers

The traveling particle that first interacts in the atmosphere, in this case a photon, is called the primary particle of the air shower and the particles created as a result of the chain interactions are the shower secondary particles. The Heitler model can be used to describe

the behavior of an EAS when the primary is a cosmic ray, i.e. atomic nuclei that can be as simple as a single proton or as heavy as iron. In this case the EAS will be a combination of electromagnetic and hadronic cascades. If the primary is a photon, however, the shower will only have an electromagnetic component [106].

According to the model, the electromagnetic cascade is made up by consecutive cycles of pair production followed by one-photon bremsstrahlung emission, Fig. 3.3. Therefore, for electromagnetic showers, a electron/positron ($e^{\pm}$) radiates a photon (γ) after traveling a distance (d),

$$d = \lambda_r \ln(2), \tag{3.1}$$

losing half its energy and where, λ_r, is the radiation length in the medium. The photon, after traveling the same distance, produces a pair e^{+}+e^{-}, of equal energy. Thus, the energy is equally distributed between the two leptons. After n splittings, the total length of the shower (X) is

$$X = n\lambda_r \ln(2) \tag{3.2}$$

and the total number of particles in the shower,

$$N = 2^n = e^{\frac{X}{\lambda_r}}. \tag{3.3}$$

The process ends when the individual energies of the leptons, $e^{\pm}$, get smaller than the critical energy (ξ_c^e) required for pair production or the bremsstrahlung, below which radiative energy loss becomes less than collisional energy loss. In air, $\xi_c^e = 85\text{MeV}$.

Lets consider that the air shower is initiated by a single photon (γ). The energy of the shower or equivalently the energy of the primary ($E_\circ$) can be written as a function of the maximum number of shower particles ($N_{\max}$) and the critical energy,

$$E_\circ = \xi_c^e N_{\max}. \tag{3.4}$$

We can obtain the penetration depth $X_{\max}^{\gamma}$ at which the shower reaches maximum size by estimating the number of n_c of splitting lengths required for the energy per particle to be reduced to ξ_c^e. Remembering that $N_{\max} = 2^{n_c}$ and using eq. 3.4 one obtains,

$$n_c = \ln\left[E_\circ/\xi_c^e\right] / \ln 2, \tag{3.5}$$

resulting in,

$$X_{\max}^{\gamma} = \lambda_r \ln\left[E_\circ/\xi_c^e\right]. \tag{3.6}$$

Even though this model is able to explain the main components and relations within a shower using very simple considerations, it is not without faults. It overestimates the ratio

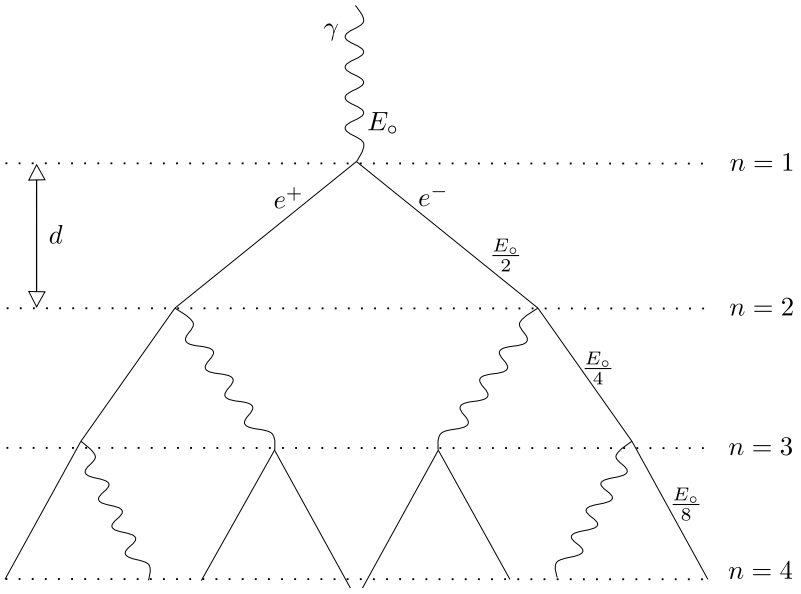


Figure 3.3: Schematic view of an electromagnetic cascade. Adapted from [106] and [107].

of electrons to photons, as it predicts, after a few generations, that $N_e \approx \frac{2}{3} N_{\max}$ whereas in reality the relative number of electrons is not as big. This discrepancy is due to several things, manly because multiple photons are often radiated during bremsstrahlung and also because many $e^{\pm}$ range out in the air. Actually, many aspects of the development of the shower after reaching its maximum are beyond the scope of this model, as the attenuation of particles is not accounted for.

There are two important aspects regarding EASs that Heitler's model explains well and that are relevant to retain, that the maximum size of the shower is proportional to $E_\circ$, see eq. 3.4 and that the depth maximum increases logarithmically with energy, see eq. 3.6.

Heitler's model is also implemented to explain extensive air showers with cosmic rays as primaries. In this case, the nuclei interact hadronically in the atmosphere, producing neutral and charged pions. The neutral pions decay almost immediately to photons, initiating electromagnetic showers. Charged pions, $\pi^{\pm}$, traverse one more layer before interacting. The process continues until the individual energy of the charged pions falls bellow the critical value, ξ_c^{π}, where they then are all assumed to decay, yielding muons and neutrinos.

3.3 The Pierre Auger Observatory

The Pierre Auger Observatory was created with the intent to perform a high statistics study of cosmic rays, at the highest energies ($\gtrsim 10^{18}$eV) by detecting the secondary particles of the EAS. For this reason alone, the observatory does not seem the most obvious choice for detecting the emissions that the baryon loaded shock scenario predicts which consist on

high energy photons and neutrinos in the energy range of $\sim$ TeV$-$PeV. However, it is possible to detect neutrino and photon air showers with the Pierre Auger observatory as searches for photons at the higher energies, above 10^{18} eV, have already been performed [108]. Additionally, regarding the energy of the shower, since the completion of the observatory changes have been made for the detection of particle showers of lower energy $\gtrsim 10^{16}$eV, which would explore the non-thermal peak of the distributions predicted by the model.

If we are focusing our analysis in the Pierre Auger observatory and the theoretical model being followed also predicts the emission of cosmic rays one could wonder why we chose to study the emission of high energy photons/neutrinos and not high energy cosmic rays. Cosmic rays are not ideal for a coincidence multimessenger analysis because they do not preserve their direction of emission upon arrival to the atmosphere as they are heavy charged particles and are considerably deflected by magnetic fields during the journey. Therefore, the possibility of spatial and temporal coincidence with other multimessenger signals is lost.

3.3.1 General description of the observatory

The Observatory works as a hybrid detector, with the combination of a large surface detector (SD) and a fluorescence detector (FD). The SD is compounded of a baseline array, containing 1660 water-Cherenkov tank stations placed in a triangular grid with the nearest neighbors separated by 1500 m, and a smaller array, the infill, where stations are separated by 750 m [109], note the red dots in Fig. 3.4. The array is spread out over an area of $\sim$ 3000 km^2. The detector is allocated at a mean altitude of $\sim$ 1400 m and is located between latitudes 35.0° and 35.3°S and between longitudes 69.0° and 69.4°W.

The surface array operates with a 100% duty cycle, a well-defined aperture independent of energy above $10^{18.5}$eV, measurement of the time structure of signals from the shower particles and sensitivity to showers arriving at large zenith angles. Hence, the SD has the capability of operating continuously, measuring the particle densities as the shower strikes the ground just after the shower maximum. On the left side of Fig. 3.5 there is a photograph of one of the tanks.

Contrary to the SD, the fluorescence telescopes only record air shower development in the atmosphere above the surface array on dark moonless nights, which represents a duty cycle of $\sim$ 15%. There are four air fluorescence sites – Los Leones, Los Morados, Loma Amarilla and Coihueco, on the left side of Fig. 3.6 is a photograph of one of them, the Los Leones fluorescence detector enclosure. The FD, on dark nights, records the amount of nitrogen fluorescence produced by showers along its path. The idea is, considering that the intensity of fluorescence light is proportional to the energy dissipated in the shower, the integration of the intensity of light produced along the shower axis results in a nearly calorimetric measurement of the shower energy. The fluorescence detector always operates in conjunction with the surface detector.

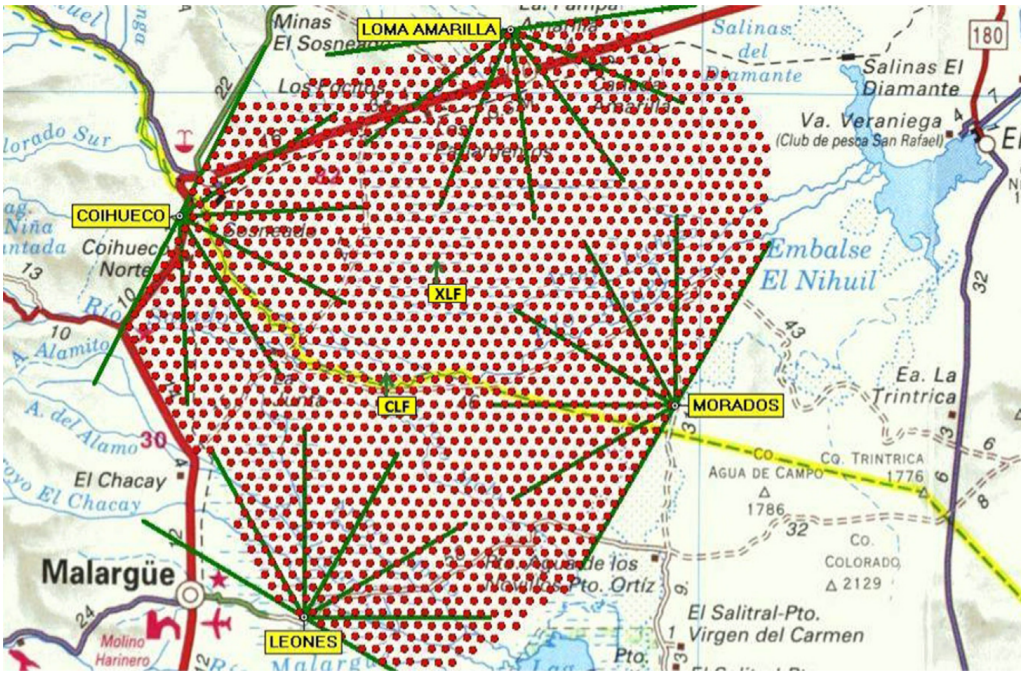


Figure 3.4: Map of the Pierre Auger Observatory. The red region represents the surface array (SD), with each dot corresponding to one of the 1660 surface detector stations. The four fluorescence detector enclosures are shown, each with the 30° field of view of its six telescopes. Also indicated are the two laser facilities, CLF and XLF, near the center of the observatory [109].

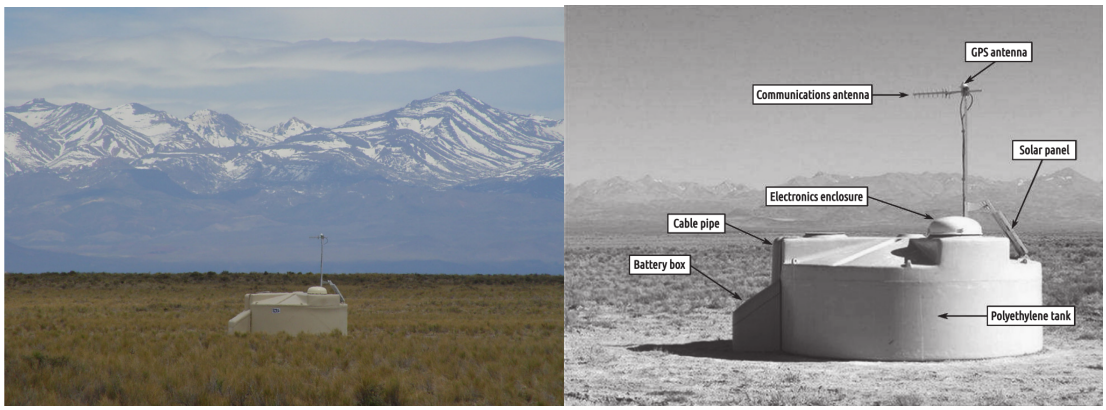


Figure 3.5: Surface detector station or Cherenkov water tank. Left: Photograph of one of the stations. Right: Description of the main components of the tank [109].

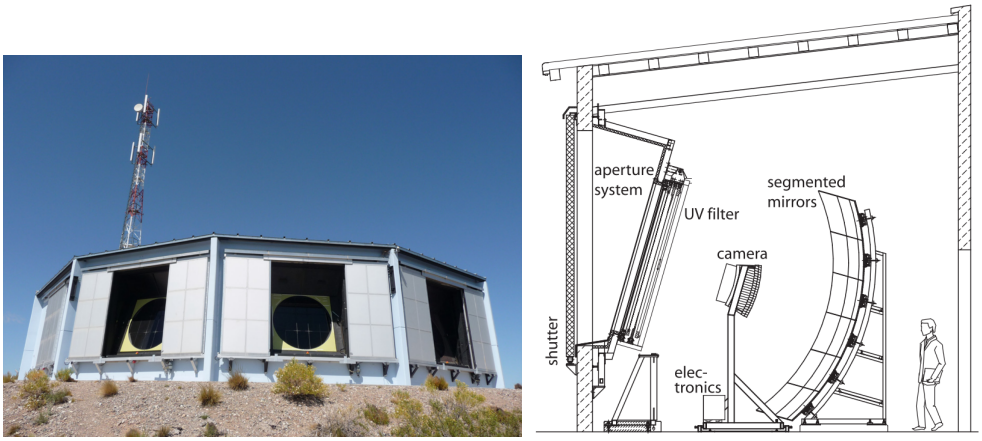


Figure 3.6: Left: The Los Leones fluorescence detector enclosure. Right: Schematic view of a fluorescence telescope and description of its main components [109].

Because of the complementarity of this hybrid setup, the energy calibration achieved by the FD can be transferred to the surface array with its perfect duty cycle. Additionally, comparing the independent measurements of each detector permits to overcome some limitations of each individual detector and to perform important cross-checks. Therefore, the observatory possesses the capability of measuring air showers simultaneously by two different but complementary techniques [109]. Thence, using this hybrid detection system, the observatory takes advantage of both the FD and SD to measure the same properties of the primary, its energy, mass, and direction.

3.3.2 Surface detector

As has been said, the observation of air showers is accomplished by observing the secondary particles. In the case of the surface array, it is sensible to the ground level slice of the air shower, with sensitive water Cherenkov stations which respond to both the muonic and electromagnetic components of the showers. The duty cycle of the detector means that the observatory has uniform coverage in right ascension.

A surface detector station consists of a water tank of 3.6 m of diameter and 1.2 m height with an isolating and reflective internal layer. The tanks interior is filled with 12 000 l of ultra-pure water and 3 photomultiplier tubes (PMTs) distributed symmetrically on the tank's surface. The PMTs detect the Cherenkov light produced by relativistic charged particles passing through the tank. However, the tanks are also sensitive to the passage of photons because of pair-production in the water. So that they work autonomously, the tanks have installed a solar powered system for the PMTs and the electronic components of the tank. The various components of the tank, including the aforementioned solar powered system can be seen in the image on the right of Fig. 3.5.

After arriving to the photomultiplier tubes, the Cherenkov photons provoke photoelectric effect in the photocathode, resulting in the emission of electrons. These electrons then enter in a multiplier chain, made up by a succession of dynodes each at an higher potential than the previous, so the electrical signal produced is detectable. In the multiplier chain the electrons are accelerated by an electric field until they reach the first dynode, after which several lower energy electrons are emitted, the process is then repeated various times ensuring that a number increasingly bigger of electrons is being emitted. At the end of the chain the electrons find the anode, where the accumulation of charge results in a measurable pulse of current. The simultaneous signal coming from several adjacent tanks in specific conditions will trigger an event detection, the amount and time arrival of signal to each tank will determine the estimated properties of the shower. The event reconstruction will be discussed in more detail in the subsection 3.3.5.

3.3.3 Fluorescence detector

There are four separate sites that make up the FD, distributed around the surface array, which can be seen in Fig. 3.4. Each site contains 6 telescopes in a clean climate controlled building. A single telescope has a field of view of $30° \times 30°$ in azimuth and elevation, the 6 telescopes possess a combined $180°$ coverage in azimuth.

A schematic view of a fluorescence telescope can been seen in Fig. 3.6. The nitrogen fluorescence light enters through a circle diaphragm of 11 m radius covered by a UV filter glass window that reduces the background light flux. The light is then focused by a spherical mirror of ~ 3400 mm radius of curvature onto a spherical focal surface, the camera of the telescope. The camera has an outer radius of curvature of 1701 mm and an inner curvature radius of 1641 mm. A matrix of 22 rows by columns of pixels, each with an hexagonal photomultiplier tube positioned inside a 400 mm diameter hole, constitutes the camera.

The fluorescence detector measures the longitudinal profile of the extensive air shower recorded by the SD whenever it is dark enough for the atmospheric fluorescence measurements to be reliable. The integral of the longitudinal profile is used to determine the shower energy, the rate of shower development and the depth at which a shower reaches its maximum $X_{\max}$, indicative of the primary particle's mass. The ultraviolet fluorescence light is emitted isotopically predominantly by the electromagnetic component of the shower.

3.3.4 Upgrades

The Pierre Auger Observatory has, since the completion of the baseline construction, gone through new enhancements, in order to extend its scientific capabilities. These enhancements include the high elevation Auger telescope (HEAT), identical to the fluorescence telescopes but that can be tilted by $29°$ upward with the main objective of lowering the energy threshold

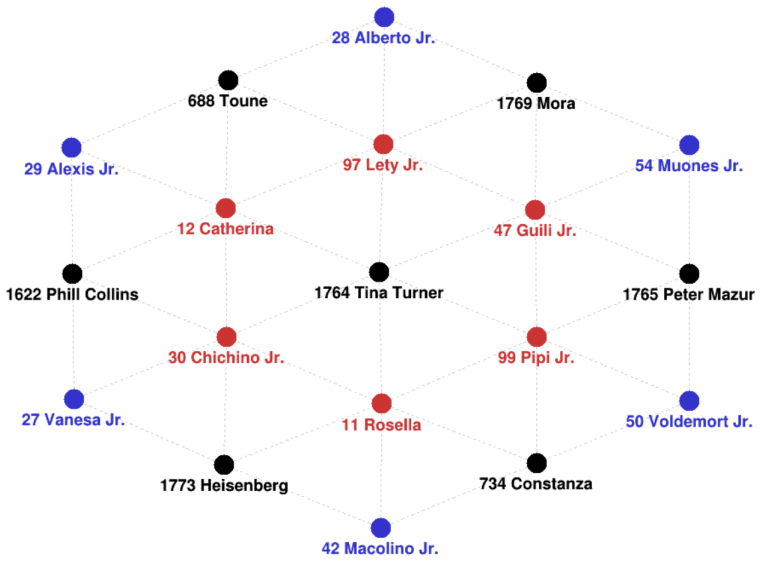


Figure 3.7: Schematic map of the SD-433 array. The color represents to which matrix the water Cherenkov detector belongs. The red tanks are part of the SD-433 unitary cell, black belong to the SD-750 array and blue to the SD-433 upgrade [110].

of hybrid data. Another upgrade is the Auger muon and infilled ground array (AMIGA), designed with the intent to directly measure the muon content of air showers. It achieves this objective with a joint system of water Cherenkov and buried scintillator detectors inside of the denser matrix of the SD, with 750 m spacing. Auger Prime is the main update made to the observatory and it consists in the implementation of scintillators above the water tanks allowing for the separation of the electromagnetic and muonic components of a shower.

The last upgrade to be mentioned will be important for our analysis, and is an even denser array created inside of the 750 m matrix, the SD-433 [109].

3.3.4.1 SD-433

The SD-433 was made for further lowering the energy threshold of the observatory. Its creation started in 2011 with the deployment of six water Cherenkov detectors placed at 433 m around the central station, forming an hexagon, which constitutes the elementary cell of the SD-433. This first cell has been operational since May of 2013 and is represented in Fig. 3.7 by the red dots. The array already suffered two upgrades to reach a 7-hexagon aperture and a total of 19 tanks. The complete matrix has been operational since May of 2019. The denser array was successful in lowering the energy threshold to 10^{16} eV even though without a full efficiency, specially for larger zenith angles. The trigger efficiency of the array will be discussed in more detail in subsection 4.1.1.6.

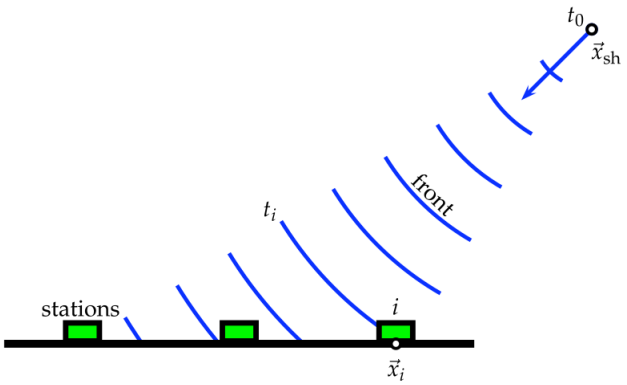


Figure 3.8: Event reconstruction with the surface array. Scheme representation of the evolution of the shower front [109].

3.3.5 Event reconstruction

In this work we will be focusing on the lower energies of Auger's capability, $\sim 10^{16}$ eV and for these energies the event reconstruction is based only on the ground array. Thus, we will focus on the event reconstruction of the surface array.

The sizes and times of signals registered by each individual SD station allow for the reconstruction of the geometry of the air shower, namely the shower core, i.e. the point of intersection between the shower axis with ground, and the arrival direction of the primary. Moreover, the shower size and energy are also reconstructed. For an event to be reconstructed it has first to pass a set of requirements of its quality for physics analyses, called off-line triggers. These triggers ensure that the shower geometry can be can reconstructed and if the signal detected is indeed an EAS. They contemplate a selection on events which triggered several adjacent surface stations within the propagation time of the shower front. Another cut selects events which are well contained inside the surface matrix, demanding that the station with the highest signal is surrounded by 6 operational stations, to ensure that a geometrical localization of the detected signal allows for the reconstruction of the event.

In order to obtain an approximation of the direction of the shower, an adjustment is made of the times of arrival of the signal to each individual tank to a wavefront. A good approximation of the shower particles front is a spherical wavefront traveling at the speed of light. A schematic representation of this concept can be found in Fig. 3.8. From the application of this model, the estimated instant for the shower center to hit the ground is inferred and, along it, the curvature radius of the spherical wave can be found.

The lateral profile of the shower, via the adjustment of the lateral distribution function (LDF), is also reconstructed, which represents the dependency of the signal as a function of the orthogonal distance to the shower axis and is described by the Nishimura-Kamata-Greisen (NKG) function [111]. In this characterization, each individual station is put in one of the three

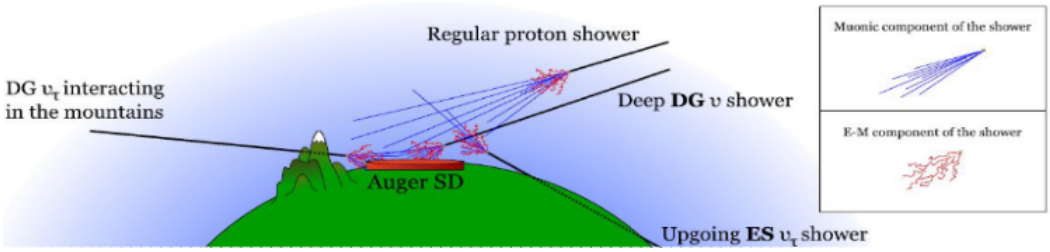


Figure 3.9: Types of neutrinos in Auger. Credit: Roger Clay, University of Adelaide.

following categories: saturated, which happens when the stations is too close to the shower center, non-triggering, for stations that are too far from the shower center, and candidates, for the stations which contribute to the shower reconstruction. For each event the amount of signal produced in each triggered tank as a function of the distance to the shower core is adjusted to the NKG function. From this function the amount of signal expected to a set distance (1000 m) is retrieved and then normalized for it to reproduce the amount of signal the shower would have produced at the set distance from its core if it had arrived at a set zentih angle ($\theta = 38°$). This value then directly correlates to the energy of the shower and is used to estimate it.

3.3.6 Photon detection

There are two main characteristics of a cosmic ray air shower that distinguishes it from a shower initiated by a photon.

The first difference is revealed in the shape of the LDF adjusted to the shower. Eletromagnetic showers do not possess the muonic component and as so the lateral profile of the shower will be different. Extensive air showers that possess a small muonic component on average have a steeper LDF compared to showers with a larger muonic component. [112].

There is another important characteristic of EAS that can be used to identify a photon as the primary which is the $X_{\max}$. Photon events are expected to have higher values of $X_{\max}$, meaning that the showers tend to develop deeper in the atmosphere which, for the same inclination, reflects onto a lower altitude for the maximum of particles in the shower to be achieved. Due to the absorption of the electromagnetic particles after $X_{\max}$ is reached, only vertical photon showers ($0° < \theta < 45°$), can be detected as secondary particles of events with higher inclinations will not reach the SD.

3.3.7 Neutrino detection

Extensive air showers initiated by neutrinos possess the two components of an EAS, the electromagnetic and the hadronic cascades. The neutrino will interact weakly with the hadrons

present in the atmosphere, resulting in the production of a jet of hadrons and in the production of a high energy lepton, corresponding to the flavor of the neutrino.

The hadron jet will start an EAS with the electromagnetic and hadronic components as described by the Heitler model. If the lepton produced is an electron, then it will initiate an electromagnetic cascade, if it is a tau it will eventually decay into a electron initiating an electromagnetic cascade as well and the last option is to produce a muon which will not form a EAS.

Therefore, an astrophysical high energy neutrino that interacts in the atmosphere will produce a extensive air shower with two components of secondary particles, electromagnetic and muonic. Neutrinos are very specific particles since they do not interact easily, that is why Antares and IceCube where designed using large volumes of water and ice, respectively. However, Auger detects the resulting particles in air showers and as so can only detect neutrino showers in specific conditions: down-going and earth-skimming. Neutrinos need to cross a big layer of the atmosphere to interact and be able to be detected by the surface array in Auger, in comparison with an EAS initiated by cosmic rays or photons for example. Therefore, only very inclined showers of high energy neutrinos, $60^\circ \lesssim \theta \lesssim 95^\circ$, can produce secondary particles detectable by the surface array. The down-going neutrino showers are the very inclined showers one would see in Auger, check Fig. 3.9. This class of neutrinos can be further divided into down-going low ($75^\circ < \theta < 90^\circ$), neutrinos down-going high ($60^\circ < \theta < 75^\circ$). The other class of neutrino showers in Auger is the earth-skimming neutrinos $90^\circ < \theta < 95^\circ$) where the primary passes through and interacts inside the earth before producing the EAS.

4 Multimessenger Study for FRBs

4.1 High-energy photons as FRB counterparts

Before trying to find high energy photons in coincidence with catalogued FRB events, it is helpful to study the sensitivity of the suitable detector(s), in order to evaluate if the detector is able to constrain the theoretical model in any way.

However, even before a sensitivity study, there are a few important quantities that must be estimated in the order to get as a first insight to what to expect. First, we can try to understand the number of photons that we expect to arrive at our detector for a source for which the energy and distance are known. To do so, we analyze the results of [59], the theoretical model already discussed in the Subsec. 2.4.4.1, where both the fast radio burst and photon/neutrino emission were assumed to be the result of an ultra-relativistic shock, propagating into a magnetized baryon-rich external medium in a magnetar.

We can look at the graphic on the right side of Fig. 2.13 in Subsec. 2.4.4.1 and approximate the expected number of 10^{16} eV photons for a source at a distance of $d = 10$ kpc:

$$F_\gamma \approx 10^{-7}\text{GeV/cm}^2 \tag{4.1}$$
$$\approx 10^{-14}\text{photons/cm}^2 \tag{4.2}$$
$$\approx 1 \text{ photon/ } (10000\text{km}^2). \tag{4.3}$$

The expected number of 10^{16} eV photons for a source at a distance of $d = 0.1$kpc is:

$$F_\gamma \approx 10^{-3}\text{GeV/cm}^2 \tag{4.4}$$
$$\approx 10^{-10}\text{photons/cm}^2 \tag{4.5}$$
$$\approx 1\text{photon/km}^2 \tag{4.6}$$
$$\approx 1 \text{ photon/ (area SD-433)}. \tag{4.7}$$

We can see these estimates as a function of the area of detection in Fig. 4.1 for the two distances to the source.

In [59], it is assumed that $\varepsilon_{\text{r,max}} \approx 10^{44}$ erg, for a frequency width $\nu \sim 1.4$ GHz and following the considerations of [113], we arrive at an estimated volumetric rate for FRBs of $\mathcal{R}(z = 0) \sim 6$ Gpc^{-3}yr^{-1}. The closest FRB of this energy per year, at this rate, occurs at

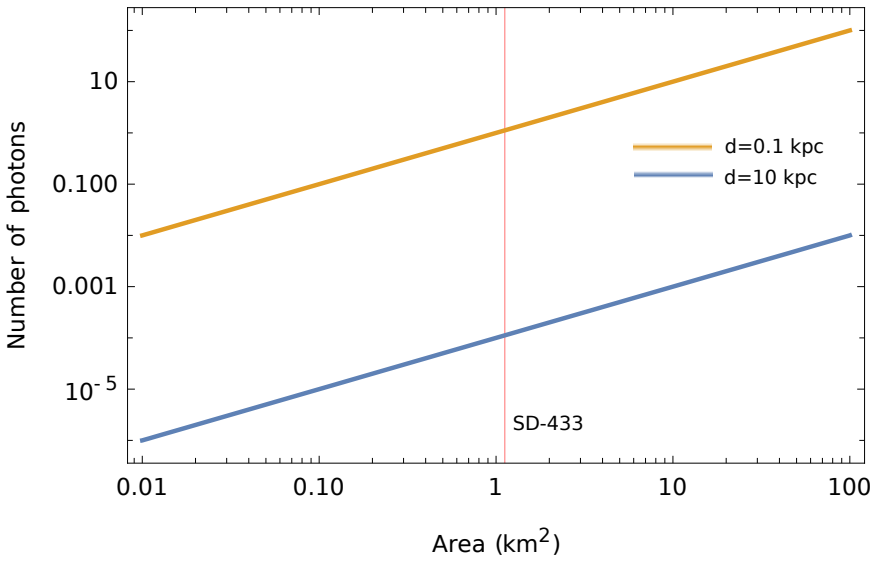


Figure 4.1: Estimated number of 10^{16} eV photons predicted by the baryon loaded shock scenario as a function of the area of detection. In blue, for a source at d=10 kpc and in yellow, for a source at d=0.1 kpc. The red line marks the effective area of the SD-433.

a distance $D_{\rm min} \sim 0.34$ Gpc. If we consider neutrino emission, for example, the expected neutrino flux would still be ~ 7 orders of magnitude below the IceCube detection threshold [59]. It is also suggested that a stack joint analysis for a large FRB sample could improve the sensitivity [114].

We can try to gauge how the volumetric rate changes when considering a lower energy for the burst. When we consider a lower energy for the FRB, the theoretical prediction for the expected fluence of the accompanying counterpart, a neutrino or photon, will be smaller. However, considering a lower energy for the burst will result in a smaller $D_{\rm min}$ and because of attenuation, when considering photon emission, the distance becomes quite important in determining the expected fluence, see Fig. 2.4.4.1. Thus, a lower energy FRB but at a closer distance can possibly be associated to a better overall fluence. Therefore, it may be relevant to estimate at which distance the closest FRB of a lower energy happens in a year.

For this effect, we will follow the considerations made at [113]. A full Bayesian analysis based on a Schechter rate function and on the ASKAP FRB statistic results in

$$\frac{d\mathcal{R}}{d\varepsilon} = \frac{\phi_0(1+z)^\beta}{\varepsilon_{\rm max}} \left(\frac{\varepsilon}{\varepsilon_{\rm max}}\right)^{-\gamma} e^{-\varepsilon/\varepsilon_{\rm max}}, \tag{4.8}$$

where ϕ_0 (in $\mathrm{Gpc}^{-3}\mathrm{yr}^{-1}$) is the volumetric rate normalization at redshift $z = 0$, β is defined so $(1+z)^\beta$ represents the evolution of the FRB rate with redshift, γ is the energy power-law index and $\varepsilon_{\rm max}$ is the maximum radio energy beyond which the rate cuts off exponentially. It

is found that the cumulative rate above a certain energy $\varepsilon \ll \varepsilon_{\rm max}$ at $z = 0$ is given by

$$\mathcal{R}(>\varepsilon) = \frac{\phi_0}{(\gamma - 1)} \left(\frac{\varepsilon}{\varepsilon_{\rm max}}\right)^{1-\gamma}, \tag{4.9}$$

with the constrain at a 68% confidence level ϕ_0 to $\log \phi_0 \simeq 1.1^{+0.8}_{-1.2}$ Gpc^{-3}yr^{-1}, $\gamma \simeq 1.6 \pm 0.3$, $\log \varepsilon_{\rm max} \simeq 34.1^{+1.1}_{-0.7}$. Considering that $\varepsilon \sim 10^{40}$ erg, $\mathcal{R}(>\varepsilon)$ becomes

$$\mathcal{R}(>\varepsilon) \sim 1860 \text{ Gpc}^{-3}\text{yr}^{-1}. \tag{4.10}$$

At this rate, the closest FRB of this energy per year occurs at a distance, $D_{\rm min}$, which obeys the following expression

$$\frac{V}{N} = \frac{1}{\mathcal{R}} = \frac{4\pi D^3_{\rm min}}{3}, \tag{4.11}$$

meaning that,

$$D_{\rm min} \sim 0.05 \text{ Gpc}. \tag{4.12}$$

Thus, thwwbe best chance to constrain theoretical emission models for counterparts of FRBs is to detect one FRB that is very bright and nearby. We can see the effect of the distance to the source on the predicted photon fluence for the baryon loaded shock scenario in Fig. 2.13, which decreases with the square of the distance. Additionally, we can see that photon absorption for the highest energies affects considerably the predicted fluence for larger distances. Those predictions were made for a fiducial burst with radio energy $\varepsilon_{\rm radio} = 10^{40}$ erg. The closest FRB of at least this energy per year, at this rate, occurs at a distance given by eq. 4.12. This distance is still about five thousand times larger than the closest ever detected FRB.

The fact that there is already a FRB detection from a galactic source at d∼10 kpc indicates that the FRB rate for lower energies should be much higher than at the higher energies. Therefore, because we have not yet detected a FRB which could come close to replicate the spectral photon fluence predicted in Fig. 2.13, it does not mean that in the next few years such detection cannot be made, as FRB statistics keep increasing at a rapid pace.

4.1.1 Sensitivity studies with the Pierre Auger Observatory

We now estimate the sensitivity of the Pierre Auger Observatory to high energy photons. When searching for high energy photons, in the case where no event is classified as a candidate, meaning that no air shower event in the chosen energy interval is coincident with the FRB source direction, $N_\gamma^{cand} = 0$, an upper limit can be placed instead, N_γ^{UL}, at given confidence level following the Feldman-Cousins approach [115]. In this analysis, we estimate the sensitivity of the observatory by placing an upper limit on the spectral photon fluence, which will be

computed by assuming that no photon event candidate was found and, as so, an upper limit, N_γ^{UL}, will be used.

4.1.1.1 Spectral photon fluence

The spectral photon flux is defined as the number of photons at the Earth from the FRB source per unit time and area in the energy range $[E_\gamma, E_\gamma + \mathrm{d}E_\gamma]$. The spectral photon flux, if we assume it follows a power law dependence with spectral index α, can be written as

$$\frac{\mathrm{d}\Phi_\gamma}{\mathrm{d}E_\gamma}(E_\gamma) = k_\gamma E_\gamma^\alpha, \qquad \left[E^{-1}L^{-2}T^{-1}\right] \tag{4.13}$$

where, following [112], we will take $\alpha = -2$ and k_γ is the flux normalization factor. The upper limit to k_γ can be obtained from

$$k_\gamma^{UL} = \frac{N_\gamma^{UL}}{\int_{E_0}^{E_1} E_\gamma^{-2}\, p_{\gamma-cut}\, \varepsilon(E_\gamma, \theta, \Delta t)\, \mathrm{d}E_\gamma}, \qquad \left[E^{-1-\alpha}L^{-2}T^{-1}\right] \tag{4.14}$$

where $p_{\gamma-cut}$ is the value of the cumulative photon distribution function at the $p_{\gamma-cut}-$ quantile of the photon distribution in the space of the discriminating parameter at which the final photon candidate cut is placed. Thus, $p_{\gamma-cut}$ considers the capability to discriminate between what is signal and background. Also in eq. 4.14, $\varepsilon(E_\gamma, \theta, \Delta t)$ is the SD photon exposure to a point source at zenith angle θ that initiated high energy photon showers with an energy E_γ in the time interval $\Delta t = t_1 - t_0$:

$$\varepsilon(E_\gamma, \theta, \Delta t) = \int_{t_0}^{t_1} A(t) \cos\theta(t)\, \epsilon_{SD}(E_\gamma, \theta(t))\, \Theta_{FoV}(\theta(t))\, \mathrm{d}t. \tag{4.15}$$

The zenith angle, θ, changes over time with the Earth rotation, as it is a coordinate of the horizontal coordinate system which co-rotates with the Earth. Therefore, the zenith angle is implicitly also a function of the sidereal time t, the source's right ascension and declination, through the expression [116],

$$\cos\theta(t) = \sin\lambda \sin\delta + \cos\lambda \cos\delta \cos(2\pi t/T - \alpha). \tag{4.16}$$

Here, λ is the latitude of the SD being considered, in this case the SD-433, where $\lambda = -35.4°$ and $T = 23\ \mathrm{h}\ 59\ \mathrm{min}\ 4.0905\ \mathrm{s}$ is the duration of a sidereal day. The step-function Θ_{FoV} considers the fraction of observation time in which the source is overlapped by the SD field of view (FoV), and it is 1 when the source is inside it and zero otherwise.

Finally, $A(t)$ is the aperture of the SD array and can be estimated considering that, at full

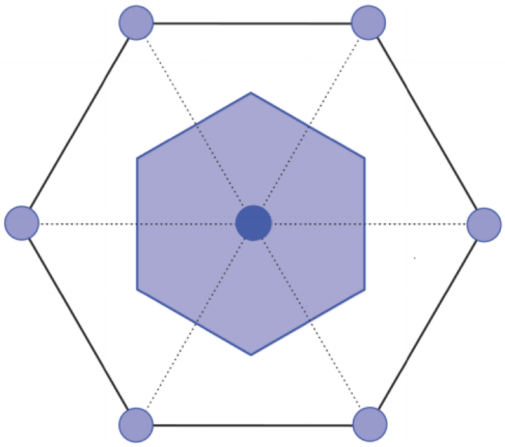


Figure 4.2: Sketch of the hexagon composed by an internal tank surrounded by 6 neighbors of SD stations separated by 433 m and the corresponding effective area, which is the shaded hexagon around the central station, for a triangular grid.

efficiency, the detection effective area per internal tank with 6 neighbors is

$$D^2 \times \sqrt{3}/2 \simeq 0.16 \text{ km}^2, \tag{4.17}$$

where D=433m is the array spacing and it corresponds to the shaded area in Fig. 4.2. The aperture then becomes

$$A(t) = 0.16 \text{ km}^2 N_{\hexagon}(t). \tag{4.18}$$

The time dependent number of hexagons of active SD stations, $N_{\hexagon}(t)$, is to be considered constant (if all tanks are working) and $N_{\hexagon}(t) = 7$ for the SD-433 station. Thus, $A = 1.12\text{km}^2$. The aperture is multiplied by a factor of $\cos\theta$ which corresponds to the effective area of the SD array when projected on the plane orthogonal to the shower axis. In eq. 4.15, $\epsilon_{SD}(E_\gamma, \theta(t))$ is the SD photon efficiency, which corresponds to the fraction of primary photons that are recorded as SD events after applying all selection cuts out of all primary photons on top of the atmosphere, see Fig. 4.3.

From the upper limit to the flux normalization factor, one can then impose an upper limit on the spectral photon fluence, $\mathcal{F}$, which is obtained by weighting the flux with the energy and integrating over the respective energy band and time interval,

$$\mathcal{F} = \int_{t_0}^{t_1} \int_{E_0}^{E_1} \frac{\mathrm{d}\Phi_\gamma}{\mathrm{d}E_\gamma} E_\gamma \, \mathrm{d}t \, \mathrm{d}E_\gamma. \tag{4.19}$$

Hence, $\mathcal{F}$ represents the total amount of energy per unit area which reaches the Earth's

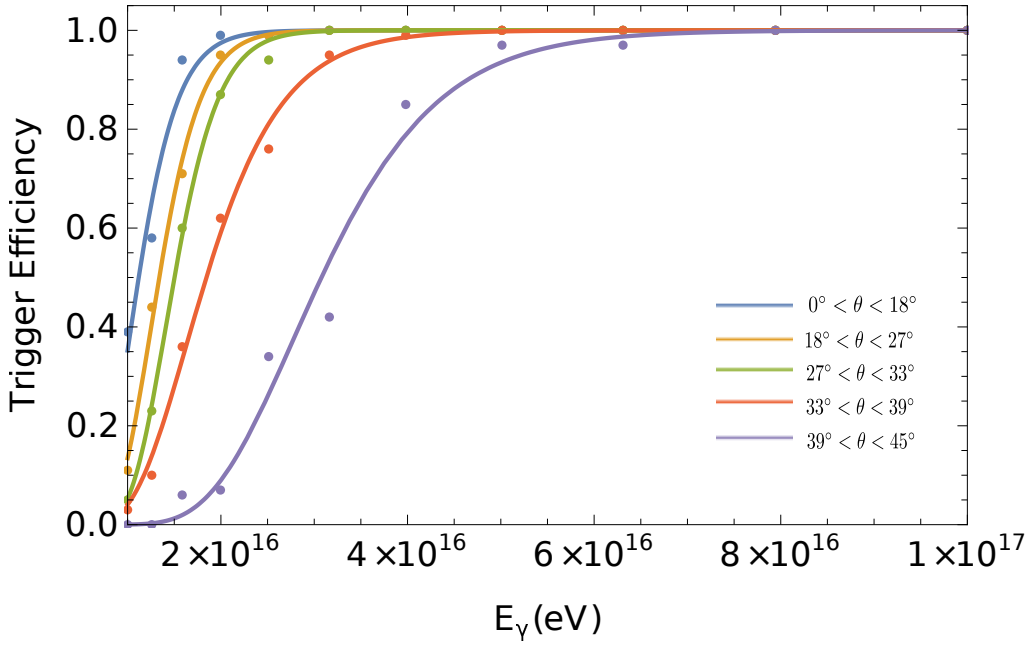


Figure 4.3: Trigger efficiency curves of SD-433 in terms of the primary energy for simulated proton events of the Pierre Auger Observatory for different intervals of θ obtained from [117].

atmosphere in the form of high energy photons. In the case $\alpha = -2$, it follows

$$\mathcal{F}_{\alpha=-2} = k_\gamma (t_1 - t_0) \int_{E_0}^{E_1} E_\gamma^{-1} \mathrm{d}E_\gamma \tag{4.20}$$

$$= \ln\left(\frac{E_1}{E_0}\right) k_\gamma (t_1 - t_0). \tag{4.21}$$

4.1.1.2 Assumptions and considerations in the analysis

In order to proceed with the analysis, there are several considerations and assumptions that are needed to be taken into account. We can start by defining the zenith angle range of the photon events we want to select. For the definition of the angular interval, we are going to use the efficiency of the SD-433, the detector used in this multimessenger study, as our guide. In Fig. 4.3, the SD-433 efficiency is depicted as a function of the simulated primary energy for protons, for five different zenith intervals between 0° and 45° [117]. These curves were calculated by adjusting the points obtained for simulated events to the following error function:

$$\epsilon_{trigger} = \frac{1}{2}\left[\,\mathrm{Erf}\left(\,\mathrm{a}(\,\log_{10}(E) - \mathrm{b}\,)\right) + 1\right]. \tag{4.22}$$

The values for the parameters a and b, for each zenith interval, can be found in table 4.1.

Zenith interval (°)	a	b
0-18	5.48	-16.049
18-27	6.16	-16.127
27-33	6.48	-16.177
33-39	4.64	-16.266
39-45	5.07	-16.488

Table 4.1: Values of the parameters a and b of Eq. 4.22 fitted to simulated events generated with energies between $10^{16} - 10^{17}$ eV.

Taking a look at Fig. 4.3, we see that the trigger efficiency is worse for the lowest energies and this effect is even more prominent for higher zenith angles. This happens because electromagnetic showers with lower energies produce less particles (check section 3.2.1) making harder the reconstruction of the event. Additionally, in an electromagnetic shower, the secondary particles are quickly absorbed into the atmosphere after the shower reaches the maximum penetration depth, $X_{\max}$. This means that lower energy or more inclined showers, with $X_{\max}$ reached at higher altitudes, will be harder to reconstruct.

We can clearly see that the efficiency increases with energy no matter the zenith angle. However, for increasingly higher zenith angles, the trigger efficiency worsens. This effect becomes particularly noticeable for the interval of $39° < \theta < 45°$ and, because of it, we will limit our analysis to photon events arriving at the observatory to θ between 0° and 45°. For the definition of the energy range there are two things to consider: the efficiency of the detector as a function of the energy which, as we can see, is limited to the range of $E > 10^{16}$ eV; the range of energies expected to be detected through the theoretical model for emission, which imposes $E < 10^{17}$ eV. Following the loaded shock scenario, we expect the production of photons with typical energies of $\sim\left[10^{11} - 10^{17}\right]$ eV [59].

In this first part of the analysis, we perform calculations considering that the source is always in the field of view of the observatory, delimited by the chosen interval for the zenith angle. This means that even though the zenith angle changes with time, in the following estimations, the source is always in the range of zenith angles chosen. And, as so, the step function is always one, $\Theta_{FoV} = 1$.

For the entirety of this analysis we used Wolfram Mathematica [118] to perform the necessary calculations and to produce the resulting graphs.

4.1.1.2.1 Perfect trigger and reconstruction efficiency

We first consider that the detection is made with perfect trigger and reconstruction efficiency, $\epsilon_{SD}(E_\gamma, \theta(t)) = 1$. If we take a look at Fig. 4.3, we quickly see that this is not necessarily a very good approximation, particularly for the lower energies considered in the analysis or for

higher zenith angles of the source. However, we can treat this first result as an approximation on the best sensitivity we can hope for in these conditions.

4.1.1.2.2 Perfect discriminant power

Another assumption left to make is on the value of the candidate cut, $p_{\gamma-cut}$. As this value relates to the ability to separate signal from background, it is useful to estimate the magnitude of background events we expect in the analysis. The following estimation is not intended to represent the exact number of background events, but rather give an idea of how relevant they are expected to be.

Regarding this study, the majority of the background events will be cosmic ray showers in the same reconstructed energy interval of the signal events and, therefore, we will approximate the background to these events. To estimate the number of cosmic ray events between $[10^{16}, 10^{17}]$ eV for a chosen time interval, we first take a look at the energy spectrum at these energies,

$$J = \frac{\mathrm{d}\phi}{\mathrm{d}\Omega \mathrm{d}E} = J_0 \left(\frac{E}{E_0}\right)^{-\gamma_0}. \tag{4.23}$$

Thus, for a given energy interval, J is approximated by a power law. For the energy interval between 1.56×10^{16} eV and 1×10^{17} eV, the exponent is $\gamma_0 = 2.83$, and for $E_0 = 5.11 \times 10^{15}$ eV, $J_0 = 9.11 * 10^{-11} \mathrm{km}^{-2}\mathrm{sr}^{-1}\mathrm{yr}^{-1}\mathrm{eV}^{-1}$ [119]. Hence, J gives the number of events for a given energy, E, per unit of area, solid angle, time and energy. Therefore, to derive the number of events, N, we integrate, giving,

$$N = \Delta\Omega\, \Delta t\, A \int_{1\times10^{16}}^{1\times10^{17}} J_0 \left(\frac{E}{E_0}\right)^{-\gamma_0} \mathrm{d}E. \tag{4.24}$$

Here, $\Delta\Omega$ is the solid angle we are considering, $\Delta\Omega = 2.3°$ [120], which is the angular resolution of the detector for a 90% confidence level (the CL we consider later in the analysis). Δt is the time interval of the follow-up search that we set at 1 s and A is the effective area of the detector, in this case $A = 1.12\,\mathrm{km}^2$. The number of estimated events then becomes,

$$N \sim 10^{-5}\,\text{events}. \tag{4.25}$$

So, if we are considering small intervals of time, the expected number of background cosmic ray events is much smaller than the number of expected photon (signal) events when we consider a close source with $d = 0.1$ kpc (check eq. 4.7). If we consider small time periods, we do not expect any background event to be reconstructed by our detector.

Taking this in mind, and continuing with the idea that we are constructing the best case

scenario with respect to the sensitivity of detection, we assume that we have perfect discriminant power, meaning that $p_{\gamma-cut} = 1$. So, not only the background is zero, but also the efficiency of photon selection in the discriminant analysis is 100%. Using the Feldman-Cousins (FC) approach, upper limits to the expectation value of the number of photon candidates can be placed at a given confidence level (CL). The FC confidence intervals depend on the amount of expected background contamination in the signal region. For example, the larger the background, the higher are the upper limits one can impose. As the expected background is very small, the upper limit estimation for the number of candidates will be made assuming zero background. The Feldman-Cousins upper limit for a measured signal of zero events with no background at 90% CL is $N_{\gamma}^{UL} \approx 2.44$ [115].

4.1.1.3 Exposure

We proceed with the analysis by estimating the exposure using eq. 4.15. In this case, the calculation becomes very simple, as the source is always inside of the observatory's FoV, $\Theta_{FoV} = 1$, the aperture is time independent, $A = 1.12\,\mathrm{km}^2$ and the trigger and after cuts efficiency is always one, $\epsilon_{SD}(E_{\gamma}, \theta(t)) = 1$. Inside of the integral we have a factor of $\cos(\theta(t))$, and therefore the value found for the exposure depends on the time interval we choose, the initial value of the zenith angle and how the zenith angle varies in time. For increasingly bigger zenith angles, the effective area of the detector decreases and so does the exposure. The time evolution of the zenith angle depends on the declination of the source, as the field of view of Auger rotates in the direction of the right ascension, completing a turn in a day. For a given declination and right ascension of a source, the zenith angle can either increase or decrease over time whether the field of view of the observatory is coming closer or further away of the position of the source.

We start by setting the time interval for 1 second as, according to the baryon loaded shock scenario [59], the time frame is big enough for most of the neutrino/photon emission to have already happened. For the time dependent zenith angle, $\theta(t)$, we set it to be $\sim 15°$ at the beginning of the search and to be increasing with time, with the behavior shown in Fig. 4.4. We can see from this graph that the zenith angle does not change much for small time intervals. The value found for the exposure is $\varepsilon_{per.eff.} = 1.0803 \times 10^{10}\,\mathrm{cm}^2\mathrm{s}$.

4.1.1.4 Upper limit to the flux normalization factor at 90% CL

We proceed with the analysis by computing the upper limit for the flux normalization factor, k_{γ}^{UL}. As was already mentioned, the upper limit on the number of candidate events is $N_{\gamma}^{UL} \approx 2.44$, $p_{\gamma-cut} = 1$ and the energy interval to be integrated is $[10^{16}, 10^{17}]$ eV. The value found is $k_{\gamma}^{UL} \sim 0.0025\,\mathrm{GeV\ cm}^{-2}\mathrm{s}^{-1}$.

In order to better understand how this quantity depends on the energy, k_{γ}^{UL} was estimated

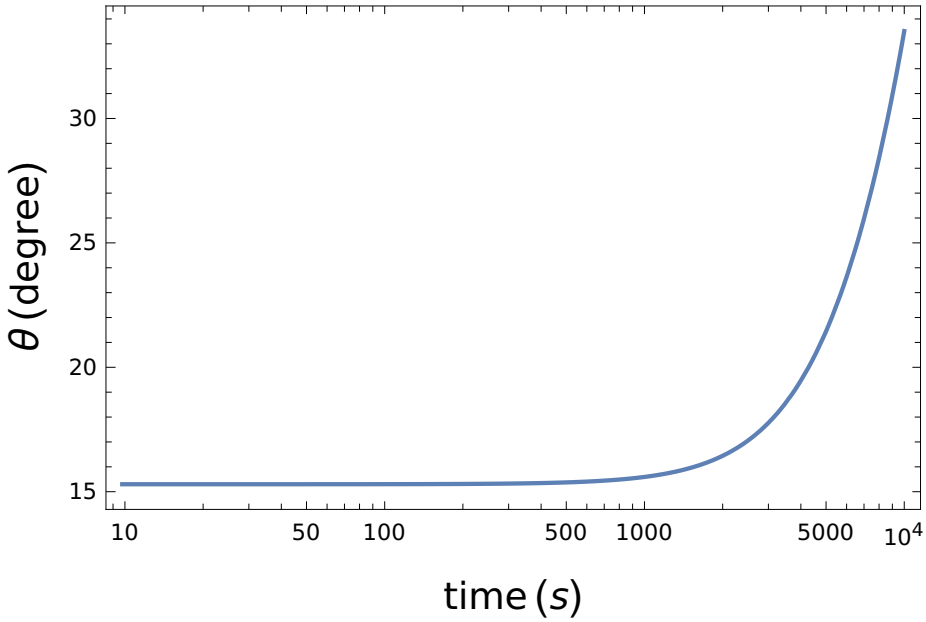


Figure 4.4: Time evolution of the zenith angle, initially set as $\sim 15°$. The time evolution of the zenith angle depends on the declination of the source, which for this case is $\delta \sim -50.7°$.

for five energy intervals within $[10^{16}, 10^{17}]$ eV and the resulting plot can be found in Fig. 4.5. As k_γ^{UL} is energy dependent, we see that for higher energies the upper limit for the normalization factor increases, as expected from eq. 4.14 for a constant exposure.

4.1.1.5 Upper limit to the spectral photon fluence at 90% CL

Using eq. 4.20 we estimate the upper limit for the spectral photon fluence at 90% CL, $\mathcal{F}_\gamma^{UL}$, to understand the sensitivity of the SD-433 to high energy photons. The idea is to discern if observations with the Pierre Auger Observatory can constrain the theoretical predictions coming from the baryon loaded shock scenario, see Fig. 2.13. The value found is $\mathcal{F}_\gamma^{UL} \sim 0.0057\,\text{GeV cm}^{-2}$.

Similarly to what happened with the flux normalization factor, we decided to estimate $\mathcal{F}_\gamma^{UL}$ for five energy intervals within $[10^{16}, 10^{17}]$ eV, and the resulting plot can be found in Fig. 4.6. These curves intend to replicate the sensitivity curves found on the right hand side graph of Fig. 2.13 for the case of high energy photon detection with the Pierre Auger Observatory.

If we take a look at the graph corresponding to the γ-ray fluence due to neutral pion decay in Fig. 2.13, and take an optimistic estimate of the order of magnitude for the expected fluence in the $[10^{16}, 10^{17}]$ eV energy interval for a source at 0.1 kpc of $\sim 10^{-3}\,\text{GeV cm}^{-2}$, we see that we do not expect to be able to constrain this model with photon detection using the SD-433 of the Pierre Auger Observatory. Moreover, it is important to highlight the fact that

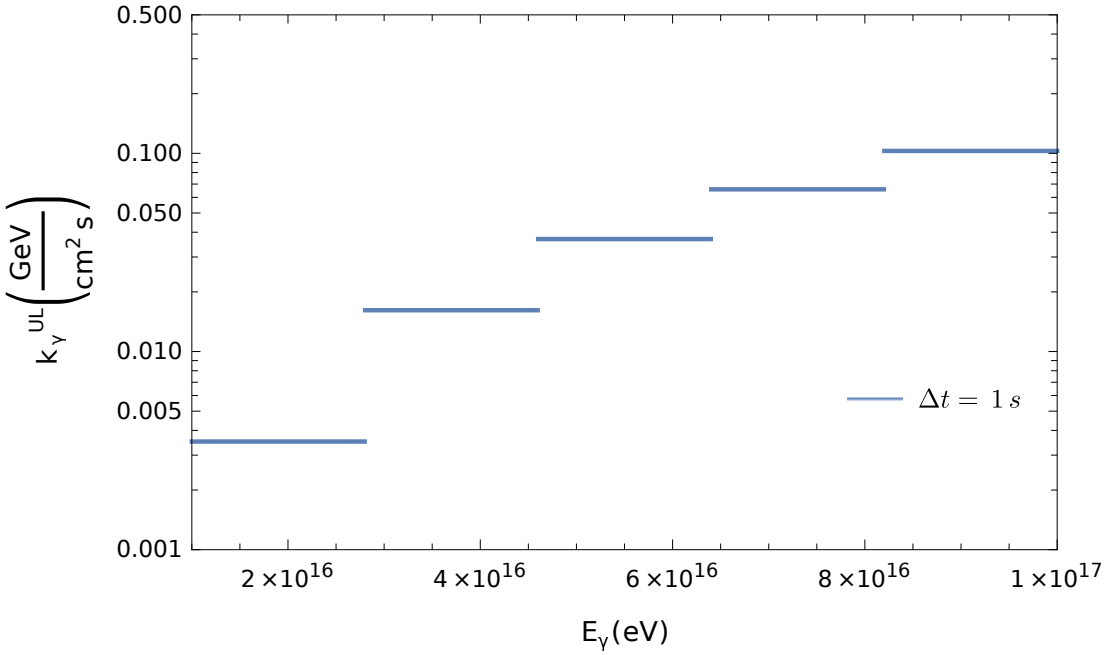


Figure 4.5: Estimated upper limit to the flux normalization factor, k_γ^{UL}, arriving to the SD-433 in the Pierre Auger Observatory for 1 second considering perfect trigger efficiency for five bands within the energy interval $[10^{16}, 10^{17}]$ eV.

we are looking at the best case scenario both regarding the sensitivity of the detector, where we consider a perfect discriminant power, a perfect trigger efficiency and that the source is always in the detector's field of view, as well as regarding the predicted fluence, where the FRB burst considered possesses a radio energy five orders of magnitude larger than the estimated value for FRB200428, the galactic FRB. Additionally, FRB200428 has its source at a distance of $\sim$ 10 kpc and, for this distance, the predicted fluence will have decreased by four orders of magnitude, as the predicted γ-ray fluence decreases with the square of the distance, see Fig. 2.13. Thus, we are looking at the ideal FRB burst for the detection of a high energy photon counterpart, which has not been detected yet.

The next step is to perform the same analysis with more realistic parameters and understand their effect on the results, meaning how much farther is the estimated sensitivity to the spectral fluence predicted by the baryon loaded shock scenario. Also, to study the behavior of sensitivities estimated using more realistic quantities and their dependencies. Later, we evaluate the impact of searching, not only with one, but with a big statistic of FRB events.

4.1.1.6 Introducing a realistic trigger efficiency

We can improve the estimate for the upper limit for the spectral photon fluence at 90% CL, $\mathcal{F}_\gamma^{UL}$, by introducing a realistic trigger efficiency of the SD-433. Moreover, by considering a realistic trigger efficiency, we can then analyze the amplitude of its effects.

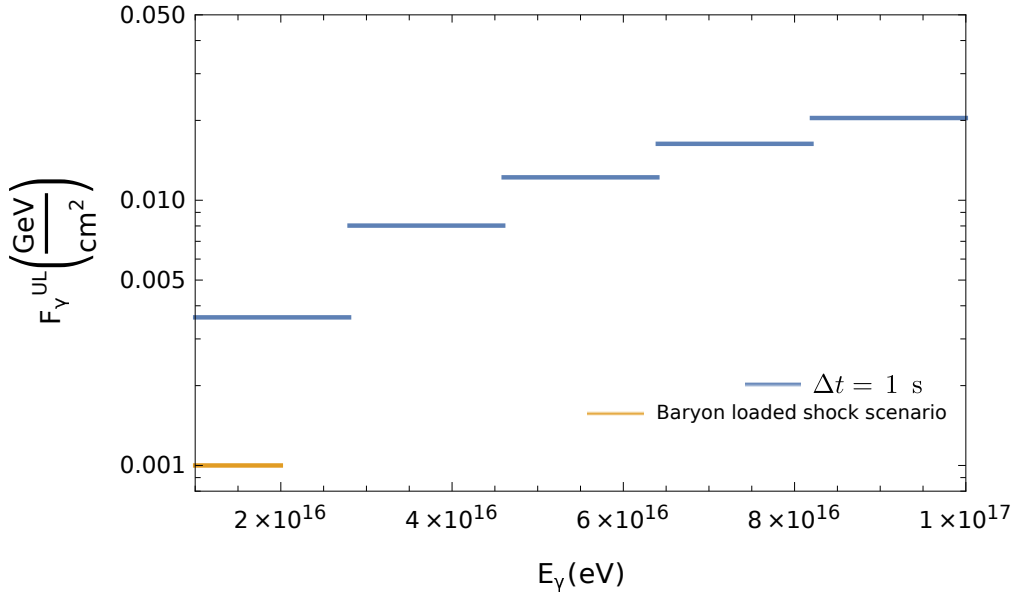


Figure 4.6: Estimated upper limit to the spectral photon fluence at 90% CL, $\mathcal{F}_\gamma^{UL}$, arriving to the Pierre Auger Observatory for 1 second considering perfect trigger efficiency for five bands within the energy interval $[10^{16}, 10^{17}]$ eV. In yellow is the reference value for the magnitude of the photon fluence predicted by the baryon loaded shock scenario for a source at d= 0.1 kpc, see Fig. 2.13.

The trigger efficiency, $\epsilon_{SD}(E_\gamma, \theta(t))$ has two dependencies: one on the energy of the event, E_γ, and other on its zenith angle, $\theta(t)$, which is time dependent as well. In order to simplify the problem, these two dependencies have been separated, leaving us with five different efficiency curves as a function of energy, for five different complementary zenith angle intervals, between $0° < \theta < 45°$[117]. The behavior of the five curves can be seen in Fig. 4.3, which have been approximated by adjusting the points in the graph to error functions, which are also shown.

We can perform the exact same calculations as before, for the same conditions, only now using the realistic trigger efficiency. In Fig. 4.7, we can see both estimations for one second and $\theta \sim 15°$, for the $\left[10^{16}, 10^{17}\right]$ eV energy interval. The only difference that can be seen appears in the lowest energy bin, since for small zenith angles, the trigger efficiency quickly goes to one with increasing energy.

4.1.1.6.1 Effect of the zenith angle

We would not expect the above result to be necessarily true for higher zenith angles within the chosen interval, $0° < \theta < 45°$. Therefore, we can evaluate how the estimated upper limits change when we perform exactly the same analysis for five different initial zenith angles, each belonging to a different trigger efficiency curve. This analysis was performed for a 1 s interval for events with zenith angle (θ) approximately 15°, 20°, 30°, 35° and 40°. The exposure for

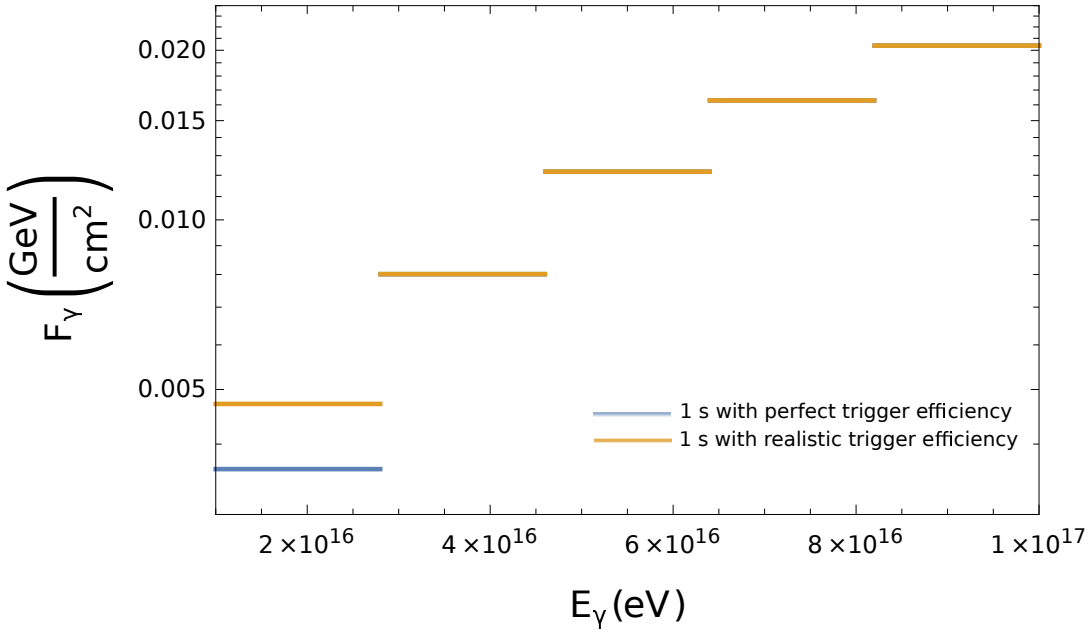


Figure 4.7: Estimated upper limit to the spectral photon fluence, $\mathcal{F}_\gamma^{UL}$, at 90% CL for photon events arriving to the Pierre Auger Observatory with zenith angle $\theta \sim 15°$ for 1 second considering perfect trigger efficiency (in blue) and the trigger efficiency curves from [117] (in orange).

the 5 different sources has now an energy dependence which can be seen in Fig. 4.8. In this figure we can see that this dependence is in agreement with the previous information coming from the trigger efficiency. If we take a look at eq. 4.15 and take in consideration that, in the 1 second interval, the variation of the zenith angle is very small (see Fig. 4.4) we can then grossly estimate that the trigger efficiency is time independent in this small time interval. Using this approximation, it is clear to see the direct impact that the trigger efficiency has on the energy dependence of the exposure. For the lowest energies, the exposure increases with energy as the trigger efficiency also increases. When the trigger efficiency reaches its maximum so does the exposure.

We continue the analysis with the estimation of the upper limit for the flux normalization factor, k_γ^{UL}, for each of the five sources. The evaluation was performed similarly as before and the result can be found in Fig. 4.9. There, we can clearly see that the small impact of introducing a realistic trigger efficiency for a source at a small zenith angle, in the previous case $\theta \sim 15°$, translates into a much bigger impact for a source at the highest end of the θ interval and this impact propagates to higher energies. For the highest θ interval, the effect is big enough for the upper limit to increase with energy for the first bins of the interval, reversing the original tendency.

Next, we can see what happens to the upper limit to the spectral photon fluence, $\mathcal{F}_\gamma^{UL}$, at 90% CL for the five cases, check Fig. 4.10. For the lowest energies, the estimated upper

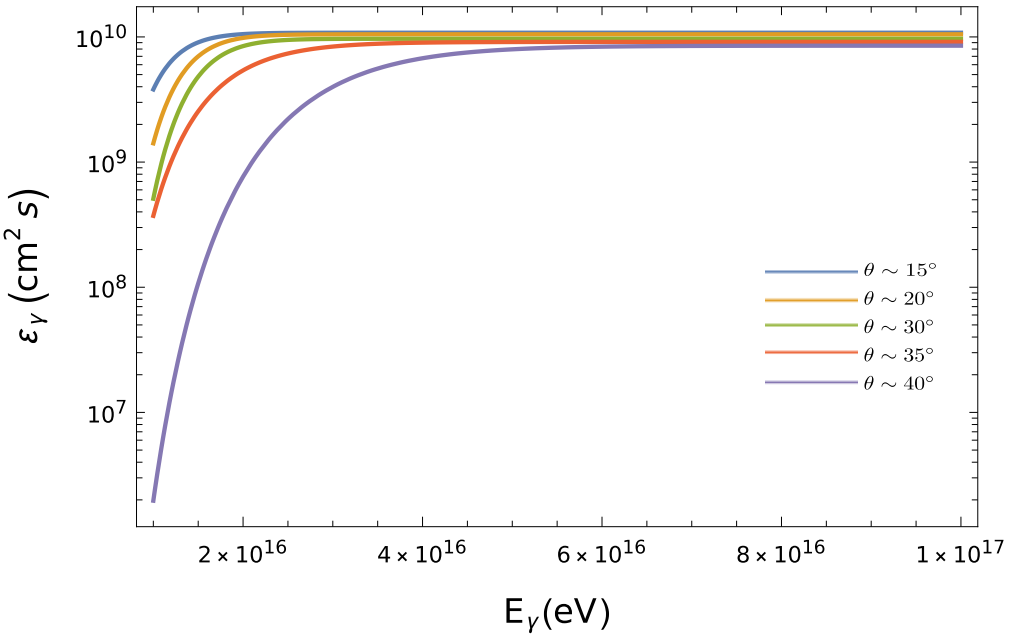


Figure 4.8: Exposure for photon events arriving to the Pierre Auger Observatory with zenith angle (θ) approximately 15°, 20°, 30°, 35° and 40° for 1 second.

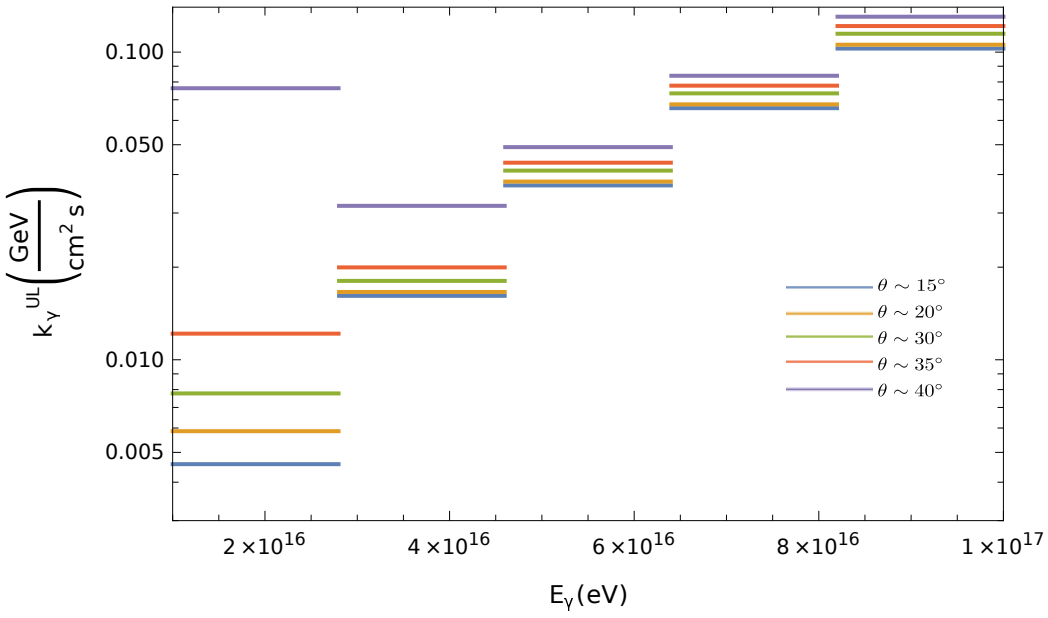


Figure 4.9: Upper limit to the flux normalization factor, k_γ^{UL}, at 90% CL for photon events arriving to the Pierre Auger Observatory with zenith angle (θ) approximately 15°, 20°, 30°, 35° and 40° for 1 second.

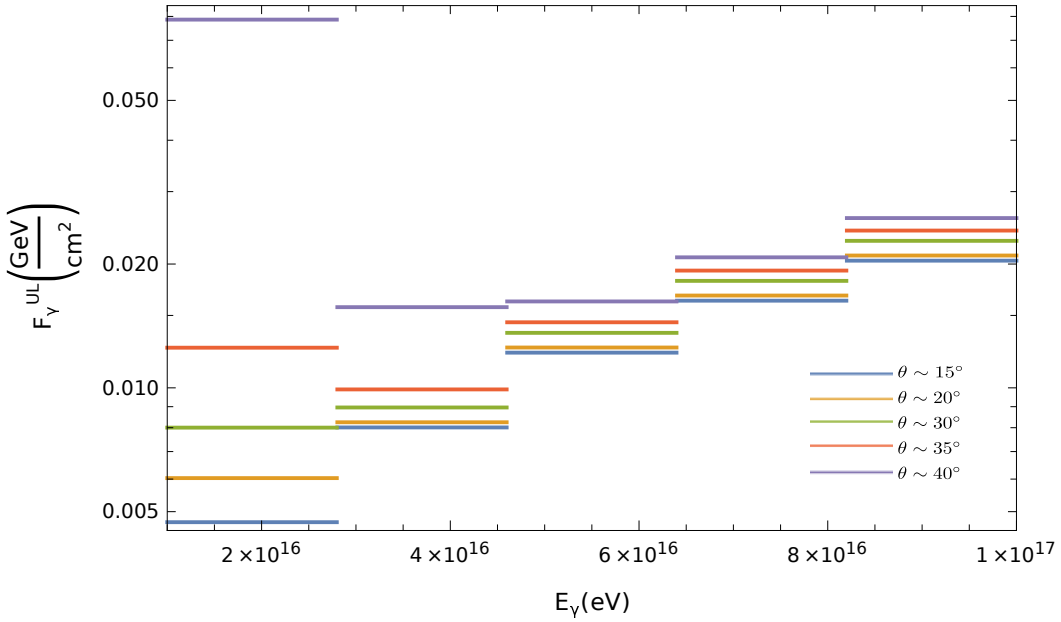


Figure 4.10: Upper limit to the spectral photon fluence, $\mathcal{F}_\gamma^{UL}$, at 90% CL for photon events arriving to the Pierre Auger Observatory with zenith angle (θ) approximately 15°, 20°, 30°, 35° and 40° for 1 second.

limit increases considerably with the initial θ used, and for the two highest values of θ, the sensitivity for the bin with lower energy is smaller than in the following energy bin.

Another important aspect to notice is that, as these five sources have different zenith angles, as seen by the observatory at any given time, their exposure is not expected to be equal even if we had considered a perfect trigger efficiency in the analysis. This happens because the effective area of the detector is smaller for increasing θ. Thus, even for the higher energies, the exposure is lower for higher zenith angles. This dependency also translates into different values found for the upper limit on the flux normalization factor and the spectral fluence for different θ for the higher energy bins, where the trigger efficiency equals one, no matter the θ.

4.1.1.6.2 Effect of the time interval

The next part of the analysis has the objective of understanding the effect of the time interval considered on these three quantities: the exposure, $\varepsilon(E_\gamma, \theta, \Delta t)$, the upper limit to the flux normalization factor, k_γ^{UL}, and the spectral fluence, $\mathcal{F}_\gamma^{UL}$. To that effect, we consider exactly the same source as initially, where $\theta \sim 15°$, but now redo the calculations for four different time intervals 1, 100, 1000 and 10000 seconds. The time evolution of the zenith angle for the total 10000 s can be seen in Fig. 4.4. One important aspect to be noted is the fact that the time evolution of the zenith angle depends both on the localization of the source and the localization of Auger's FoV in the moment of detection, i.e., the sidereal time of detection,

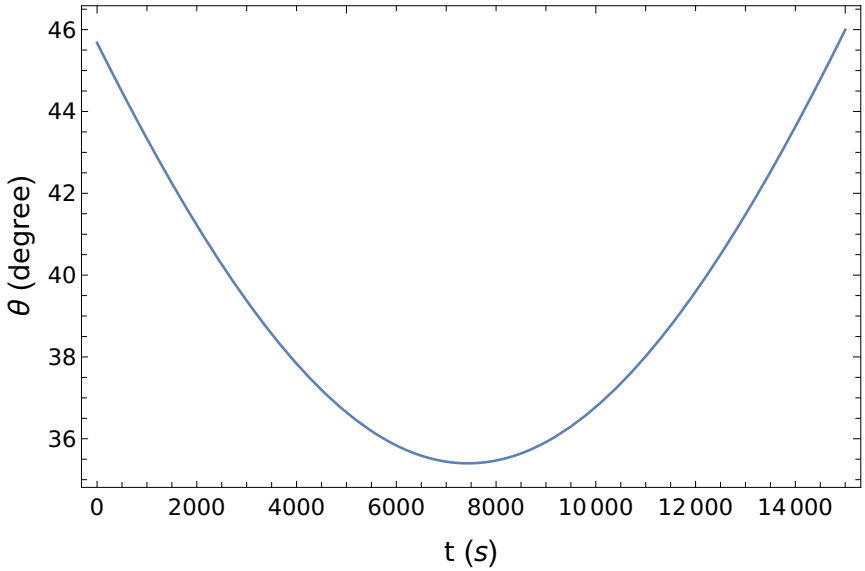


Figure 4.11: Time evolution of the zenith angle (θ) for the transit of a source, for which the FoV initially comes closer until it reaches its minimum and then moves away.

(see eq. 4.16). Hence, since the effective area and the trigger efficiency depend on the time evolution of the zenith angle, we will have to be careful to reach conclusions about the general effect of the time window in the analysis. If we take a look at Fig. 4.4, we see that, in this case, the zenith angle is always increasing with time during the 10000 s. However, as already been warned, that does not have to be the case. The zenith angle either increases or decreases depending on whether the FoV of Auger is coming closer to the source or further away. To demonstrate this, we show in Fig. 4.11 an example of the transit of a source, for which the FoV initially comes closer and then moves away. This transit was performed for a source at right ascension $\alpha \sim 31°$, declination $\delta \sim 0°$ and sidereal time $t \sim 0$ s.

Additionally, it is also possible to see that, in this case, the source passes through all of the trigger efficiency bands in the 10 000 s. Nonetheless, the time window is not big enough for it to pass the maximum value of 45°. As has already been mentioned, the assumption is that the source is always inside the FoV of Auger limited by the θ interval set.

We can now advance to the estimation of the exposure for the four time intervals, which can be found as a function of the energy in Fig. 4.12. The approximation that the zenith angle is constant during the analysis is not valid anymore (again take a look at eq. 4.15). In this expression, the two time dependent quantities to be integrated are the efficiency, $\epsilon_{SD}(E_\gamma, \theta(t))$, and the effective area of the detector, $A\cos(\theta(t))$. As the curves were evaluated by performing the time integral, we see that they appear translated by the same order of magnitude as the ratio between the time intervals.

The trigger efficiency is only different from unity for the lower energies and it is responsible for the energy dependency of the exposure, including for which energy it reaches its maximum

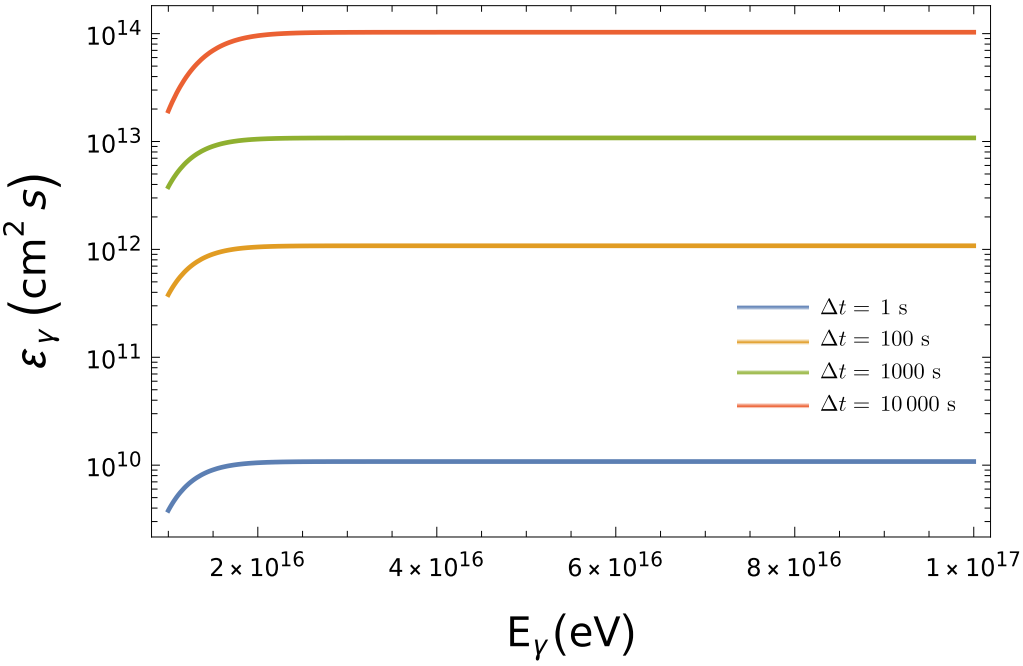


Figure 4.12: Exposure for photon events arriving to the Pierre Auger Observatory with zenith angle $\theta \sim 15°$ for 1, 100, 1000 and 10 000 seconds.

value. For the 10 000 s curve, the increase of the exposure with the energy is slower just before it reaches its maximum value, compared to the 1 s case because, over time, the trigger efficiency curve changes and the contribution for the exposure decreases. The effective area is not energy dependent and, as so, its effect on these curves translates into a multiplicative factor. Here, the effective area is decreasing over time resulting in a slight decrease of what would be the exposure if the effective area was constant. If, however, the zenith angle decreased over time, both the effect of the effective area and the trigger efficiency would be reversed.

The flux normalization factor has the reverse tendency as the exposure, as shown in Fig. 4.14. Then, for the smallest time window, 1 s, the exposure is the smallest but the upper limit to the flux normalization factor is the highest. The small effect of the realistic trigger efficiency can be seen once again for the first energy bin and the effect of the decreasing effective area is again a multiplicative factor.

To estimate the upper limit to the spectral fluence, $\mathcal{F}_\gamma^{UL}$, we multiply once again by the length of the time interval being considered. This means that the big separation of the curves in both the exposure and k_γ^{UL} does not exist in the case of $\mathcal{F}_\gamma^{UL}$. Thus, for the same energy interval, the separation between the curves of different time intervals arises because of effects of the zenith angle evolution over time. In this scenario, the zenith angle increases over time, and therefore, in Fig. 4.14 we can see a big separation in the first energy bin between the three curves of 1, 100 and 1000 seconds (which are overlapped) and the 10000 seconds curve because

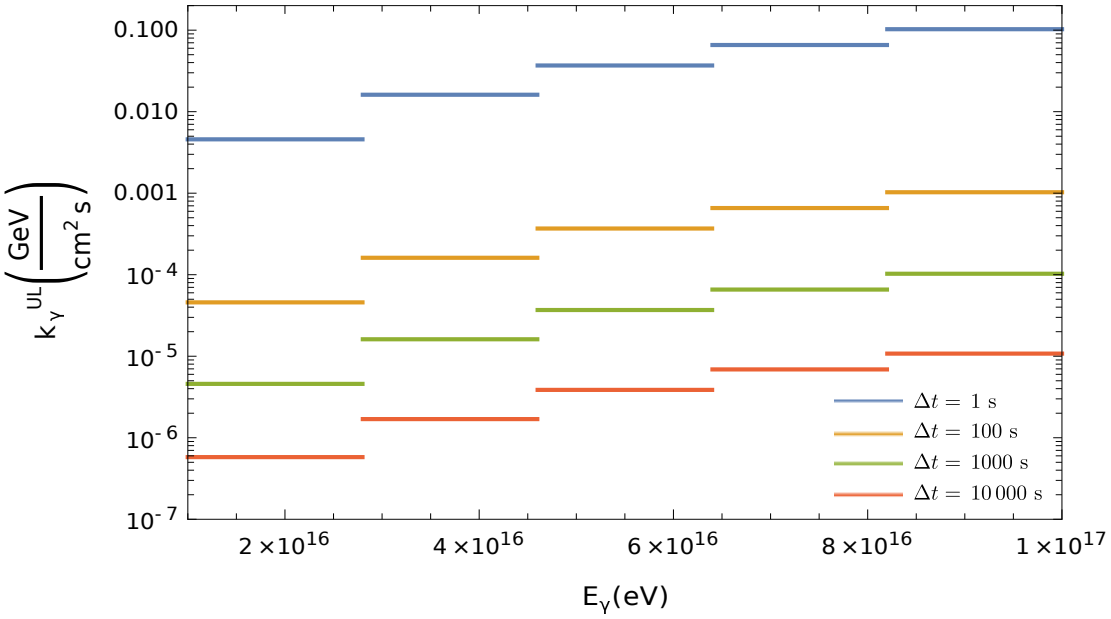


Figure 4.13: Estimated upper limit to the flux normalization factor, k_γ^{UL}, at 90% CL for photon events arriving to the Pierre Auger Observatory with zenith angle $\theta \sim 15°$ for 1, 100, 1000 and 10 000 seconds.

of the trigger efficiency and a small separation between the same curves for the other energies bins due to the time evolution of the effective area. Hence, if the zenith angle decreased over time, this tendency would be completely reversed and the sensitivity of our detector would increase for bigger time intervals.

A very noticeable characteristic of Fig. 4.14 is the fact that we do not have a clear separation between the first three curves. This happens because of the way the zenith angle evolves in this case. It changes very slowly on the first 1000 s and much faster after, see Fig. 4.4, so the differences caused by the θ evolution for the first three curves are very small. That is also the reason why we considered such diverse time intervals to be able to study their effect on the analysis, as the approximation made previously regarding the background only makes sense when considering smaller time windows, check subsection 4.1.1.2. If, however, we are considering larger time windows, the upper limit to the number of candidates decreases. For example, when $N_{background} \simeq 0.5$ events, which corresponds to a time window of 50000 s, $N_\gamma^{UL} \simeq 1.94$ [115].

Also, in Fig. 4.14, we can once again see the exemplifying reference to the predicted photon fluence for a very bright and nearby FRB coming from the baryon loaded shock scenario. Its presence serves to reiterate the conclusion that the Pierre Auger Observatory does not seem to be the best detector to perform this analysis on finding photon counterparts to FRBs since it is not likely to be able to constrain the theoretical model unless in the future a very bright, $\varepsilon_{\text{radio}} \gtrsim 10^{40}$ erg, and nearby source, $d \lesssim 0.1$ kpc, is detected.

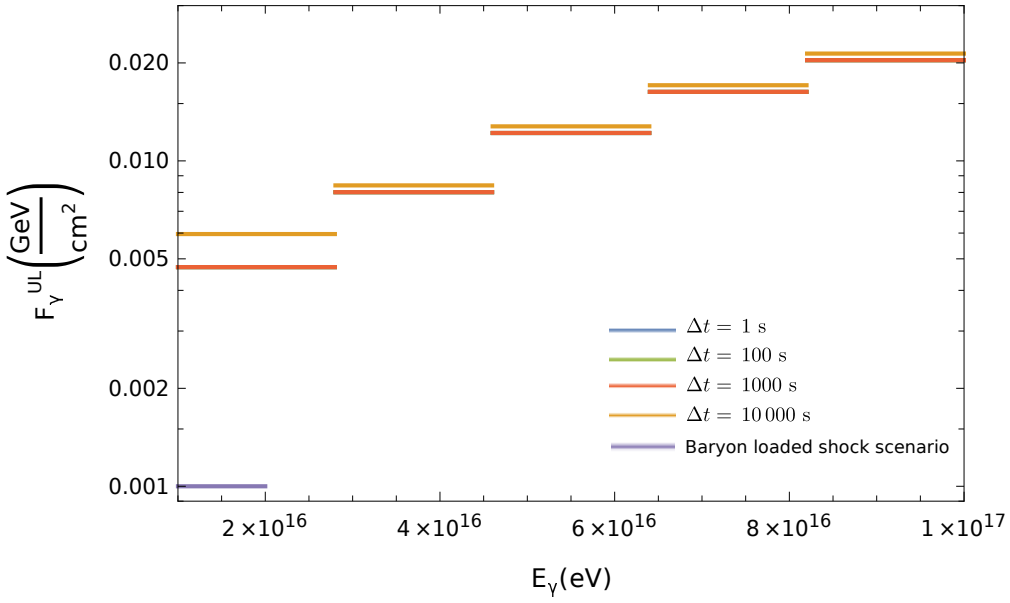


Figure 4.14: Estimated upper limit to the spectral fluence, $\mathcal{F}_\gamma^{UL}$, at 90% CL for photon events arriving to the Pierre Auger Observatory with zenith angle $\theta \sim 15°$ for 1, 100, 1000 and 10 000 seconds. In purple is the reference value for the magnitude of the photon fluence predicted by the baryon loaded shock scenario for a source at d= 0.1 kpc, see Fig. 2.13.

4.1.2 FRB localization and Auger's field of view

To perform a follow-up analysis using catalogued FRB events, one needs to understand the detector's field of view and how it evolves in a sidereal day. When, in the previous analysis, we defined the zenith angle interval of detection to $0° < \theta < 45°$, we limited the area for searching counterparts to about half of the sky, see the blue region in Fig. 4.15.

In the case of the Pierre Auger Observatory, only a small fraction of FRB detections are included in the total region in the sky for $0° < \theta < 45°$, during a sidereal day. This means that, if we are using catalogued events for the search, it is important to use observatories that can complement the research. In Fig. 4.15 we see that by considering both Auger and LHAASO, we can cover most of the sky for the counterpart search. As LHAASO is in China, in the northern hemisphere, and SWGO is to be built in the southern hemisphere, these two detectors can also be complementary in a wide search for photon FRB counterparts (see the maximum/minimum field of view declinations for both detectors in table 4.2). However, this will only be true if their instantaneous FoV intersect with the FoV of the FRB surveys, which are limited and for that, their longitude will be relevant, as we will see in the next subsection.

At any given moment, the field of view of one of these detectors, for $0° < \theta < 45°$, only covers a smaller part of the sky. Moreover, the fraction of the day for which a point in the sky is inside the field of view of the detector will depend on its declination. This dependence

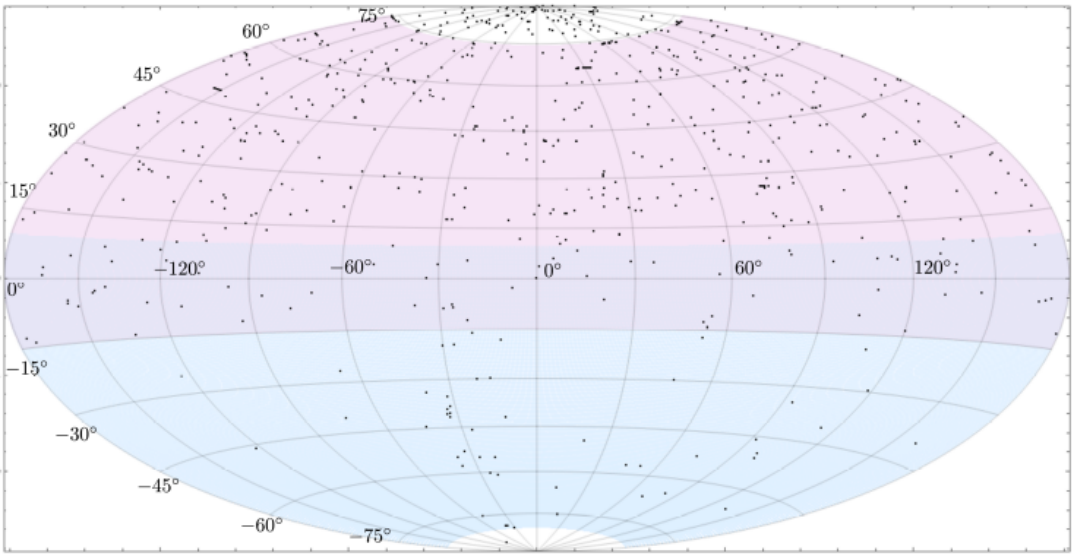


Figure 4.15: Localization of 774 fast radio bursts plotted using equatorial coordinates (source: Transient Name Server (TNS)). The shaded regions are the total region in the sky observed by the Pierre Auger Observatory (blue) and by LHAASO (pink) for $0° < \theta < 45°$ plotted using equatorial coordinates.

is represented in Fig. 4.16 for the field of view of Auger and for a zenith angle between 0° and 45°. We further address this aspect in the following section 4.1.4.

4.1.3 Sensitivity studies considering other observatories

The Pierre Auger Observatory may not be the best detector to constrain the baryon loaded scenario. On the other hand, the sensitivity curves of HAWC, in Fig. 2.13, show that it can possibly constrain the theoretical model for photon emission. We now evaluate if there are lower energy detectors with better or comparable sensitivity to HAWC. For this effect, we consider two different detectors - LHAASO and SWGO.

In table 4.2 we present some characteristics of these two detectors, HAWC and the SD-433, that are relevant for this analysis. The maximum and minimum declination of the field of view of the detector for $\theta < 45°$ are, as already been discussed, quite important as they constrain the total search area of each detector (in a day) to about approximately half of the sky. Moreover, the field of view of each observatory in any given moment will be smaller. This means that complementing southern with northern, as well as eastern and western detectors, becomes important, as we will describe in the next subsection.

We continue the estimate of the exposure for these three detectors for similar conditions to the initial analysis. Thus, we are again considering the zenith angle interval between 0° and 45°, see [121, 122], and the energy range for each of the three detectors, HAWC, SWGO and LHAASO, will be the corresponding interval that appears in table 4.2.

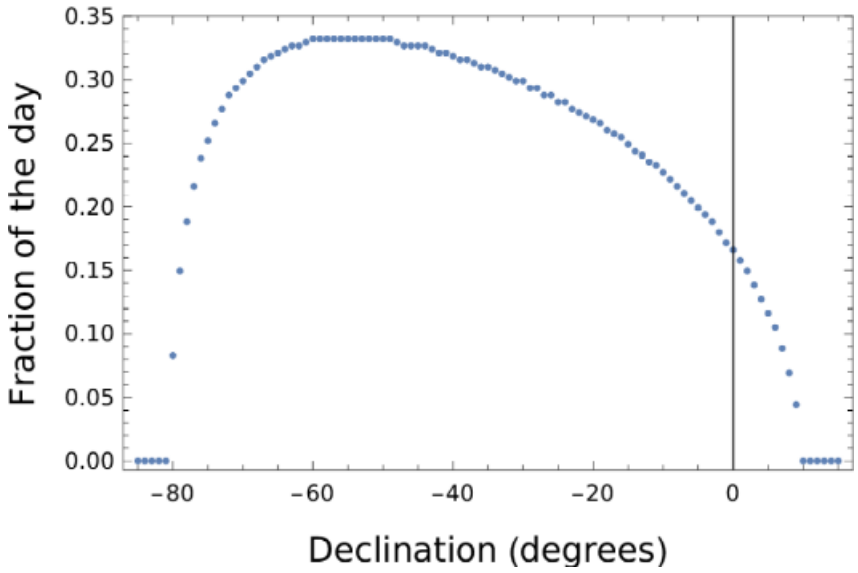


Figure 4.16: Fraction of a sidereal day for which the instantaneous field of view for zenith angles $\theta < 45°$ of the Pierre Auger Observatory covers a point in the sky as a function of its declination.

	Auger (SD433)	HAWC	SWGO	LHAASO
Area (m^2)	1.12 x 10^6	2 x 10^4	2.21 x 10^5 / 5 x 10^6	1 x 10^6
Energy Range (eV)	[10^{16} ,10^{17}]	[10^{11},10^{14}]	[10^{11},10^{15}]	[10^{11},10^{15}]
Longitude	69° 18' 57" W	97° 18' 30" W	67° 45′ 12″ W	100° 08′ 15″ E
Latitude	35° 12' 24" S	18° 59' 41" N	23° 01′ 09″ S	29° 21′ 31″ N
Maximum Dec (θ<45°)	9.5°	63.5°	22°	74°
Minimum Dec (θ<45°)	-80.3°	-26°	-67.5°	-15°

Table 4.2: Properties of high energy photon detectors, namely, the area, energy range, localization and maximum/minimum declination of the field of view of the detector for $\theta < 45°$ for the SD-433 of the Pierre Auger observatory [109], HAWC [101], SWGO [103], and LHAASO [102].

Detector	Exposure (cm^2s)
HAWC	$\sim 2 \times 10^8$
LHAASO	$\sim 9 \times 10^9$
SWGO ($2.21 \times 10^5 m^2$)	$\sim 2 \times 10^9$
SWGO ($5 \times 10^6 m^2$)	$\sim 5 \times 10^{10}$

Table 4.3: Estimated exposure found for HAWC, LHAASO and SWGO for a 1 second analysis with initial zenith angle $\theta \sim 15°$.

We also consider that the detection is made with perfect trigger and after cuts efficiency, $\epsilon_{SD}(E_\gamma, \theta(t)) = 1$, that the source is always in the field of view of the observatory, $\Theta_{FoV} = 1$ and assume that there is a perfect discriminant power, i.e., $p_{\gamma-cut} = 1$. The analysis is done for 1 second for a source at $\theta \sim 15°$. For SWGO the evaluation was made considering two different possible areas for the detection.

Regarding the use of a perfect discriminant power, the assumption of a small number of background events is no longer valid. In fact, the flux of cosmic rays, for these lower energies, will be much higher since $\gamma_0 \sim 3$ (see eq. 4.23) for most of the cosmic ray spectrum. Thus, this constitutes a simplification of the analysis, having in mind that the objective is to understand what is the order of magnitude of the sensitivity of these three detectors and which properties of the detector maximize it. One can also assume, in a following step, a certain power to reject the background, which will affect N_γ^{up}, and an efficiency of signal selection $p_{\gamma-cut}$.

In table 4.3 we find the estimated exposure for the three detectors and the differentiating factor between the values found is the area of the detector. The bigger the area, the bigger is the exposure, see eq. 4.15. In a follow-up analysis, an important factor to consider is how the localization of the observatory relates to the localization of the FRB detectors. Additionally, as a close, galactic, FRB is needed for being possible to constrain a theoretical model for the emission of FRB counterparts, it is important that the Milky Way is inside the observatory's FoV.

Next we can take a look at what happens for the upper limit to the spectral fluence, $\mathcal{F}_\gamma^{UL}$, at 90% CL, for photon events arriving to HAWC, LHAASO and SWGO for the 1 second case in Fig. 4.17. As we are comparing different detectors with different localizations for the zenith to be the same, the localization of the source will be different. For LHAASO and SWGO, as the upper limits are being estimated for the same energy intervals, the difference in the curves relates directly to the detectors' area. Thus, the bigger the detector, the better the sensitivity, which means that the optimal detectors to constrain the theoretical model will maximize the detection area.

When we look at the upper limits imposed, we see that LHAASO and SWGO have a clear advantage in comparison with HAWC. These two detectors explore almost the entire energy

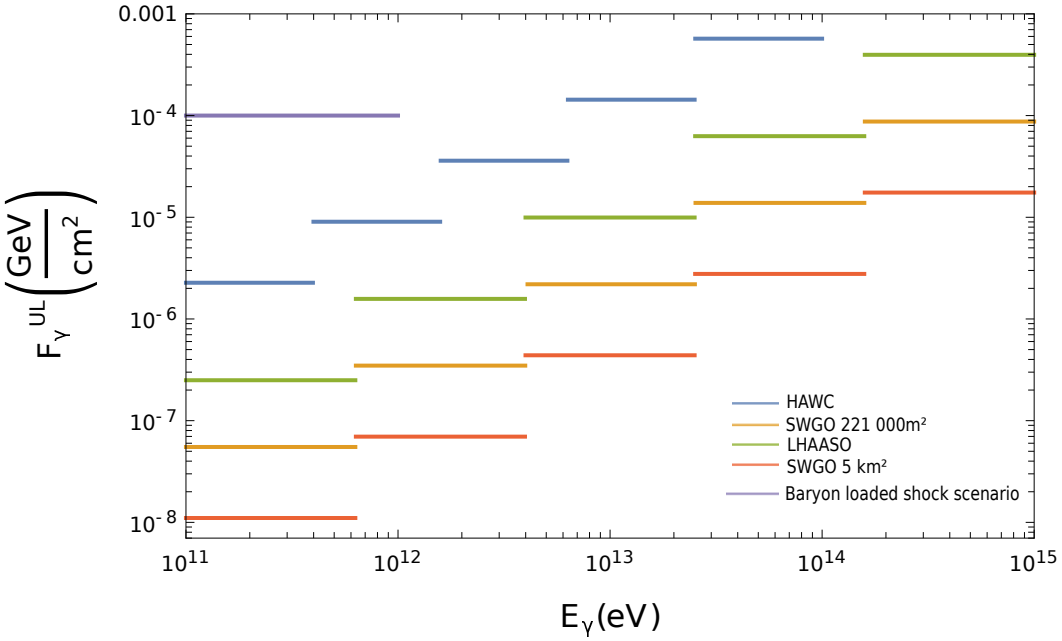


Figure 4.17: Estimated upper limit to the spectral fluence, $\mathcal{F}_\gamma^{UL}$, at 90% CL for photon events arriving to HAWC, LHAASO and SWGO with zenith angle $\theta \sim 15°$ for 1 second. In purple is the reference value for the magnitude of the photon fluence predicted by the baryon loaded shock scenario for a source at d= 0.1 kpc, see Fig. 2.13.

interval of predicted photon emissions, while additionally maximizing the exposure with their large surface areas. Nonetheless, a large surface area is not all that important in regards to the detectors characteristics, as the localization can be fundamental in determining the ability of a detector to search for FRB counterparts. Also, in Fig. 4.17, we see the reference value for the magnitude of the fluence predicted by the baryon loaded shock scenario for a very nearby source, $d \sim 0.1$ kpc, and bright FRB.

It is relevant to mention that the sensitivity of HAWC estimated in this analysis is not, as expected, exactly the same as the one found in Fig. 2.13. The curves were evaluated considering a realistic trigger and reconstruction efficiency and considering the effects of the background in the analysis [81].

Finally, it is important to reiterate that these curves were estimated for ideal conditions and that, for more realistic conditions, we would expect considerable differences, particularly at the lower energies. In a more realistic analysis, the background would have to be taken into consideration, since for the range of energies considered, the number of background events in a 1 s interval would be $\sim 10^3$. Therefore, the discriminant power of the detector becomes crucial. Additionally, if a realistic trigger efficiency was introduced in the analysis, one would expect an increase of the upper limit to the spectral fluence for the lower energies, forming a "V" shape similar to Fig. 4.10 or to HAWC's sensitivity curve in Fig. 2.13. Therefore, it is not

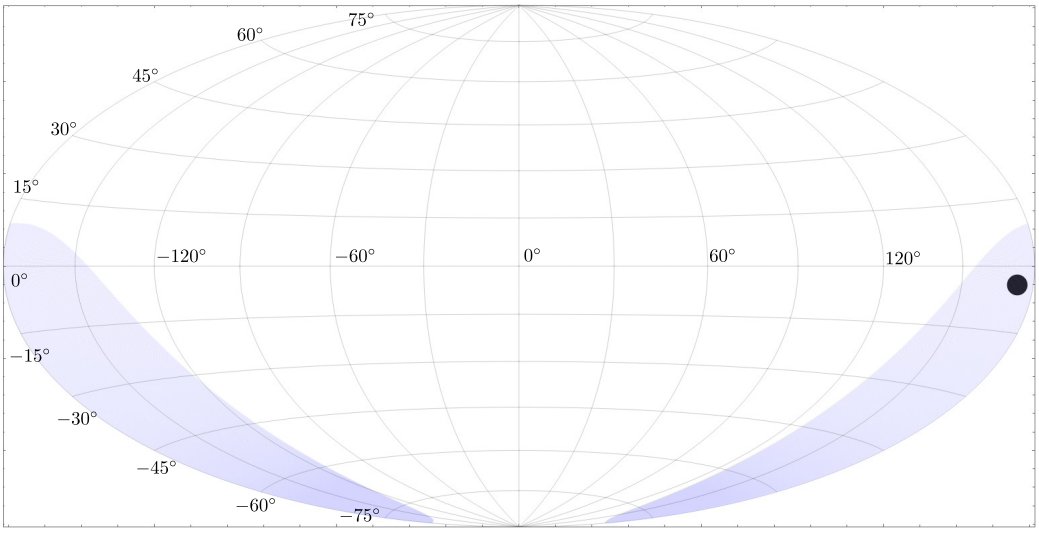


Figure 4.18: Localization of FRB 20181030E and the FoV of the Pierre Auger Observatory for the zenith angle (θ) interval of 0° to 45°, for the moment of detection.

immediate to assume that the two detectors are able to constrain the theoretical model for FRB photon counterparts coming from bright galactic sources as one would have to perform the same calculations with more realistic assumptions.

4.1.4 Sensitivity to stack analysis using catalogued FRB events

To proceed with the stack analysis using catalogued FRB events, we start by performing exactly the previous calculations of the exposure, upper limits to the flux normalization factor and to the spectral fluence, but now for a set of specific events. One expects not all FRBs to be inside the FoV of Auger for the zenith angle interval set, between 0° and 45°, in the moment of detection. Thus, for the FRBs outside the FoV, no upper limit can be imposed. Therefore, the first step is to check which FRB events were inside Auger's FoV.

Inside the blue region in Fig. 4.15, there are 127 FRBs, which means that the rest of the 774 represented FRBs can never be inside of Auger's FoV. For the remaining FRBs, we used their localization and sidereal time of their detection for checking which were inside the FoV of Auger in the interval of 0° to 45°, see eq. 4.16. Of the 127 FRBs, there was only one coincidence, see Fig. 4.18. With only one detection a stack analysis becomes impossible.

Additionally, we may ask: why only one out of the 127 FRBs was, in the moment of detection, inside of Auger's FoV? We have to consider that most of the FRB detections in the southern hemisphere come from two experiments, ASKAP and Parkes, and their field of view at any given moment will not cover the entire southern hemisphere. Also, these detectors are located in Australia whereas Auger is found in Argentina, so the two FoVs are out of phase with each other, which makes an event in their intersection unlikely.

A stack analysis cannot be performed using the Pierre Auger Observatory, but we can try it using other detectors. We begin with LHAASO and perform the same evaluation to determine how many FRB sources were inside its FoV. LHAASO has been operating stably since the end of 2019 and, therefore, we need to exclude from this analysis all previous FRB detections, leaving 92 FRB events for the coincidence study. From these 92 FRB events, 5 were inside the FoV of LHAASO in the moment of detection. Since LHAASO is in the northern hemisphere with minimum declination for detection of $\sim -15°$, see table 4.2, most of the FRB events inside its integrated field of view will have been detected by CHIME and similarly to what happened with Auger. CHIME is found in Canada and LHAASO in China, so at any given moment the FoVs of these detectors will be in opposing phases, not intersecting.

CHIME's field of view at any given moment covers all declinations until $-11°$ but only a few degrees in right ascension, making it more unlikely its intersection with another detector's field of view. In this case, CHIME's current FoV does not intersect with LHAASO's, which means that most of the FRB detections cannot be studied by LHAASO. Thus, even though LHAASO had previously seemed a promising observatory for the detection of photon counterparts of FRBs, at this moment it does not seem suitable for FRB follow-up searches, as most of the studies with catalogued events are impossible. Nonetheless, this fact can change in the future as new FRB surveys appear.

Notwithstanding, we can continue the stack analysis by estimating the upper limit to the spectral photon fluence, now using the total exposure for the 5 events, which is calculated by summing the five contributions. We follow the assumptions of subsection 4.1.1.2, with the exception of the energy interval, which is $\left[10^{11}, 10^{15}\right]$ eV. We can see the results in Fig. 4.19, where the improvement on the upper limit is approximately linear with the number of events considered, as the exposure also increases linearly. If there is a considerable number of coincident events, the sensitivity of detection can be improved noticeably.

Considering HAWC, we see that there are 418 FRB events comprehended between its maximum and minimum declination, see table 4.2. From these events, 379 were inside the FoV of HAWC at the moment of detection. As this observatory is found in Mexico, a much better intersection between FoVs, as the detectors align in longitude, is obtained. We can now perform the stack analysis by combining the individual exposures and then estimating the upper limit to the spectral photon fluence for 1 second, Fig. 4.19. Once again, the improvement is approximately linear with the number of events being considered. Therefore, for 379 events, the sensitivity increases almost 4 orders of magnitude, see Fig. 4.17 for comparison.

With this result, we see that HAWC and LHAASO are currently the best detectors to search for high energy photons as FRB counterparts and a stack analysis, if performed with sufficient statistics, can improve its sensitivity considerably. In Fig. 4.19 we see represented an estimate to the order of magnitude for the photon fluence for an extragalactic FRB with $\varepsilon_{radio} \sim 10^{40}$ erg and at typical distances of ~ 0.1 Gpc, predicted by the baryon loaded shock scenario.

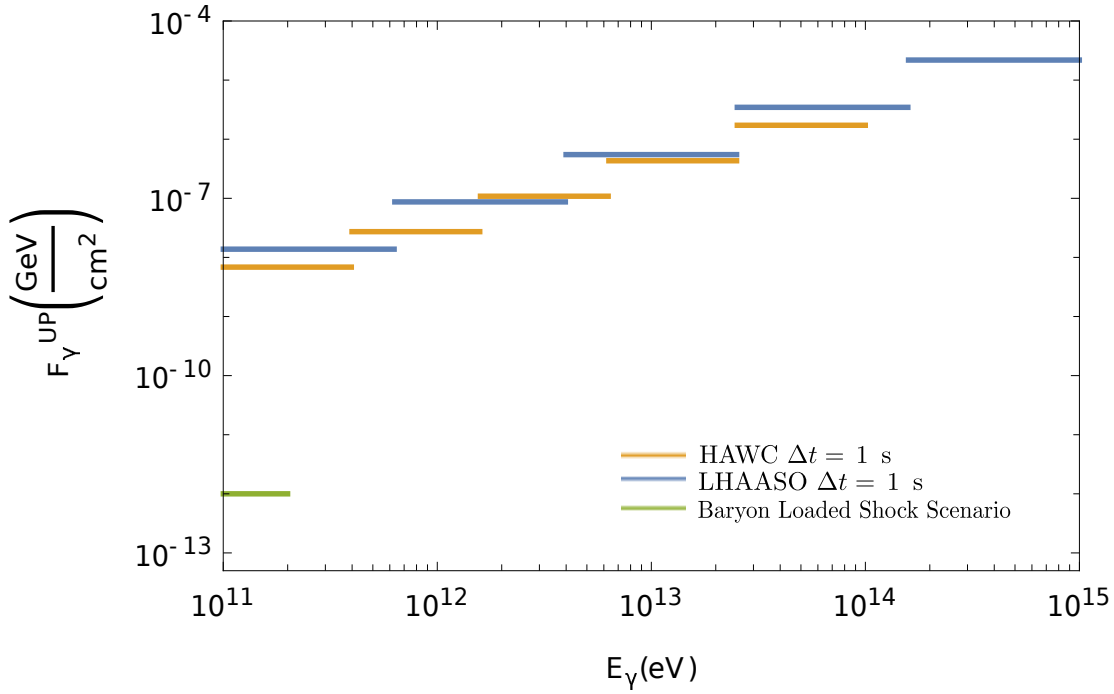


Figure 4.19: Stack analysis of the upper limit to the spectral fluence, $\mathcal{F}_\gamma^{UL}$, for photon events arriving to HAWC and LHAASO using catalogued FRB events for a 1 second analysis. Also represented is an estimate to the order of magnitude for the photon fluence for an extragalactic FRB with $\varepsilon_{radio} \sim 10^{40}$ erg and at typical distances of ~ 0.1 Gpc predicted by the baryon loaded shock scenario.

This addition is, once again, only a reference. Nevertheless, it indicates that, even though a stack analysis, when done with sufficient statistics, can improve a detector's sensitivity considerably, as for extragalactic events, the detectors' sensitivity is still approximately 4 orders of magnitude worse than the predicted fluence. Moreover, the upper limits on fluence are the best case scenario with regards to photon detection, where important aspects like the background, were neglected.

In conclusion, the theoretical model could only be constrained if there was a sufficient number of less energetic galactic events, like FRB200428, for which a stack analysis could be performed, improving sufficiently the sensitivity of detection or with the detection of a single, very bright and nearby FRB. Hence, future FRB surveys will be fundamental for both increasing the total number of FRB detections, but also to allow counterpart studies to be performed by other observatories, like LHAASO or SWGO.

4.2 High-energy neutrinos as FRB counterparts

From FRB catalogued events, the best chance for the detection in a targeted search of photon counterparts is the closest FRB ever detected, the galactic FRB. So, one can pose the question of whether Auger's FoV intersected with this source at the time of the FRB detection. In Fig. 4.20, we can see the field of view of the Pierre Auger observatory for different intervals of zenith angle (θ) for the moment of detection of FRB200428. It is possible to see that the source at this moment was not inside of the FoV of Auger for a zenith angle between 0° and 45°, the interval suitable for photon detection. Curiously, the source is, however, inside the zenith angle interval suitable for neutrino detection in Auger.

For a neutrino shower to be detected in the Pierre Auger Observatory, the neutrino has to interact closely to the Cherenkov tanks and, as so, detection is only possible in specific conditions. As already discussed, the zenith angle must vary between, $60° < \theta < 95°$. The larger zenith angles, mean that there is a bigger chance of intersection of FoV at any given moment with other FRB surveys, for example, with CHIME. However, they also mean a considerably worse effective area, which directly affects the exposure of detection, see eg. 4.15.

Thus, the next step is to understand what is Auger sensitivity to neutrino events for the energy range predicted by the baryon loaded shock scenario. The Pierre Auger Observatory has already performed studies for the detection of high energy neutrinos, but for energies $\gtrsim 10^{18}$ eV, have found no neutrino candidates. For lower energies $\gtrsim 5 \times 10^{16}$ eV, there are preliminary upper limits for the sensitivity of Auger [123]. However, in this energy interval, the sensitivity worsens considerably for the lowest energies and is overall worse than IceCube's sensitivity. To understand this dependency with energy, one has to consider the cross section for the interaction of the neutrinos near the Cherenkov water tanks, as it increases with energy.

Additionally, IceCube has a detection advantage, as its FoV covers the entire sky at any

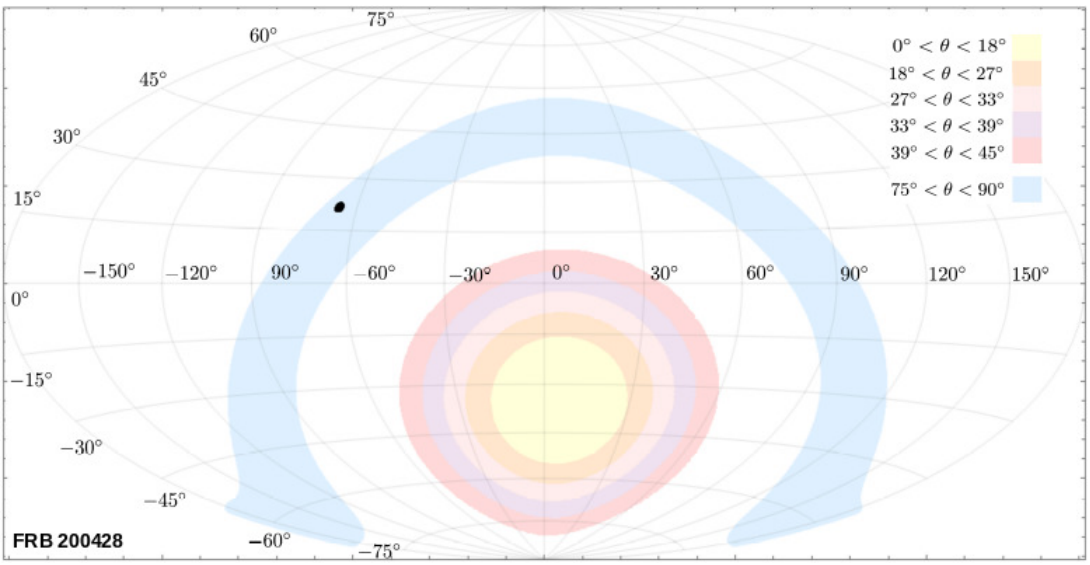


Figure 4.20: Localization of the galactic FRB 200428 (black) and the FoV of the Pierre Auger Observatory for different intervals of zenith angle (θ) at the moment of detection of the FRB.

moment. Therefore, the best detector for a follow-up analysis in search for neutrino events, as counterparts of FRBs, is IceCube. Moreover, we know that it can possibly constrain the theoretical model for a neutrino counterpart of a bright and nearby FRB, see Fig. 2.13, and such studies already exist [92, 114]. In [92], we also find a sensitivity estimate assuming an isotropic distribution of FRBs for a future stack analysis considering a varying number of catalogued FRB events. This predicts an upper limit to the spectral fluence when considering 1000 events of $\sim 10^{-4}$ GeVcm^{-2}for a 100 TeV neutrino which is an improvement of two orders of magnitude from the curve found in Fig. 2.13. As the number of catalogued FRB events has since increased significantly, a follow-up stacking search for neutrinos as FRB counterparts can be retried.

5 Conclusions and Outlook

The objective of this work was to understand whether it is possible, with current detectors and FRB detections, to constrain theoretical models for the emission of FRB counterparts and understand how it could be achieved. In the event of it not being possible, our task would be to study the future detection properties and FRB detections that would maximize the possibility to constrain FRB counterpart models.

In order to accomplish this goal, we started with an overview of fast radio bursts and their most important properties, aiming to explain the excitement surrounding them and why they are good candidates for multimessenger studies. In Chapter 2, we explored some FRB properties like their extragalactic distribution, estimated rate of occurrence and their energetics, which is the most intriguing aspect of FRBs, since it means that associated with their emission there has to be an exotic, extremely energetic event. Also, we discussed some of the still unknown aspects of FRBs, like whether there are different populations, repeaters and non repeaters, with different emission mechanisms and sources.

Another important aspect discussed in Chapter 2 were FRB source models, which are plenty and varied. However, motivated by the recent association between a galactic magnetar and a FRB, we focused our study on magnetars as FRB emission sources. To contextualize, we first gave a brief overview of the most relevant properties of magnetars and then discussed how they, as emitters, can explain most of the FRB properties. We focused then on models concerning a flaring magnetar and gave a brief explanation of one of these models called the baryon loaded shock scenario. This model not only predicts the emission of FRBs, but also of high energy counterparts, namely neutrinos and photons, and it makes predictions on the spectral fluence for both particles. We then used these predictions to guide the analysis on the subsequent chapters.

In Chapter 3, we discussed high energy particles and their detection, starting by examining the typical multimesseger signals studied and their detectors, giving particular attention to high energy photons and neutrinos as they are the particles predicted as counterparts by the theoretical model. We described them the way high energy particles interact in the atmosphere, forming extensive atmospheric showers, described by the Heitler model. The characteristics of the secondary particles created in the shower, like the number of particles and the maximum penetration depth provide information on the properties of the primary particle.

Another important topic of this thesis concerned the experimental facility in which we based

this study, the Pierre Auger Observatory. We began by describing its main characteristics and detectors, including the subdetector used in this analysis, the SD-433. A discussion of how events are reconstructed in Auger is presented, based on the size and time of arrival of signals registered by each individual SD station. We conclude the chapter with the analysis of what differentiates high energy photon and neutrino events from a typical high energy cosmic ray in a surface detector.

In Chapter 4, we began analyzing estimates in order to get a first insight on what to expect. We considered the predicted fluence for photons being emitted as counterparts of a bright FRB, with $\varepsilon_{radio} = 10^{40}$ erg, and from a nearby source, d=0.1 kpc. This allowed us to estimate the number of photons arriving, for a varying detection area (see Fig. 4.1). For the SD-433, this corresponded to one single photon.

A second calculation was made in order to estimate at which distance the closest FRB happens, during a year, for $\varepsilon = 10^{40}$ erg. The resulting value is still ∼5000 times larger than the distance of FRB200428. However, the fact that there is already a FRB detection from a galactic source at d∼10 kpc indicates that the FRB rate for lower energies should be much higher than at higher energies. This means that, with the increasing number of FRB surveys and detections, more galactic FRB detections can be expected in the next few years. Nonetheless, to recreate the curves found in Fig. 2.13, the FRB needs to be simultaneously from a nearby galactic source and highly energetic ($\varepsilon_{radio} = 10^{40}$ erg).

The analysis continued with on estimate of the upper limit for the spectral photon fluence as a measurement of the sensitivity of the detector to photon events. For that purpose, we assumed that no photon candidates would be found and as so, an upper limit could be derived. We started by defining the quantities to consider and the assumptions taken in this study. Taking in consideration both the SD-433's trigger efficiency and the energy interval for which photons in the baryon loaded shock scenario are expected to be emitted, the energy interval set was $\left[10^{16}, 10^{17}\right]$ eV. Based also on the trigger efficiency, see Fig. 4.3, for the detection of photons, we limited the zenith angle to $0° < \theta < 45°$. We also considered that the source is always inside the FoV of the detector, that we possess a perfect discriminant power and we started by considering a perfect trigger efficiency. We estimated the exposure for a 1 s interval for a source at $\sim 15°$. Using the exposure, we evaluated the flux normalization factor and plotted it for five different energy bins, Fig. 4.6. In the plot we saw that it increased with energy as expected from eq. 4.14.

The next step was to estimate of the upper limit to the spectral photon fluence at 90% CL and the resulting curves (Fig. 4.7), when compared to the predicted fluence of the baryon loaded shock scenario, which led to the conclusion that, in order for the Pierre Auger Observatory to be able to constrain this model, we would need an extremely close and bright FRB. This first estimate is still the best case scenario and the next objective was to try to understand how this result would change by introducing a realistic trigger efficiency. Perform-

ing the calculations for the same source but with a realistic trigger efficiency showed that for smaller zenith angles the introduction of the trigger efficiency only affected the lowest energy bin. When we estimate an upper limit to the spectral photon fluence for five different sources at different zenith angles, for the same small time period, we see that the different zenith angle will separate the curves and the larger the θ the larger the upper limit. The zenith angle affects the upper limit through two quantities: the effective area, which introduces a multiplicative factor over the limit; and the trigger efficiency, which is worse for larger zenith angles and lower energies.

Next, we checked the effect of the time window chosen in the analysis. We considered the same source for four different time intervals - 1, 100, 1000 and 10 000 seconds - and concluded that, because the FoV of Auger was, in this case, moving away from the source, the zenith angle increased over time. Therefore, the upper limit increased with increasing time intervals.

After, we performed the upper limit using other observatories, namely, HAWC, LHAASO and SWGO, which concern lower energies $10^{11} - 10^{15}$ eV. From this analysis we saw that the distinguishing factor for the sensitivity of detection is its effective area. However, in order to detect FRB photon counterparts, another important characteristic of the observatory becomes vital - its localization. We concluded this upon trying to perform a stack analysis using catalogued FRB events for Auger, HAWC and LHAASO and found that, as FRB surveys are still limited, there are photon observatories, namely Auger and LHAASO, with very little FRB coincidences. A future step would be to perform these calculations using a more realistic approach concerning the trigger efficiency and the background effect.

In summary, in order to constrain FRB counterpart emission models, specifically, the baryon loaded shock scenario, we conclude that the following requirements are needed: either a single very bright, $\varepsilon_{radio} > 10^{40}$ erg, and a nearby $d \sim 0.1$ kpc source FRB; or a large number of less energetic galactic events, for which a stack analysis could be performed, improving sufficiently the sensitivity of detection. Even with the increasing number of FRB detections, these requirements are hard to be met, meaning that it will take a few years of observation till photon detectors are able to constrain FRB photon counterpart models.

Bibliography

[1] Kumiko Kotera and Angela V. Olinto. The astrophysics of ultrahigh-energy cosmic rays. *Annual Review of Astronomy and Astrophysics*, 49:119–153, 2011. https://doi.org/10.1146/annurev-astro-081710-102620.

[2] Raymond Davis Jr., Don S. Harmer, and Kenneth C. Hoffman. Search for neutrinos from the sun. *Physical Review Letters*, 20(21):1205, 1968. https://doi.org/10.1103/PhysRevLett.20.1205.

[3] B. Abbott, S. Jawahar, N. Lockerbie, K. Tokmakov (LIGO scientific collaboration and Virgo collaboration). GW150914: first results from the search for binary black hole coalescence with Advanced LIGO. *Phys Rev D*, 93:122003, 2016. http://dx.doi.org/10.1103/PhysRevD.93.122003.

[4] B.P. Abbott, et al. (LIGO Scientific Collaboration and Virgo Collaboration, et al.). Multi-messenger observations of a binary neutron star merger. 2017. https://doi.org/10.3847/2041-8213/aa91c9.

[5] Arnauld Albert, Michel André, Marco Anghinolfi, M. Ardid, J-J. Aubert, et al. Search for high-energy neutrinos from binary neutron star merger GW170817 with ANTARES, IceCube, and the Pierre Auger Observatory. *arXiv:1710.05839*, 2017.

[6] Alexander Aab, Pedro Abreu, Marco Aglietta, Imen Al. Samarai, IFM Albuquerque, et al. Ultrahigh-energy neutrino follow-up of gravitational wave events GW150914 and GW151226 with the Pierre Auger Observatory. *Physical Review D*, 94(12):122007, 2016. https://doi.org/10.1103/PhysRevD.94.122007.

[7] Bing Zhang. *The physics of gamma-ray bursts*. Cambridge University Press, 2018.

[8] James M. Cordes and Shami Chatterjee. Fast radio bursts: an extragalactic enigma. *Annual Review of Astronomy and Astrophysics*, 57:417–465, 2019. https://doi.org/10.1146/annurev-astro-091918-104501.

[9] Brian Dennison. Fast radio bursts: constraints on the dispersing medium. *Monthly Notices of the Royal Astronomical Society: Letters*, 443(1):L11–L14, 2014. https://doi.org/10.1093/mnrasl/slu072.

[10] M. Caleb, C. Flynn, M. Bailes, E.D. Barr, R.W. Hunstead, et al. Are the distributions of fast radio burst properties consistent with a cosmological population? *Monthly Notices of the Royal Astronomical Society*, 458(1):708–717, 2016. https://doi.org/10.1093/mnras/stw175.

[11] Duncan R. Lorimer, Matthew Bailes, Maura Ann McLaughlin, David J. Narkevic, and Froney Crawford. A bright millisecond radio burst of extragalactic origin. *Science*, 318(5851):777–780, 2007. DOI: 10.1126/science.1147532.

[12] V. Ravi, R.M. Shannon, and A. Jameson. A fast radio burst in the direction of the Carina dwarf spheroidal galaxy. *The Astrophysical Journal Letters*, 799(1):L5, 2015. https://doi.org/10.1088/2041-8205/799/1/L5.

[13] E. Petroff, M. Bailes, E.D. Barr, B.R. Barsdell, N.D.R. Bhat, et al. A real-time fast radio burst: polarization detection and multiwavelength follow-up. *Monthly Notices of the Royal Astronomical Society*, 447(1):246–255, 2015. https://doi.org/10.1093/mnras/stu2419.

[14] Manisha Caleb, E.F. Keane, W. Van Straten, Michael Kramer, Jean-Pierre Macquart, et al. The Survey for Pulsars and Extragalactic Radio Bursts–III. Polarization properties of FRBs 160102 and 151230. *Monthly Notices of the Royal Astronomical Society*, 478(2):2046–2055, 2018. https://doi.org/10.1093/mnras/sty1137.

[15] V. Gajjar, A.P.V. Siemion, D.C. Price, C.J. Law, D. Michilli, et al. Highest frequency detection of FRB 121102 at 4–8 GHz using the breakthrough listen digital backend at the Green Bank Telescope. *The Astrophysical Journal*, 863(1):2, 2018. https://doi.org/10.3847/1538-4357/aad005.

[16] Kiyoshi Masui, Hsiu-Hsien Lin, Jonathan Sievers, Christopher J. Anderson, Tzu-Ching Chang, et al. Dense magnetized plasma associated with a fast radio burst. *Nature*, 528(7583):523–525, 2015. https://doi.org/10.1038/nature15769.

[17] D. Michilli, A. Seymour, J.W.T. Hessels, L.G. Spitler, V. Gajjar, et al. An extreme magneto-ionic environment associated with the fast radio burst source FRB 121102. *Nature*, 553(7687):182–185, 2018. https://doi.org/10.1038/nature25149.

[18] D.J. Champion, E. Petroff, M. Kramer, M.J. Keith, M. Bailes, et al. Five new fast radio bursts from the HTRU high-latitude survey at Parkes: first evidence for two-component bursts. *Monthly Notices of the Royal Astronomical Society: Letters*, 460(1):L30–L34, 2016. https://doi.org/10.1093/mnrasl/slw069.

[19] W. Farah, C. Flynn, Matthew Bailes, A. Jameson, K.W. Bannister, et al. FRB microstructure revealed by the real-time detection of FRB170827. *Monthly Notices of*

the Royal Astronomical Society, 478(1):1209–1217, 2018. https://doi.org/10.1093/mnras/sty1122.

[20] P. Scholz, L.G. Spitler, J.W.T. Hessels, S. Chatterjee, J.M. Cordes, et al. The repeating fast radio burst FRB 121102: multi-wavelength observations and additional bursts. *The Astrophysical Journal*, 833(2):177, 2016. https://doi.org/10.3847/2041-8213/834/2/L8.

[21] M. Amiri, K. Bandura, M. Bhardwaj, P. Boubel, M.M. Boyce, et al. A second source of repeating fast radio bursts. *Nature*, 833:235–238, 2019. https://doi.org/10.1038/s41586-018-0864-x.

[22] Wei Deng and Bing Zhang. Cosmological implications of fast radio burst/gamma-ray burst associations. *The Astrophysical Journal Letters*, 783(2):L35, 2014. https://doi.org/10.1088/2041-8205/783/2/L35.

[23] J. Michael Shull and Charles W. Danforth. The dispersion of fast radio bursts from a structured intergalactic medium at redshifts z$<$ 1.5. *The Astrophysical Journal Letters*, 852(1):L11, 2018. https://doi.org/10.3847/2041-8213/aaa2fa.

[24] Z. Zheng, E.O. Ofek, S.R. Kulkarni, J.D. Neill, and M. Juric. Probing the intergalactic medium with fast radio bursts. *The Astrophysical Journal*, 797(1):71, 2014. https://doi.org/10.1088/0004-637X/797/1/71.

[25] He Gao, Zhuo Li, and Bing Zhang. Fast radio burst/gamma-ray burst cosmography. *The Astrophysical Journal*, 788(2):189, 2014. https://doi.org/10.1088/0004-637X/788/2/189.

[26] Julian B. Munoz, Ely D. Kovetz, Liang Dai, and Marc Kamionkowski. Lensing of fast radio bursts as a probe of compact dark matter. *Physical Review Letters*, 117(9):091301, 2016. https://doi.org/10.1103/PhysRevLett.117.091301.

[27] Y.K. Wang and F.Y. Wang. Lensing of fast radio bursts by binaries to probe compact dark matter. *Astronomy & Astrophysics*, 614:A50, 2018. https://doi.org/10.1051/0004-6361/201731160.

[28] F. Vazza, M. Brüggen, P.M. Hinz, D. Wittor, N. Locatelli, and C. Gheller. Probing the origin of extragalactic magnetic fields with Fast Radio Bursts. *Monthly Notices of the Royal Astronomical Society*, 480(3):3907–3915, 2018. https://doi.org/10.1093/mnras/sty1968.

[29] Julian B. Munoz, Ely D. Kovetz, Liang Dai, and Marc Kamionkowski. Lensing of fast radio bursts as a probe of compact dark matter. *Physical Review Letters*, 117(9):091301, 2016. https://doi.org/10.1103/PhysRevLett.117.091301.

[30] Ricardo G. Landim. Constraining dark photon dark matter with fast radio bursts. *Eur. Phys. J. C*, 80:913, 2020. https://doi.org/10.1140/epjc/s10052-020-08495-6.

[31] Luca Bonetti, John Ellis, Nikolaos E. Mavromatos, Alexander S. Sakharov, Edward K. Sarkisyan-Grinbaum, and Alessandro D.A.M. Spallicci. Photon mass limits from fast radio bursts. *Physics Letters B*, 757:548–552, 2016. https://doi.org/10.1016/j.physletb.2016.04.035.

[32] Nan Xing, He Gao, Jun-Jie Wei, Zhengxiang Li, Weiyang Wang, et al. Limits on the weak equivalence principle and photon mass with FRB 121102 subpulses. *The Astrophysical Journal Letters*, 882(1):L13, 2019. https://doi.org/10.3847/2041-8213/ab3c5f.

[33] Bei Zhou, Xiang Li, Tao Wang, Yi-Zhong Fan, and Da-Ming Wei. Fast radio bursts as a cosmic probe?. *Physical Review D*, 89(10):107303, 2014. https://doi.org/10.1103/PhysRevD.89.107303.

[34] Anthony Walters, Amanda Weltman, B.M. Gaensler, Yin-Zhe Ma, and Amadeus Witzemann. Future cosmological constraints from fast radio bursts. *The Astrophysical Journal*, 856(1):65, 2018. https://doi.org/10.3847/1538-4357/aaaf6b.

[35] Orfeu Bertolami and Ricardo G Landim. Cosmic transients, Einstein's equivalence principle and dark matter halos. *Physics of the dark universe*, 21:16–20, 2018. https://doi.org/10.1016/j.dark.2018.05.002.

[36] Steven J. Tingay and David L. Kaplan. Limits on Einstein's equivalence principle from the first localized fast radio burst FRB 150418. *The Astrophysical Journal Letters*, 820(2):L31, 2016. https://doi.org/10.3847/2041-8205/820/2/L31.

[37] Vikram Ravi, R.M. Shannon, M. Bailes, K. Bannister, S. Bhandari, et al. The magnetic field and turbulence of the cosmic web measured using a brilliant fast radio burst. *Science*, 354(6317):1249–1252, 2016. DOI: 10.1126/science.aaf6807.

[38] Anastasia Fialkov and Abraham Loeb. Constraining the CMB optical depth through the dispersion measure of cosmological radio transients. *Journal of Cosmology and Astroparticle Physics*, 2016(05):004, 2016. https://doi.org/10.1088/1475-7516/2016/05/004.

[39] Yun-Wei Yu, Kwong-Sang Cheng, Gary Shiu, and Henry Tye. Implications of fast radio bursts for superconducting cosmic strings. *Journal of Cosmology and Astroparticle Physics*, 2014(11):040, 2014. https://doi.org/10.1088/1475-7516/2014/11/040.

[40] Christopher D. Bochenek, Vikram Ravi, Konstantin V. Belov, Gregg Hallinan, Jonathon Kocz, Shri R. Kulkarni, and Dan L. McKenna. A fast radio burst associated with a galactic magnetar. *Nature*, 587(7832):59–62, 2020. http://doi.org/10.22002/D1.1647.

[41] Benito Marcote, Kenzie Nimmo, J.W.T. Hessels, S.P. Tendulkar, C.G. Bassa, et al. A repeating fast radio burst source localized to a nearby spiral galaxy. *Nature*, 577(7789):190–194, 2020. https://doi.org/10.1038/s41586-019-1866-z.

[42] D. Thornton, B. Stappers, M. Bailes, B. Barsdell, S. Bates, N.D.R. Bhat, M. Burgay, S. Burke-Spolaor, D.J. Champion, P. Coster, et al. A population of fast radio bursts at cosmological distances. *Science*, 341(6141):53–56, 2013. DOI:10.1126/science.1236789.

[43] Transient name server. http://www.wis-tns.org. Accessed: 2021-09.

[44] Mandana Amiri, Bridget C. Andersen, Kevin Bandura, Sabrina Berger, Mohit Bhardwaj, et al. The First CHIME/FRB Fast Radio Burst Catalog. *Submitted to ApJS, arXiv:2106.04352*, 2021.

[45] E. Platts, A. Weltman, A. Walters, S.P. Tendulkar, J.E.B. Gordin, and S. Kandhai. A living theory catalogue for fast radio bursts. *Physics Reports*, 821:1–27, 2019. https://doi.org/10.1016/j.physrep.2019.06.003.

[46] Ziggy Pleunis, Deborah C. Good, Victoria M. Kaspi, Ryan Mckinven, Scott M. Ransom, et al. Fast Radio Burst Morphology in the First CHIME/FRB Catalog. *Accepted for publication in APJ arXiv:2106.04356*, 2021.

[47] Masoud Rafiei-Ravandi, Kendrick M. Smith, Dongzi Li, Kiyoshi W. Masui, Alexander Josephy, et al. CHIME/FRB Catalog 1 results: statistical cross-correlations with large-scale structure. *arXiv:2106.04354*, 2021.

[48] Casey J. Law, Geoffrey C. Bower, Sarah Burke-Spolaor, Bryan Butler, Earl Lawrence, et al. A millisecond interferometric search for fast radio bursts with the Very Large Array. *The Astrophysical Journal*, 807(1):16, 2015. https://doi.org/10.1088/0004-637X/807/1/16.

[49] S. Chatterjee, C.J. Law, R.S. Wharton, S. Burke-Spolaor, J.W.T. Hessels, et al. A direct localization of a fast radio burst and its host. *Nature*, 541(7635):58–61, 2017. https://doi.org/10.1038/nature20797.

[50] Shriharsh P. Tendulkar, C.G. Bassa, James M. Cordes, Geoffery C. Bower, Casey J. Law, et al. The host galaxy and redshift of the repeating fast radio burst FRB 121102. *The Astrophysical Journal Letters*, 834(2):L7, 2017. https://doi.org/10.3847/2041-8213/834/2/L7.

[51] Keith W. Bannister, Adam T. Deller, C. Phillips, J.P. Macquart, Jason X. Prochaska, et al. A single fast radio burst localized to a massive galaxy at cosmological distance. *Science*, 365(6453):565–570, 2019. DOI: 10.1126/science.aaw5903.

[52] V. Ravi, M. Catha, L. D'Addario, S.G. Djorgovski, G. Hallinan, et al. A fast radio burst localized to a massive galaxy. *Nature*, 572(7769):352–354, 2019. https://doi.org/10.1038/s41586-019-1389-7.

[53] B.C. Andersen, K.M. Bandura, M. Bhardwaj, A. Bij, M.M. Boyce, et al. A bright millisecond-duration radio burst from a Galactic magnetar. *Nature*, 587:54–58, 2020. https://doi.org/10.1038/s41586-020-2863-y.

[54] E. Parent, P. Chawla, V.M. Kaspi, G.Y. Agazie, H. Blumer, et al. First Discovery of a Fast Radio Burst at 350 MHz by the GBNCC Survey. *The Astrophysical Journal*, 904(2):92, 2020. https://doi.org/10.3847/1538-4357/abbdf6.

[55] W. Farah, C. Flynn, M. Bailes, A. Jameson, T. Bateman, et al. Five new real-time detections of fast radio bursts with UTMOST. *Monthly Notices of the Royal Astronomical Society*, 488(3):2989–3002, 2019. https://doi.org/10.1093/mnras/stz1748.

[56] L.G. Spitler, J.M. Cordes, J.W.T. Hessels, D.R. Lorimer, M.A. McLaughlin, et al. Fast radio burst discovered in the Arecibo pulsar ALFA survey. *The Astrophysical Journal*, 790(2):101, 2014. https://doi.org/10.1088/0004-637X/790/2/101.

[57] E. Fonseca, B.C. Andersen, M. Bhardwaj, P. Chawla, D.C. Good, et al. Nine new repeating fast radio burst sources from CHIME/FRB. *The Astrophysical Journal Letters*, 891(1):L6, 2020. https://doi.org/10.3847/1538-4357/abbdf6.

[58] L. Connor, M.C. Miller, and D.W. Gardenier. Beaming as an explanation of the repetition/width relation in FRBs. *Monthly Notices of the Royal Astronomical Society*, 497(3):3076–3082, 2020. https://doi.org/10.1093/mnras/staa2074.

[59] Brian D. Metzger, Ke Fang, and Ben Margalit. Neutrino Counterparts of Fast Radio Bursts. *The Astrophysical Journal Letters*, 902(1):L22, 2020. https://doi.org/10.3847/2041-8213/abbb88.

[60] Manasvi Lingam and Abraham Loeb. Fast radio bursts from extragalactic light sails. *The Astrophysical Journal Letters*, 837(2):L23, 2017. https://doi.org/10.3847/2041-8213/aa633e.

[61] Aurélien Barrau, Carlo Rovelli, and Francesca Vidotto. Fast radio bursts and white hole signals. *Physical Review D*, 90(12):127503, 2014. https://doi.org/10.1103/PhysRevD.90.127503.

[62] Ludovic Van Waerbeke and Ariel Zhitnitsky. Fast radio bursts and the axion quark nugget dark matter model. *Physical Review D*, 99(4):043535, 2019. https://doi.org/10.1103/PhysRevD.99.043535.

[63] Wei-Min Gu, Yi-Ze Dong, Tong Liu, Renyi Ma, and Junfeng Wang. A neutron star–white dwarf binary model for repeating fast radio burst 121102. *The Astrophysical Journal Letters*, 823(2):L28, 2016. https://doi.org/10.3847/2041-8205/823/2/L28.

[64] Shotaro Yamasaki, Tomonori Totani, and Kenta Kiuchi. Repeating and non-repeating fast radio bursts from binary neutron star mergers. *Publications of the Astronomical Society of Japan*, 70(3):39, 2018. https://doi.org/10.1093/pasj/psy029.

[65] Long-Biao Li, Yong-Feng Huang, Jin-Jun Geng, and Bing Li. A model of fast radio bursts: collisions between episodic magnetic blobs. *Research in Astronomy and Astrophysics*, 18(6):061, 2018. https://doi.org/10.1088/1674-4527/18/6/61.

[66] Heino Falcke and Luciano Rezzolla. Fast radio bursts: the last sign of supramassive neutron stars. *Astronomy & Astrophysics*, 562:A137, 2014. https://doi.org/10.1051/0004-6361/201321996.

[67] Fabrice Mottez and Philippe Zarka. Radio emissions from pulsar companions: a refutable explanation for galactic transients and fast radio bursts. *Astronomy & Astrophysics*, 569:A86, 2014. https://doi.org/10.1051/0004-6361/201424104.

[68] S. Chandrasekhar. The Maximum Mass of Ideal White Dwarfs. *APJ*, 74:81, 1931. DOI: 10.1086/143324.

[69] Bradley W. Carroll and Dale A. Ostlie. *An introduction to modern astrophysics*. Cambridge University Press, 2nd Edition, 2017.

[70] Victoria M. Kaspi and Andrei M. Beloborodov. Magnetars. *Annual Review of Astronomy and Astrophysics*, 55:261–301, 2017. https://doi.org/10.1146/annurev-astro-081915-023329.

[71] Diego F Torres and Nanda Rea. High-Energy: Emission from Pulsars and their Systems. In *Proceedings of the first session of the Sant Cugat forum on astrophysics, astrophysics and space science proceedings. Berlin*, volume 531. Springer, 2011. DOI 10.1007/978-3-642-17251-9.

[72] Andrei M. Beloborodov. A flaring magnetar in FRB 121102? *The Astrophysical Journal Letters*, 843(2):L26, 2017. https://doi.org/10.3847/2041-8213/aa78f3.

[73] Yuri Lyubarsky. Fast radio bursts from reconnection in a magnetar magnetosphere. *The Astrophysical Journal*, 897(1):1, 2020. https://doi.org/10.3847/1538-4357/ab97b5.

[74] Brian D. Metzger, Ben Margalit, and Lorenzo Sironi. Fast radio bursts as synchrotron maser emission from decelerating relativistic blast waves. *Monthly Notices of*

the Royal Astronomical Society, 485(3):4091–4106, 2019. https://doi.org/10.1093/mnras/stz700.

[75] Yuri Lyubarsky. A model for fast extragalactic radio bursts. *Monthly Notices of the Royal Astronomical Society: Letters*, 442(1):L9–L13, 2014. https://doi.org/10.1093/mnrasl/slu046.

[76] S. Johnston, E.F. Keane, S. Bhandari, J.P. Macquart, S.J. Tingay, et al. Radio light curve of the galaxy possibly associated with FRB 150418. *Monthly Notices of the Royal Astronomical Society*, page stw2808, 2016. https://doi.org/10.1093/mnras/stw2808.

[77] Shao-Qiang Xi, Pak-Hin Thomas Tam, Fang-Kun Peng, and Xiang-Yu Wang. Search for GeV counterparts to fast radio bursts with Fermi. *The Astrophysical Journal Letters*, 842(1):L8, 2017. https://doi.org/10.3847/2041-8213/aa74cf.

[78] P. Scholz, A. Cook, M. Cruces, J.W.T. Hessels, V.M. Kaspi, et al. Simultaneous X-Ray and Radio Observations of the Repeating Fast Radio Burst FRB 180916. J0158+ 65. *The Astrophysical Journal*, 901(2):165, 2020. https://doi.org/10.3847/1538-4357/abb1a8.

[79] S. Mereghetti, V. Savchenko, C. Ferrigno, D. Götz, M. Rigoselli, et al. INTEGRAL discovery of a burst with associated radio emission from the magnetar SGR 1935+ 2154. *The Astrophysical Journal Letters*, 898(2):L29, 2020. https://doi.org/10.3847/2041-8213/aba2cf.

[80] Roger D. Blandford and James P. Ostriker. Particle acceleration by astrophysical shocks. *The Astrophysical Journal*, 221:L29–L32, 1978. DOI: 10.1086/182658.

[81] Israel Martinez-Castellanos. Search for very-high-energy gamma-ray counterparts of gravitational waves with HAWC. *PoS*, ICRC2019:737, 2019. DOI: 10.22323/1.358.0737.

[82] Divya Palaniswamy, Randall B. Wayth, Cathryn M. Trott, Jamie N. McCallum, Steven J. Tingay, and Cormac Reynolds. A search for fast radio bursts associated with gamma-ray bursts. *The Astrophysical Journal*, 790(1):63, 2014. https://doi.org/10.1088/0004-637X/790/1/63.

[83] D.R. Madison, D. Agarwal, K. Aggarwal, O. Young, H.T. Cromartie, et al. A Deep Targeted Search for Fast Radio Bursts from the Sites of Low-redshift Short Gamma-Ray Bursts. *The Astrophysical Journal*, 887(2):252, 2019. https://doi.org/10.3847/1538-4357/ab58c3.

[84] Nipuni T. Palliyaguru, Devansh Agarwal, Golnoosh Golpayegani, Ryan Lynch, Duncan R. Lorimer, et al. A targeted search for repeating fast radio bursts associated with

gamma-ray bursts. *Monthly Notices of the Royal Astronomical Society*, 501(1):541–547, 2021. https://doi.org/10.1093/mnras/staa3352.

[85] Shotaro Yamasaki, Tomonori Totani, and Norita Kawanaka. A blind search for prompt gamma-ray counterparts of fast radio bursts with fermi-lat data. *Monthly Notices of the Royal Astronomical Society*, 460(3):2875–2880, 2016. https://doi.org/10.1093/mnras/stw1206.

[86] G.H. Hilmarsson, L.G. Spitler, E.F. Keane, T.M. Athanasiadis, E. Barr, et al. Observing superluminous supernovae and long gamma-ray bursts as potential birthplaces of repeating fast radio bursts. *Monthly Notices of the Royal Astronomical Society*, 493(4):5170–5180, 2020. https://doi.org/10.1093/mnras/staa701.

[87] Akash Anumarlapudi, Varun Bhalerao, Shriharsh P. Tendulkar, and Arvind Balasubramanian. Prompt X-Ray Emission from Fast Radio Bursts—Upper Limits with AstroSat. *The Astrophysical Journal*, 888(1):40, 2020. https://doi.org/10.3847/1538-4357/ab5363.

[88] Thomas Callister, Jonah Kanner, and Alan Weinstein. Gravitational-wave constraints on the progenitors of fast radio bursts. *The Astrophysical Journal Letters*, 825(1):L12, 2016. https://doi.org/10.3847/2041-8205/825/1/L12.

[89] Jun-Jie Wei, Xue-Feng Wu, and He Gao. Cosmology with gravitational wave/fast radio burst associations. *The Astrophysical Journal Letters*, 860(1):L7, 2018. https://doi.org/10.3847/2041-8213/aac8e2.

[90] A. Albert, M. André, M. Anghinolfi, G. Anton, M. Ardid, et al. The search for high-energy neutrinos coincident with fast radio bursts with the ANTARES neutrino telescope. *Monthly Notices of the Royal Astronomical Society*, 482(1):184–193, 2019. https://doi.org/10.1093/mnras/sty2621.

[91] Samuel Fahey, Ali Kheirandish, Justin Vandenbroucke, and Donglian Xu. A search for neutrinos from fast radio bursts with IceCube. *The Astrophysical Journal*, 845(1):14, 2017. https://doi.org/10.3847/1538-4357/aa7e28.

[92] M.G. Aartsen, M. Ackermann, J. Adams, J.A. Aguilar, M. Ahlers, et al. A search for neutrino emission from fast radio bursts with six years of IceCube data. *The Astrophysical Journal*, 857(2):117, 2018. https://doi.org/10.3847/1538-4357/aab4f8.

[93] Péter Mészáros, Derek B. Fox, Chad Hanna, and Kohta Murase. Multi-messenger astrophysics. *Nature Reviews Physics*, 1(10):585–599, 2019. https://doi.org/10.1038/s42254-019-0101-z.

[94] Alessandro De Angelis and Mário João Martins Pimenta. *Introduction to particle and astroparticle physics: questions to the Universe*. Springer, 2015. DOI: 10.1007/978-88-470-2688-9.

[95] M. Tavani, G. Barbiellini, A. Argan, F. Boffelli, A. Bulgarelli, et al. The AGILE mission. *Astronomy & Astrophysics*, 502(3):995–1013, 2009. https://doi.org/10.1051/0004-6361/200810527.

[96] Julie E. McEnery, Peter F. Michelson, William S. Paciesas, and Steven Ritz. Fermi gamma-ray space telescope. *Optical Engineering*, 51(1):011012, 2012. https://doi.org/10.1117/1.OE.51.1.011012.

[97] Eckart Lorenz and Robert Wagner. Very-high energy gamma-ray astronomy. *The European Physical Journal H*, 37(3):459–513, 2012. https://doi.org/10.1140/epjh/e2012-30016-x.

[98] James Anthony Hinton, et al. (Hess Collaboration). The status of the HESS project. *New Astronomy Reviews*, 48(5-6):331–337, 2004. https://doi.org/10.1016/j.newar.2003.12.004.

[99] Carmen Baixeras, et al. (Magic Collaboration). The MAGIC telescope. *Nuclear Physics B-Proceedings Supplements*, 114:247–252, 2003. https://doi.org/10.1016/S0920-5632(02)01910-2.

[100] Jamie Holder, R.W. Atkins, H.M. Badran, G. Blaylock, S.M. Bradbury, et al. The first VERITAS telescope. *Astroparticle Physics*, 25(6):391–401, 2006. https://doi.org/10.1016/j.astropartphys.2006.04.002.

[101] Tyce DeYoung, et al. (HAWC Collaboration). The HAWC observatory. *Nuclear Instruments and Methods in Physics Research Section A: Accelerators, Spectrometers, Detectors and Associated Equipment*, 692:72–76, 2012. https://doi.org/10.1016/j.nima.2012.01.026.

[102] Huihai He. Design of the LHAASO detectors. *Radiation Detection Technology and Methods*, 2(1):1–8, 2018. https://doi.org/10.1007/s41605-018-0037-3.

[103] P. Abreu, A. Albert, R. Alfaro, C. Alvarez, R. Arceo, et al. The Southern Wide-Field Gamma-Ray Observatory (SWGO): a next-generation ground-based survey instrument for VHE gamma-ray astronomy. *arXiv preprint arXiv:1907.07737*, 2019.

[104] David Fink, Michael Hotchkis, Quan Hua, Geraldine Jacobsen, Andrew M. Smith, et al. The antares AMS facility at ANSTO. *Nuclear Instruments and Methods in Physics Research Section B: Beam Interactions with Materials and Atoms*, 223:109–115, 2004. https://doi.org/10.1016/j.nimb.2004.04.025.

[105] Mark G. Aartsen, M. Ackermann, J. Adams, J.A. Aguilar, M. Ahlers, et al. The IceCube Neutrino Observatory: instrumentation and online systems. *Journal of Instrumentation*, 12(03):P03012, 2017. https://doi.org/10.1088/1748-0221/12/03/P03012.

[106] James Matthews. A Heitler model of extensive air showers. *Astroparticle Physics*, 22(5-6):387–397, 2005. https://doi.org/10.1016/j.astropartphys.2004.09.003.

[107] Ralf Ulrich, Ralph Engel, and Michael Unger. Hadronic multiparticle production at ultrahigh energies and extensive air showers. *Physical Review D*, 83(5):054026, 2011. https://doi.org/10.1103/PhysRevD.83.054026.

[108] Alexander Aab, Pedro Abreu, Marco Aglietta, Imen Al Samarai, I.F.M. Albuquerque, Ingomar Allekotte, et al. Search for photons with energies above 1018 eV using the hybrid detector of the Pierre Auger Observatory. *Journal of cosmology and astroparticle physics*, 2017(04):009, 2017. https://doi.org/10.1088/1475-7516/2017/04/009.

[109] Pierre Auger Collaboration. The Pierre Auger cosmic ray observatory. *Nuclear Instruments and Methods in Physics Research Section A: Accelerators, Spectrometers, Detectors and Associated Equipment*, 798:172–213, 2015. https://doi.org/10.1016/j.nima.2015.06.058.

[110] D. Ravignani G. Silli, D. Melo et al. Study of the efficiency for the SD-433. *The Auger Observatory internal note*, 2021.

[111] Koichi Kamata and Jun Nishimura. The lateral and the angular structure functions of electron showers. *Progress of Theoretical Physics Supplement*, 6:93–155, 1958. https://doi.org/10.1143/PTPS.6.93.

[112] Philip Ruehl, Marcus Niechciol, and Markus Risse. Follow-Up Search for UHE Photons after Gravitational Wave Events with the Pierre Auger Observatory. *Verhandlungen der Deutschen Physikalischen Gesellschaft*, 2019.

[113] Wenbin Lu and Anthony L. Piro. Implications from ASKAP fast radio burst statistics. *The Astrophysical Journal*, 883(1):40, 2019. https://doi.org/10.3847/1538-4357/ab3796.

[114] Ali Kheirandish, Alex Pizzuto, Justin Vandenbroucke, et al. Searches for neutrinos from fast radio bursts with IceCube. *The Astrophysical Journal*, 845(1):14, 2017.

[115] Gary J. Feldman and Robert D. Cousins. Unified approach to the classical statistical analysis of small signals. *Physical Review D*, 57(7):3873, 1998. https://doi.org/10.1103/PhysRevD.57.3873.

[116] Alexander Aab, Pedro Abreu, Marco Aglietta, Justin M. Albury, Ingomar Allekotte, et al. Measurement of the cosmic-ray energy spectrum above 2.5×10^{18} eV using the Pierre Auger Observatory. *Physical Review D*, 102(6):062005, 2020. https://doi.org/10.1103/PhysRevD.102.062005.

[117] Nicolás Martín González. Search for ultra-high energy photons with the AMIGA muon detector. *PHD Thesis*, 2018. https://publikationen.bibliothek.kit.edu/1000081130.

[118] Stephen Wolfram. Wolfram research. *Inc., Mathematica, Version*, 8:23, 2013.

[119] Francesco Fenu, et al. (Pierre Auger Collaboration). The cosmic ray energy spectrum measured using the Pierre Auger Observatory. In *35th International Cosmic Ray Conference*, volume 301, page 486. SISSA Medialab, 2018. DOI: 10.22323/1.301.0486.

[120] N.Gonzalez et al. Internal note of the Pierre Auger Collaboration GAP 2020-038, 2020.

[121] G. Di Sciascio, et al. (Lhaaso Collaboration). The LHAASO experiment: from gamma-ray astronomy to cosmic rays. *Nuclear and particle physics proceedings*, 279:166–173, 2016. https://doi.org/10.1016/j.nuclphysbps.2016.10.024.

[122] Israel Martinez-Castellanos. Search for very-high-energy gamma-ray counterparts of gravitational waves with HAWC. *PoS*, ICRC2019:737, 2020. DOI: 10.22323/1.358.0737.

[123] Marta Trini and Jaime Alvarez. Search for sub-EeV neutrinos with the Infilled array of the Pierre Auger Observatory GAP 2020-027, 2020.